# Development of Reduced Chemical Models for Simulations of Biomass Pyrolysis and Combustion

by

**Jeffrey F. Glusman**

B.S. Mechanical Engineering, The Pennsylvania State University, 2013

M.S. Aeronautics and Astronautics, The University of Washington, 2016

A thesis submitted to the

Faculty of the Graduate School of the

University of Colorado in partial fulfillment

of the requirements for the degree of

Doctor of Philosophy

Paul M. Rady Department of Mechanical Engineering

2022

Committee Members:

Prof. John W. Daily, Co-Chair

Prof. Peter E. Hamlington, Co-Chair

Prof. Gregory B. Rieker

Prof. Hope A. Michelsen

Prof. John A. N. Farnsworth

Glusman, Jeffrey F. (Ph.D., Mechanical Engineering)

Development of Reduced Chemical Models for Simulations of Biomass Pyrolysis and Combustion

Thesis directed by Prof. John W. Daily and Prof. Peter E. Hamlington

Predicting the spread and environmental impacts of wildland fires remains an inexact science. Extreme temperature shifts due to climate change alongside continuous societal expansion have caused the wildland urban interface to grow. As this interface grows, these natural disasters will become deadlier and costlier each year. There has been a push for physics-based predictive fire spread models, yet simulations remain challenging due to the immense computational requirements introduced by the complex chemistry of biomass pyrolysis, ignition, and combustion. Furthermore, the large separation of spatial-temporal scales requires most simulations to resolve large scales and model small scales. The range of spatial scales in wildland fires spans from global weather patterns, on the order of thousands of kilometers, to chemical reactions on sub-millimeter scales. The range of temporal scales spans from days to reaction scales on the order of microseconds. The research presented in this thesis is focused on enabling physics-based computational modeling of chemical processes occurring at small spatial scales and on short time scales, with a view towards implementing the resulting models in much larger-scale and more computationally intensive simulations of wildland fire spread.

This dissertation outlines the steps taken to address the computational and time requirements required for simulations of reacting flows. These consist of *a priori* kinetic mechanism reduction, the integration of adaptive mesh refinement and dynamic load balancing with a multi-phase simulation, the use of tabulated chemistry with various skeletal models and the derivation of a lumped specie for use in an infinitely-fast chemistry simulation. Ultimately, the work encompassed here provides a computationally-efficient framework for simulations of biomass pyrolysis, ignition, and combustion.

The introductory chapter provides additional motivation for the study of wildland fire simulations, an expansive outline of the thesis and a listing of the contributions made to the research

community. The second chapter provides background on mechanism reduction and its application to a comprehensive, biomass-specific mechanism to produce something more suitable for a large simulation. The third chapter discusses the development and verification of a computational framework that is compared to a cone-calorimeter experiment. The fourth chapter investigates the role of reduced models in the characteristics of reacting plumes. The final chapter discusses the overall conclusions of this work and contributions made in the dissertation.

## Dedication

To students: past, present and future.

In memory of Caelan Lapointe, you taught me everything OpenFOAM, CAATS and puns.

## Acknowledgements

I'd like to thank Peter and John for their advice, time, support and consistent words of wisdom: "Onward and upward!" - John — "Having hope only leads to despair." - Peter

I'd like to thank the entirety of the committee for their review, remarks, questions and discussions.

I'd like to thank the students of the Turbulent Energy Systems Laboratory for adopting me and providing crucial support, criticisms and friendship throughout this process. An immense amount of gratitude goes specifically to Caelan, SSW, and Mike, this work wouldn't exist without them.

I'd like to thank the department for putting their trust in me as the Lead Graduate Student Fellow to the Center for Teaching & Learning and thrice as a Graduate Part-Time Instructor. These roles contributed to my financial support and, more importantly, kept the fire alive within me.

I'd like to thank my family, friends and Lightning for keeping me sane. And lastly, to Amber for sticking by my side through the uncertainties, the long hikes, long days and everything in between.

And to my trusty AMD Ryzen™ 7 2700x, may you live on in infamy.

This research was supported by the Strategic Environmental Research and Development Program (SERDP) under grant W912HQ-16-C-0026 as project number RC-2642, and under grant W912HQ-20-C-0065 as project number RC20-1382. This work utilized the Texas Advanced Computing Center (TACC) at The University of Texas at Austin for providing HPC resources that have contributed to the research results reported. This work utilized the Summit supercomputer, which is supported by the National Science Foundation (awards ACI-1532235 and ACI-1532236), the University of Colorado Boulder, and Colorado State University.

# Contents

**Chapter**

# Tables

**Table**

# Figures

**Figure**

# Chapter 1

# Introduction

*"Our real discoveries come from chaos, from going to the place that looks wrong and stupid and foolish."*

— unnamed narrator*, Chuck Palahniuk, Invisible Monsters*

The negative impact of wildland fires on the environment, infrastructure and a multitude of other factors are being exacerbated by the increasing variability due to climate change. Between 2010 and 2015, wildland fires consumed over 29 million acres of timber, grass, and brush in the United States, equivalent to nearly half the surface area of Colorado. Over the same period, $8 billion was spent on fire suppression by federal agencies and almost 11 million additional acres of wildland fuel were removed through preventative prescribed burns. Nearly two thousand structures were lost as the result of wildland fires in 2014 alone. In 2017, 9.8 million aces burned, including the largest fire in California history [1]. Moreover, it is anticipated that over the coming decades, climate change will contribute to increased wildland fire activity, particularly in the Western United States [2]. This is evident in the 2020 fire season in California where the growing wildland urban interface and dry conditions led to the deadliest fire season to date that included five of the top twenty largest wildfires [3].

Wildland fires are multi-physics problems involving multi-phase flow, solid fuel pyrolysis, chemical heat release, and heat transfer via both radiation and turbulence-mediated convection. Further complicating the problem, these physical processes depend on fuel type (i.e., specie of tree, grass or plant), fuel geometry (i.e., the shape of the entire tree, broken branch or leaves), and topography, among many other factors, and span an enormous range of spatial and temporal

scales, from millimeter-scale chemical processes to fire spread at landscape scales.

Although numerical simulations provide a low-cost, low-risk approach to studying wildland fire, simulation accuracy is constrained by the challenge of representing physical processes spanning such widely disparate scales [4, 5]. Predicting wildland fires using computational models remains, however, an inexact science. Such models can generally be divided into two categories: semi-empirical operational models used for nearly real-time incident response, such as the Fire Area Simulator (FARSITE) [6], and physics-based models used to understand the dynamics of fire spread, such as the Weather Research and Forecasting Model and Fire (WRF-Fire) [7]. Although there is a growing trend in wildland fire research towards physics-based models [8–12], these models remain limited by the daunting challenge of incorporating the physics of wildland fuel combustion in landscape scale numerical simulations that are coupled to atmospheric dynamics and weather [7]. The need for such scale-resolving simulations arises from the considerable environmental and economic cost of wildland fires, as well as the difficulty in establishing future mitigation and avoidance strategies. It is anticipated that climate change will contribute to increased wildland fire activity [13, 14], further increasing the importance of simulations in fire management efforts. Additionally, predicting pollutants produced from controlled burns would inform burns near highly populated areas to reduce their societal impacts [15, 16].

From a fundamental perspective, biomass burning during wildland fires consists of three interrelated physical processes: pyrolysis, ignition, and combustion-induced heat release. Pyrolysis is the gasification of solid fuel into gaseous fuel and can be performed in the absence of oxygen. The pyrolysis process consists of thousands to millions of elementary reactions [17] and thus requires modeling to be tractably simulated. Attempts to capture the complexity of the pyrolysis mechanism with significantly simpler kinetics have been devised in the forms of single-component/single-step, single-component/multi-step, multi-component/single-step and multi-component/multi-step kinetics [18]. The Activation Energy Distribution Model (AEDM) was proposed by Vand [19] which theorized the gasification of metallic films using an infinite number of irreversible reactions with various activation energies which was used by Cai *et al.* [20] to model the pyrolysis of lignocellulosic

biomass, defined as organic matter comprised of cellulose, hemicellulose and lignin. Most computational pyrolysis simulations are of industrially applied reactors which are a mixture of particles and sand, modelled as porous media, a multi-fluid mixture or as discrete particles [21].

Pyrolysis simulations have been performed using Gpyro [22]. Gpyro originally utilized simple pyrolysis kinetics (single-component/multi-step) and was an isolated volume of biomass, not coupled to any gaseous domain. Recently, the 3D extension of Gpyro, Gpyro3D [23], was coupled with the Wildland-Urban Interface Fire Dynamics Simulator (WFDS) [24, 25], but simplified the pyrolysate in the gas-phase to only be a lumped fuel molecule, namely, $C_{3.4}H_{6.2}O_{2.5}$. A study by Gentile *et al.* [26] used the bioSMOKE framework [27] to model isolated, arbitrarily shaped particles of biomass and accounted for anisotropy that is natural in biomass materials.

During biomass burning, the presence of pyrolysis products alone is not enough to induce combustion and heat release. For this, an ignition source is required. In some cases, the temperature of pyrolysis products may be sufficiently high to lead to auto-ignition, but it is more common for lightning strikes, arson or faulty equipment to ignite pyrolysis gases [28]. Once a fire has begun, embers may serve as additional sources for ignition and propagation [29]. Predicting the production and transport of embers is, in itself, a research area of considerable importance, but in simulations at small scales the effects of embers can be mimicked by providing a "spark" or brief high temperature event that exceeds the activation energy of the pyrolysis gases and results in exothermic reactions associated with combustion.

As with simulations of chemical reactions during pyrolysis, detailed mechanisms for combustion of pyrolysis products can be prohibitively large. To model gas-phase combustion requires knowledge of the composition of gases exiting the solid fuel following pyrolysis along with the thermodynamic properties of each species and a kinetic reaction mechanism. As discussed above, the set of compounds found in practice is quite large, and most researchers have chosen to take a "lumped" approach to characterizing the gaseous fuel and describing the chemical kinetics. The dilemma that faces the researcher is that far more is known about pyrolysate composition than thermodynamic properties, reaction mechanisms and their rates for the larger species. For the lighter fractions such

as $CH_4$ and CO, thermodynamic properties are well known and there exist kinetic mechanisms that have been directly validated based on experimental flame data. For the larger hydrocarbons and oxygenated species, however, thermal decomposition pathways, thermochemical data and reaction rates are not universally available.

Even if a complete kinetic reaction mechanism were known for the gas-phase combustion of a given fuel type, inclusion of the mechanism in high-resolution simulations would likely overwhelm the available computational resources. Therefore, a reduced reaction mechanism of some kind must be used. There are two general approaches to developing such reduced mechanisms. One approach is to take the results of a pyrolysis model that predicts the light products of pyrolysis and then reduce an existing mechanism for the gas-phase chemistry. In this case, one could start with a well-known mechanism like GRI-Mech [30] and reduce it to a smaller skeletal model as in Zhou and Mahalingam [31]. The other approach is to take more detailed species data such as that generated by Jarvis *et al.* [32] and carry out the work of determining thermodynamic properties, reaction pathways, and rates. Then using a hierarchical approach similar to that outlined by Westbrook and Dryer [33], one then builds on existing mechanisms. An intermediate approach is to characterize classes of molecules (Jarvis' factors, for example) with lumped representative species. This is the approach taken, for example, by Ranzi *et al.* [34] in developing their detailed gas-phase mechanism.

These prior attempts to model pyrolysis, ignition, and combustion during biomass burning motivate the present thesis. In particular, reduced chemical models for pyrolysis and combustion are developed and implemented in computationally efficient simulations of biomass burning at small scales. The simulations are then validated using measurements from laser absorption spectroscopy for pyrolysis, ignition, and combustion of a small Douglas fir solid fuel sample.

## 1.1 Objectives and Research Questions

The work presented in this thesis outlines steps taken toward enabling more accurate and efficient simulations of biomass pyrolysis, ignition, and combustion. The complex nature of wildland fire spread at small scales is explored by coupling solid- and gaseous-regions and using complex

kinetics in both regions. In order to achieve this goal, the objective of developing efficient simulations of biomass pyrolysis, ignition and combustion is critical. While this overarching objective is lofty, to get there, the follow research questions have been posed:

- To what degree can the detailed, gas-phase, combustion kinetic models be reduced while still predicting bulk quantities (i.e., ignition delay time, laminar flame speed, heat release, etc.) and maintaining volatile species important to soot formation?
- Can multi-component/multi-specie pyrolysis and combustion kinetics be utilized in a single framework that consists of coupled solid and gas domains?
- Can highly reduced models (i.e., single-step, finite-rate chemistry or single-step, infinite-rate chemistry) be used to predict quantities of flaming biomass combustion?

## 1.2 Overview of Dissertation

In order to reduce the computational cost of high-fidelity numerical simulations of wildland fire, computationally efficient—yet still physically accurate—reduced chemical kinetic models are required for the prediction of gas-phase combustion. In Chapter 2, a detailed gas-phase combustion model is presented which is intractable for simulations due to its size. Direct Relation Graph with Error Propagation and Sensitivity Analysis (DRGEPSA) is used to remove species and reactions that are insignificant to the reaction pathway given specific sets of conditions (i.e., temperature, pressure, equivalence ratio and target species) to produce a skeletal model. The reduction process and three such models are presented for the combustion of gas-phase products resulting from the pyrolysis of Douglas fir. The theoretical computational savings enabled by these models are substantial when compared to detailed models on the basis of ignition delay time, peak temperature, volumetric heat release rate, laminar flame speed and extinction temperature. The reduction in number of species and reactions make the skeletal models more suitable for wildland fire simulations spanning large spatial and temporal scale ranges.

In Chapter 3, simulations of a validation experiment of pyrolysis and ignition of radiatively-heated Douglas fir are presented in the open-source framework of OpenFOAM [35] with the solver fireDyMFoam developed by Lapointe *et al.* [36, 37]. The simulations are compared on a basis of temporally resolved gas- and solid-phase temperature, solid-phase mass loss and water vapor mole fraction to an experiment performed by Makowiecki *et al.* [38] with reasonable agreement; general trends are captured temporally and in magnitude. This work begins to address the complexity of coupling the solid- and gaseous-regions, including adaptive mesh refinement (AMR) and introduces novel boundary conditions for modeling pyrolysate composition within OpenFOAM. A simplified framework utilizing only methane and water produced by pyrolysis and infinitely-fast chemistry.

As a possible solution to the disparity of spatial scales, high-resolution numerical simulations at much smaller scales (e.g., 10 m and below) can, in principle, be used to develop improved subgrid-scale models for landscape scale wildland fire simulations. As the scale of the simulations decreases, there is a greater need to more accurately model all relevant small-scale chemical and fluid processes. To adequately model fire spread, simulations must be able to resolve small-scale turbulent mixing, as well as capture the pyrolysis and subsequent gas-phase combustion of geometrically complex and spatially heterogeneous wildland fuels. The challenge of resolving turbulence can be addressed through advanced computational techniques such as AMR [39–41], but the chemical models used for pyrolysis and combustion must be sufficiently detailed without significantly increasing the computational cost.

In Chapter 4, the reduced chemical models that were introduced and developed in Chapter 2 are utilized in a computational study of a reacting plume. In addition to the three models, an additional highly reduced model is examined. Simulations using fireFoam are performed to mimic the pyrolysate that diffuses off the block of Douglas fir from Chapter 3 with the use of tabulated chemistry. These reduced chemical models are compared with infinitely-fast combustion of a lumped molecule in order to compare the most simple form of chemistry against higher fidelity models. Additionally, a novel, objective method for quantifying the dominant frequency in a reacting flow is introduced which requires additional study for validation.

Chapter 5 contains some final remarks, and ultimately will provide some answers to the objectives and research questions posed earlier. Future additions to this work will be posed with a general direction of interest, specifically for any questions or objectives not met by this work.

## 1.3 Research Contributions

This work has resulted in two first-author journal articles (presented in Chapters 2 and 3):

(1) J. F. Glusman, K. E. Niemeyer, A. S. Makoweicki, N. T. Wimer, C. B. Lapointe, G. B. Rieker, P. E. Hamlington, J. W. Daily, Reduced gas-phase kinetic models for burning of douglas fir, Frontiers in Mechanical Engineering 5 (2019).

(2) J. F. Glusman, C. B. Lapointe, A. S. Makoweicki, S. Simons-Wellin, G. B. Rieker, J. W. Daily, P. E. Hamlington, Validation of computationally efficient simulations of douglas fir pyrolysis and combustion using time-resolved frequency comb laser measurements, Frontiers in Forests and Global Change 5 (2022).

Additionally, this work contributed to several co-authored journal publications:

(1) A. S. Makowiecki, D. I. Herman, N. Hoghooghi, E. F. Strong, R. K. Cole, G. Ycas, F. R. Giorgetta, C. B. Lapointe, J. F. Glusman, J. W. Daily, P. E. Hamlington, N. R. Newbury, I. R. Coddington, G. B. Rieker, Mid-infrared dual frequency comb spectroscopy for combustion analysis from 2.8 to 5 $\mu$m, Proceedings of the Combustion Institute (2020).

(2) C. Lapointe, N. T. Wimer, J. F. Glusman, A. S. Makowiecki, J. W. Daily, G. B. Rieker, P. E. Hamlington, Efficient simulation of turbulent diffusion flames in openfoam using adaptive mesh refinement, Fire Safety Journal 111 (2020) 102934.

(3) A. Makowiecki, J. Steinbrenner, N. Wimer, J. Glusman, C. Lapointe, J. Daily, P. Hamlington, G. Rieker, Dual frequency comb spectroscopy of solid fuel pyrolysis and combustion: Quantifying the influence of moisture content in douglas fir, Fire Safety Journal 116 (2020) 103185.

(4) C. Lapointe, N. T. Wimer, S. Simons-Wellin, J. F. Glusman, G. B. Rieker, P. E. Hamlington, Efficient simulations of propagating flames and fire suppression optimization using adaptive mesh refinement, Fluids 6 (2021) 323.

(5) N. T. Wimer, M. S. Day, C. Lapointe, M. A. Meehan, A. S. Makowiecki, J. F. Glusman, J. W. Daily, G. B. Rieker, P. E. Hamlington, Numerical simulations of buoyancy-driven flows using adaptive mesh refinement: structure and dynamics of a large-scale helium plume, Theoretical and Computational Fluid Dynamics 35 (2021) 61–91.

This work was presented at various conferences:

(1) J. F. Glusman, C. B. Lapointe, A. S. Makowiecki, S. Simons-Wellin, G. B. Rieker, J. W. Daily, and P. E. Hamlington. Computationally Efficient Simulations of Douglas Fir Pyrolysis and Combustion. 12th U.S. National Combustion Meeting - Fire Research, held virtually, May 24-26, 2021.

(2) J. F. Glusman, G. B. Rieker, J. W. Daily, and P. E. Hamlington. Wildland Fire: A cooperative effort of simulations, chemical modelling and lasers. 2020 Graduate Engineering Annual Research & Recruitment Symposium - Air Quality, Boulder, Colorado, February 21 2020.

(3) J. F. Glusman, K. E. Niemeyer, A. S. Makowiecki, N. T. Wimer, C. Lapointe, G. B. Rieker, P. E. Hamlington, and J. W. Daily. Initial Verification of a Reduced Combustion Model of Douglas Fir. Rocky Mountain Fluid Mechanics Symposium - Summer 2019 Meeting, Boulder, Colorado, July 29 2019.

(4) J. F. Glusman, A. S. Makowiecki, N. T. Wimer, K. E. Niemeyer, G. B. Rieker, P. E. Hamlington, and J. W. Daily. A Chemical Kinetic Mechanism Reduction for Wildland Fire Direct Numerical Simulation and Experimental Validation. Rocky Mountain Fluid Mechanics Symposium - Fall 2018 Meeting, Boulder, Colorado, August 13 2018.

(5) J. F. Glusman, A. S. Makowiecki, N. T. Wimer, K. E. Niemeyer, G. B. Rieker, P. E. Hamlington, and J. W. Daily. A Chemical Kinetic Model Reduction and Pyrolysis Model for Wildland Fire Direct Numerical Simulation. Western States Section of the Combustion Institute - Spring 2018 Meeting, Bend, Oregon, March 25-27 2018.

# Chapter 2

## Reduced Gas-Phase Kinetic Models for Burning of Douglas Fir

*"Truth is much too complicated to allow anything but approximations."*

— John von Neumann

### 2.1 Introduction

Although existing biomass pyrolysis models are not excessively large, gas-phase combustion models routinely involve hundreds or even thousands of different species and reactions. For example, Ranzi *et al.* [34] have provided a gas-phase biomass combustion model—which is the basis for the present skeletal models—that contains 4,533 reactions and 137 species. Skeletal and other reduced models are typically an order of magnitude smaller. The widely-used multi-step DRM19 kinetic model, for instance, is a 19 species (plus $N_2$ and Ar), 84 reaction reduced model for methane combustion based on GRI-Mech 1.2 [30].

In the following, the development of three new skeletal chemical kinetic models for gas-phase combustion of Douglas fir pyrolysis products is outlined. The three models are targeted at large-scale simulations on high-performance computing resources, but are intended to provide three different levels of accuracy and computational cost. Users may thus choose the model best suited to their needs and available computational resources. All skeletal mechanisms include a similar number of species (i.e., 71 and 54 species), but have vastly different numbers of reactions (i.e., 1,179 versus 637 versus 204).

The skeletal models are obtained by reducing the detailed chemical kinetic model for gas-

phase biomass combustion from Ranzi *et al.* [34]. The reduction is performed using the directed relation graph with error propagation and sensitivity analysis method in a perfectly-stirred reactor (PSR). It is then shown that all three skeletal models introduce quantifiable error, as compared to the detailed model, for various properties of premixed and diffusion flames.

## 2.2 Methodology

The overall reduction procedure tracks ignition delay time error in a constant-pressure, fixed volume PSR for the combustion of gases resulting from the pyrolysis of Douglas fir. In the following, the model and procedure used to obtain the Douglas fir pyrolysis products are described, followed by descriptions of the detailed chemical kinetic model and the reduction process.

### 2.2.1 Pyrolysis Model

The pyrolysis kinetic model is that of Debiagi *et al.* [45], which includes extractives and is a refined version of the model published by Corbetta *et al.* [46]. The model involves 28 reactions and 47 species (including volatile, non-volatile, and condensed-phase species) and provides pathways for the thermal decomposition of the three main polymer components of wood: cellulose, hemicellulose, and lignin, in addition to two extractives. It predicts light molecules directly, while heavy molecules are described by lumped species. The advantage of using this model is that the gaseous lumped product species correspond to those in an associated gas-phase detailed combustion model [34], which is the starting point for the model reduction performed here. Of the 47 species in the pyrolysis mechanism, 18 are volatile.

The major components of wood are polymers, and the pyrolysis model reflects this by starting with de-polymerization reactions, although in a highly simplified manner. Cellulose is assumed to transform into active cellulose; i.e., a reactive form that leads to the monomeric form and other products like levoglucosan. Hemicellulose is assumed to decompose into intermediate species `HCE1` and `HCE2` that successively decompose with different activation energies, with different propensities to char. Lignin is assumed to be composed of `LIG-C`, `LIG-O`, and `LIG-H` (carbon, oxygen, and hy-

drogen rich derivatives of the $\beta$-O-4 molecule, respectively), that then decompose into intermediate components that lead to other products [34].

Extractives extend the applicable types of biomass that can be represented with this kinetic model. Previous versions of the pyrolysis mechanism (e.g., Corbetta *et al.* [46]) were only valid for specific types of biomass, depending on their carbon and hydrogen makeup. Extractives fall into two categories: hydrophilic and hydrophobic. Debiagi *et al.* [45] chose to use a tannin (`TANN`) as the hydrophilic extractive and a triglyceride (`TGL`) as the hydrophobic extractive.

### 2.2.2 Douglas Fir Pyrolysis Products

To carry out reduction of the gas-phase kinetic model, a realistic set of gas-phase pyrolysis products is required as input to the gas-phase calculations. Therefore, simulations were ran using the pyrolysis model described in the previous section over a range of times and temperatures. This requires selecting a target wood species to work with, since the initial concentrations of cellulose, hemicellulose, and lignin vary by species. Douglas fir was selected because of its widespread availability and native presence in the Rocky Mountain region. The initial mole fractions of cellulose, hemicellulose, `LIG-C`, `LIG-H`, `LIG-O`, `TANN`, and `TGL` for Douglas fir are obtained from References [45, 47, 48]; Table 2.1 lists these in terms of percentage by weight.

The pyrolysis model is solved using an experimentally measured temperature time series (shown in Figure 2.1) as input. In the experiments, Douglas fir samples were heated with a

Table 2.1: Weight percentages of the main components of Douglas fir, including molecular structures.

| Molecule | Structure | Weight Percentage |
|---|---|---|
| Cellulose | $C_6H_{10}O_5$ | 44.06 |
| Hemicellulose | $C_6H_8O_5$ | 22.01 |
| `LIG-C` | $C_{15}H_{14}O_4$ | 4.73 |
| `LIG-H` | $C_{20}H_{22}O_{10}$ | 12.05 |
| `LIG-O` | $C_{22}H_{28}O_9$ | 10.89 |
| `TANN` | $C_{15}H_{12}O_7$ | 1.26 |
| `TGL` | $C_{57}H_{100}O_7$ | 5.01 |

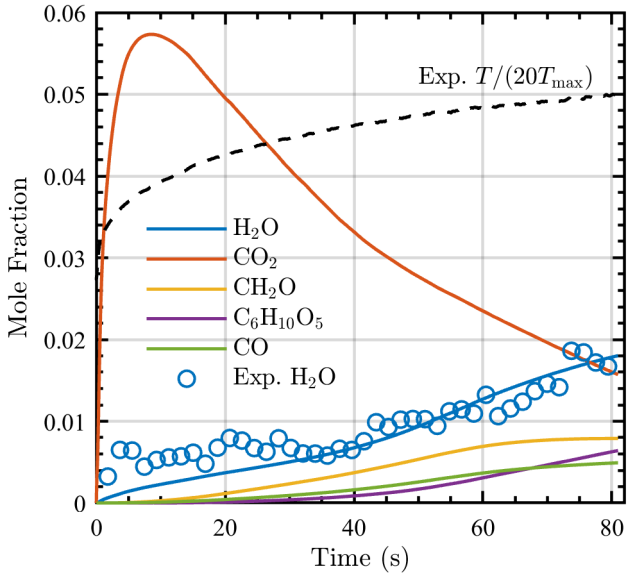


Figure 2.1: Mole fraction time series of the five most prevalent (by mole fraction at 80 s) volatile pyrolysis products (indicated by lines) and the corresponding experimentally measured $H_2O$ mole fraction (indicated by open circles). The normalized experimental temperature times series is also shown (black dashed line), where $T_{\max} = 639$ K.

cone-calorimeter while simultaneously measuring surface temperature (via an infrared camera), gas temperature, and $H_2O$ mole fraction. The latter two quantities were measured using dual-frequency comb laser diagnostics [49]. Since the model describes pyrolysis (i.e., decomposition at high temperature in the absence of air), an approximately stoichiometric amount of air was assumed for comparison with the experimental dataset. The formation of pyrolysis gases is modeled using the surface temperature measured by the infrared camera, prior to any combustion occurring. More extensive details on the experiments are available in Makowiecki *et al.* [38].

Figure 2.1 shows the evolution of the top five volatile pyrolysis products as a function of time; at 80 s, these species account for approximately 74% of the total moles of the pyrolysate in the gas-phase. This figure indicates that the pyrolysis model accurately captures the production of $H_2O$ vapor measured experimentally.

### 2.2.3 Detailed Combustion Model

The detailed gas-phase kinetic model `bio1412` from the CRECK modeling group is used as the starting point for the reduced skeletal models. This model is publicly available at their website (`http://creckmodelling.chem.polimi.it`), with verification data given by Ranzi *et al.* [34]. The model contains 4,533 reactions and 137 species and is built upon earlier work from the CRECK group [50]. Although this model has been shown to give good agreement for the gas-phase combustion of solid fuel pyrolysis gases [34], it is generally too large for inclusion in already demanding simulations of wildland fire. Consequently, in the following the process of reducing this model to a size that is appropriate for high-fidelity numerical simulations is described.

### 2.2.4 Reduction Methodology

The CRECK detailed gas-phase combustion model is reduced using the Model Automatic Reduction Software (MARS) package [51–54]. The reduction employs the directed relation graph with error propagation (DRGEP) and sensitivity analysis (SA) method, followed by reaction elimination, which Niemeyer and colleagues have shown to be effective for reducing various surrogate fuel models.

Briefly, the process begins by applying DRGEP, which determines the importance of each species to the production or consumption of chosen target species (e.g., fuel, oxidizer, important pollutants). Next, a "greedy" SA removes individual species one-by-one and evaluates the error induced; it removes the species that least influence error and repeats the process on the remaining species until reaching the specified error limit. The error limit is determined by comparing predictions of the full, detailed kinetic model via autoignition and PSR simulations across expected conditions (e.g., pressure, temperature, equivalence ratio, and initial reactants) with those of the skeletal model. Ignition delay time and points along the upper PSR temperature response curve are chosen as metrics for the reduction, consistent with typical target parameters for premixed combustion mechanisms. Then, the contributions of each remaining reaction are examined, with

the goal of eliminating reactions that are unimportant to the overall progression of the kinetic model, while remaining below the specified error tolerance. The final resulting model is considered the skeletal model.

This process is carried out for each targeted condition (e.g., pressure, temperature, equivalence ratio, initial reactants), resulting in a single skeletal model that consists of the union of species remaining over all conditions. This guarantees that the reduced model maintains error below the specified limit for autoignition and PSR results. Further, targeted species cannot be removed, regardless of their impact on the overall kinetics.

## 2.3 Results

### 2.3.1 Skeletal Combustion Models

Reduction calculations were performed using the fuel set composed of all 18 gas-phase pyrolysis products. The pressure was set to 1 atm, with temperatures ranging from 800 to 2000 K and equivalence ratios from 0.5 to 1.5. The wide range of conditions included in the reduction reflects the similarly wide-ranges of temperatures and equivalence ratios found in real-world wildland fires.

To create a robust gas-phase combustion model, various sets of products from the pyrolysis model were used in the reduction, corresponding to the products at 20, 50, and 80 s (shown in Figure 2.1). However, the resulting reduced gas-phase models were all roughly the same size, with similar numbers of species and reactions. Therefore, only the reductions on the final pyrolysis products at 80 s will be discussed in the following sections.

Figure 2.2 shows the reduction process via DRGEPSA for the number of species remaining in the kinetic model as a function of error limit. Applying DRGEP with a maximum error of 30% (in ignition delay time and peak temperature in a PSR) to the detailed kinetic model removed 75 species and any reaction containing them, leaving 62 species. At this point in the reduction, the error in ignition delay time between the detailed model and the reduced model was approximately 21%. Applying sensitivity analysis removed 8 additional species and their associated reactions,

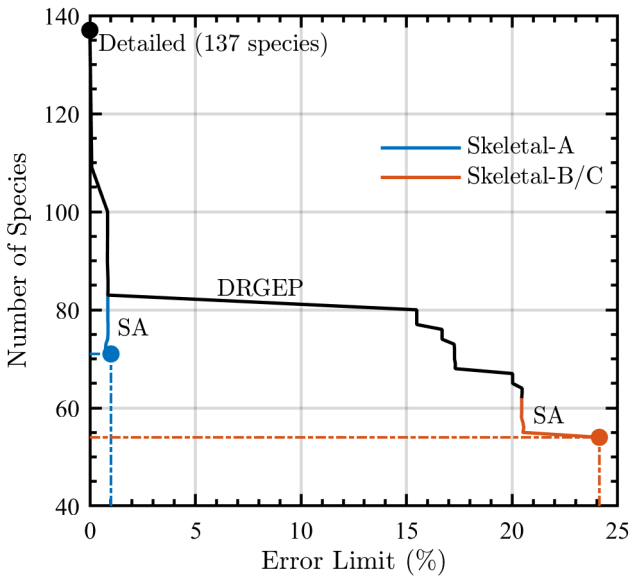


Figure 2.2: Number of species as a function of error limit during the reduction of the detailed model using the directed relation graph with error propagation (DRGEP) and sensitivity analysis (SA) method. Dash-dot lines indicate the number of species for the given error limit in skeletal models A (blue lines) and B (red lines) prior to the reaction elimination step (which produces Skeletal-C).

resulting in a reduced model with 54 species and 637 reactions, giving approximately 24% error as compared to the detailed model. The reaction elimination step removed an additional 433 reactions, yielding a skeletal model with 204 reactions. For the ignition delay time in a PSR, this final skeletal model has 82.6% maximum error when compared to the detailed model. In total, the skeletal model retains 54 species and 204 reactions, corresponding to 39.4% of the total number of species and 4.5% of the total number of reactions in the detailed model.

During the DRGEP process, Figure 2.2 indicates a significant increase in error at 81 species, corresponding to a jump from below 1% to greater than 15% error. Consequently, a second reduced model with 1% error for gas-phase combustion was created, hereby noted Skeletal-A. Due to the large error increase associated with the reaction elimination step, the highly reduced model will be denoted Skeletal-C and Skeletal-B being the reduced model produced by DRGEPSA with 30% error. The numbers of species and reactions in these three models are summarized in Table 2.2, along with the detailed model. After the DRGEPSA process, the Skeletal-A model has only 0.8% error in ignition delay time compared to the detailed model, which increases to 24.1% error for

Table 2.2: Detailed and skeletal model details, indicating the final number of species and reactions, as well as the error in the ignition delay time with respect to the detailed model.

| Model | # Species | # Reactions | Error % |
|---|---|---|---|
| Detailed | 137 | 4,533 | - |
| Skeletal-A | 71 | 1,179 | 0.81 |
| Skeletal-B | 54 | 637 | 24.1 |
| Skeletal-C | 54 | 204 | 82.9 |

Skeletal-B and 82.9% after the reaction elimination step in Skeletal-C. With the introduction of tabulated and dimensional reduction of chemistry, models on the order of one-thousand reactions and one-hundred species are suitable for some computations [55], and thus all the skeletal models developed here are sufficiently compact for implementation in high-resolution simulations.

### 2.3.2 Validation of Skeletal Models

To validate the accuracy of the reduced skeletal models, which were obtained based on consideration of the ignition delay time in PSR calculations, constant-volume ignition delays, PSR peak temperatures, volumetric heat-release rates, laminar flame speeds, and diffusion flame extinction points from the detailed model are compared to those of the skeletal model.

Figure 2.3 shows that all three skeletal models match the ignition delay times of the detailed model for equivalence ratios from 0.5 to 1.5 over a wide range of temperatures. Although discrepancies do exist between the models at low temperatures, such temperatures are not of primary interest for wildland fire. In general, as expected, the larger Skeletal-A model is in better agreement with the detailed model, as compared to the Skeletal-B and Skeletal-C models.

To assess the importance of the error in ignition delay, the absolute error in the ignition delay time is compared to an approximate characteristic turbulent mixing time $\tau_{\text{mix}}$. This time is estimated as $\tau_{\text{mix}} \approx 0.1$ s based on a convective velocity of 1 cm/s and a characteristic length of 1 mm. For most practical conditions, the ignition delay will be dominated by mixing and therefore the error introduced by the reduction is reasonably small, as seen in Figure 2.4. The highest error occurs at low temperatures where the characteristic turbulent mixing time would be much longer

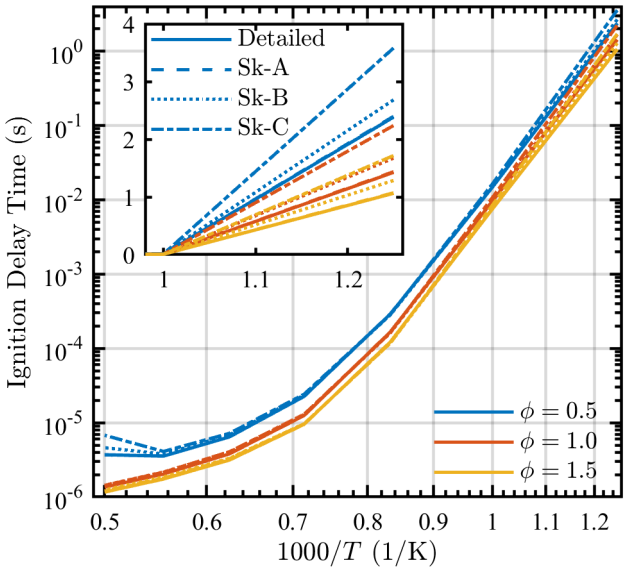


Figure 2.3: Ignition delay as a function of $1000/T$ in a PSR at equivalence ratios $\phi = [0.5, 1.0, 1.5]$ and $P = 1$ atm for the detailed (solid lines), Skeletal-A (dashed lines), Skeletal-B (dash-dot lines), and Skeletal-C (dotted lines) models. The inset shows ignition delay time versus $1000/T$ for lower temperatures.

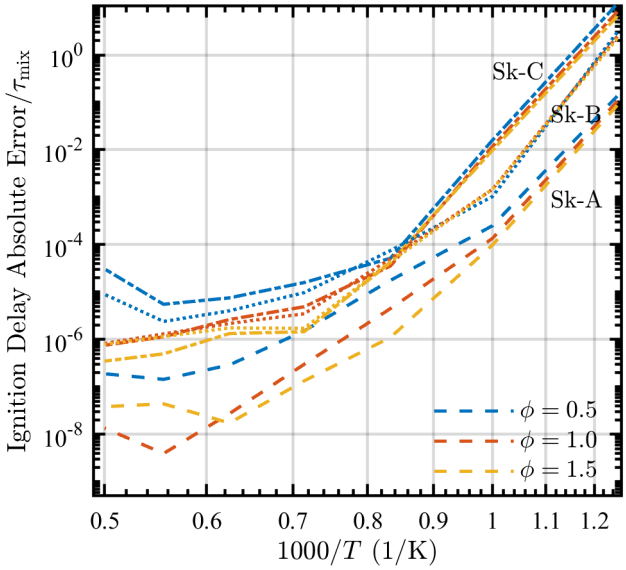


Figure 2.4: Absolute error relative to the mixing time $\tau_{\text{mix}} = 0.1$ s as a function of $1000/T$ in a PSR at equivalence ratios $\phi = [0.5, 1.0, 1.5]$ and $P = 1$ atm for the detailed (solid lines), Skeletal-A (dashed lines), Skeletal-B (dash-dot lines), and Skeletal-C (dotted lines) models.

than the approximate one used here, due to a lower convective velocity. While the deviations at $T = 2{,}000$ K look large, it must be kept in mind that the non-dimensional errors are on the order

of $10^{-4}$ to $10^{-8}$, and therefore trivial for this application when compared to the mixing time.

The PSR calculations performed during the reduction process provide the peak temperature and the volumetric heat-release rate as functions of residence time. These results are shown in Figures 2.5 and 2.6 for the detailed and skeletal models over equivalence ratios from 0.5 to 1.5.

For each of the models and at all equivalence ratios, the peak temperatures in Figure 2.5 decrease as the residence time decreases, consistent with the increased incidence of incomplete combustion for small residence times. The detailed and Skeletal-A models are in nearly perfect agreement, with small deviation in Skeletal-B model for all conditions considered. However, peak temperatures from the Skeletal-C model show a slight discrepancy with respect to the detailed and Skeletal-A and B models, but the correct trends with varying residence time are nevertheless still captured.

The variation of the volumetric heat-release rate with residence time is nearly identical for the detailed and all three skeletal models, as shown in Figure 2.6. In particular, the volumetric heat release rate increases substantially as the residence time decreases. This occurs because more

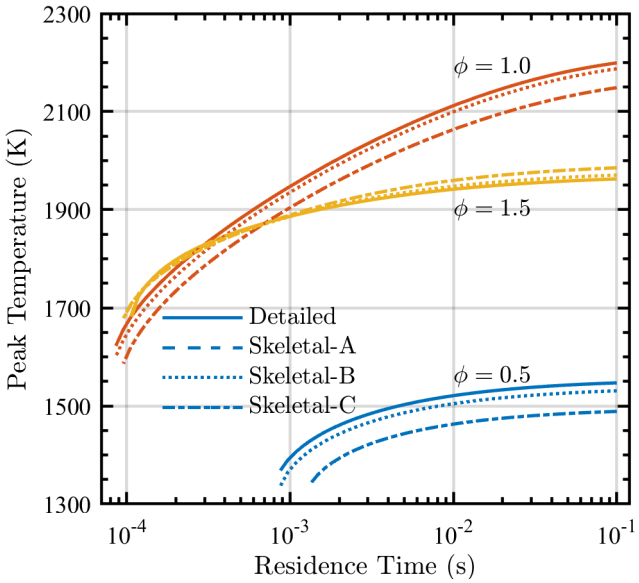


Figure 2.5: Peak temperature versus residence time in a PSR at equivalence ratios $\phi = [0.5, 1.0, 1.5]$ and $P = 1$ atm for detailed (solid lines), Skeletal-A (dashed lines), Skeletal-B (dash-dot lines), and Skeletal-C (dotted lines) models.

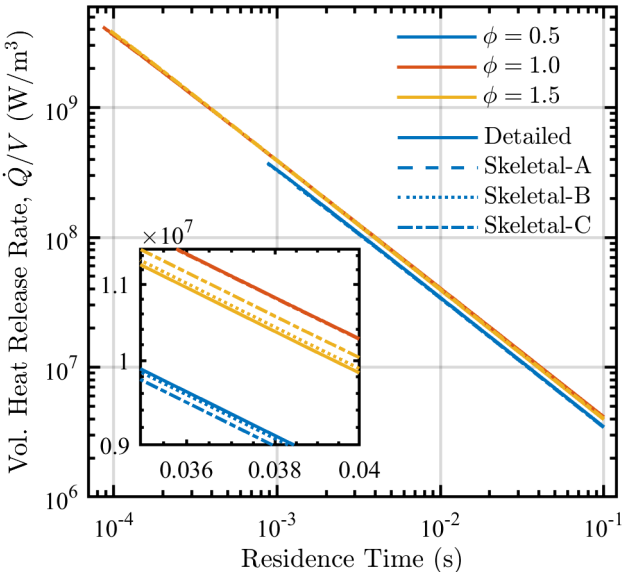


Figure 2.6: Volumetric heat release rate versus residence time in a PSR at equivalence ratios $\phi = [0.5, 1.0, 1.5]$ and $P = 1$ atm for detailed (solid lines), Skeletal-A (dashed lines), Skeletal-B (dash-dot lines), and Skeletal-C (dotted lines) models.

heat must be removed relative to the volume in order to maintain a constant-pressure reactor.

To validate the model reduction in non-homogeneous flame configurations, laminar flame speeds were computed for a one-dimensional premixed flame in Cantera [56] using both detailed and skeletal chemical kinetic models with mixture-averaged diffusion coefficients. The physical domain length was 50 cm, the reactants were at a temperature of 300 K and pressure of 1 atm, and flame speeds were computed over a range of equivalence ratios. Figure 2.7 shows that, once again, there is essentially no discrepancy between the detailed and Skeletal-A models. Although errors are larger for the Skeletal-B and Skeletal-C models, these errors may be tolerable in simulations of real-world fires given the typically larger errors introduced by other physical models in the simulations (e.g., for turbulence, heat transfer, and fuel properties), as well as uncertainties in boundary and initial conditions.

Because wildland fires exhibit characteristics of both premixed and diffusion flames, the skeletal models were also used to compute the extinction temperature as a function of maximum strain rate for an opposed-jet diffusion flame. The simulations were performed using Cantera in an

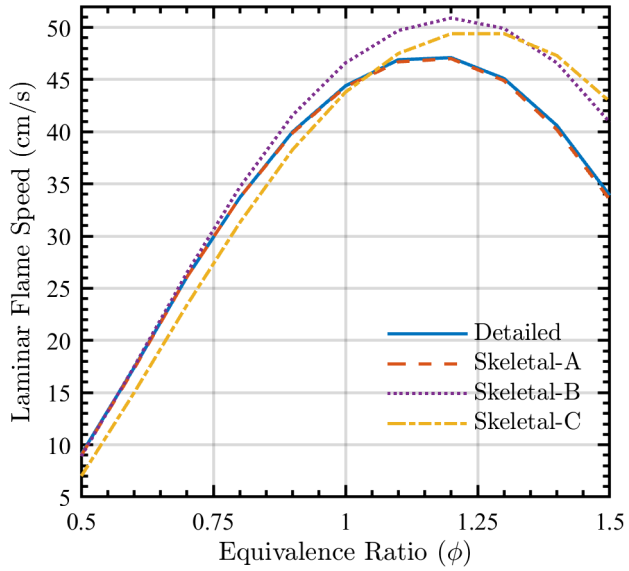


Figure 2.7: Laminar flame speed for a one-dimensional premixed flame as a function of equivalence ratio $\phi$ for detailed (solid lines), Skeletal-A (dashed lines), Skeletal-B (dash-dot lines), and Skeletal-C (dotted lines) models. The reactants were at temperature 300 K and pressure 1 atm.

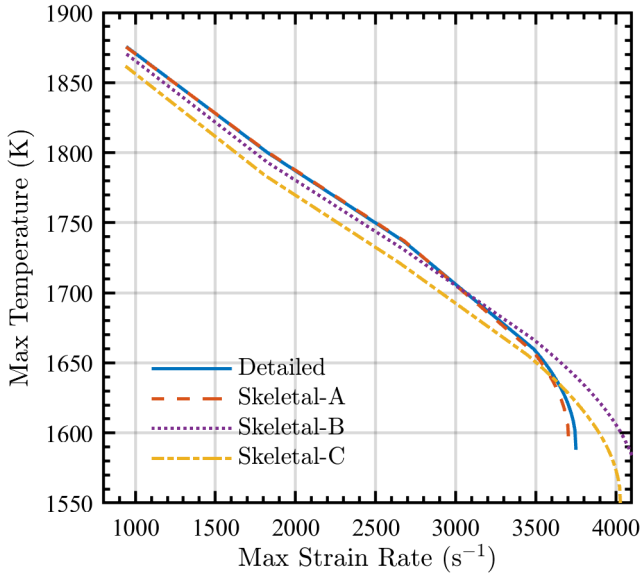


Figure 2.8: Maximum temperature in an opposed-jet diffusion flame as a function of maximum strain rate for detailed (solid lines), Skeletal-A (dashed lines), Skeletal-B (dash-dot lines), and Skeletal-C (dotted lines) models. The conditions of the opposed-jet configuration were $T_{\text{fuel}} = 500$ K, $T_{\text{air}} = 300$ K, and $P = 1$ atm.

18 mm domain with radiation. The fuel and air temperatures were $T_{\text{fuel}} = 500$ K and $T_{\text{air}} = 300$ K, respectively, and the pressure was $P = 1$ atm.

Table 2.3: Root mean square (RMS) and maximum error percentages from the Skeletal-A, Skeletal-B, and Skeletal-C reduced models for various properties of interest over the range of conditions considered in this study. Errors are computed relative to results from the detailed model. Properties are computed for a perfectly stirred reactor (PSR), a 1D laminar premixed (LP) flame, and an opposed-jet diffusion (OJD) flame.

| | Skeletal-A Error | | Skeletal-B Error | | Skeletal-C Error | |
|---|---|---|---|---|---|---|
| | RMS (%) | Max (%) | RMS (%) | Max (%) | RMS (%) | Max (%) |
| Ign. Delay Time (PSR) | 0.40 | 0.81 | 9.40 | 24.13 | 28.82 | 82.85 |
| Peak Temp. (PSR) | 0.03 | 0.33 | 0.73 | 1.46 | 2.54 | 6.17 |
| Vol. Heat Rel. Rate (PSR) | 0.01 | 0.13 | 0.34 | 0.82 | 1.24 | 2.65 |
| Flame Speed (LP) | 0.64 | 1.18 | 9.12 | 20.65 | 13.5 | 26.5 |
| Extinction Temp. (OJD) | 0.52 | 1.40 | 1.00 | 1.98 | 0.54 | 1.16 |

The results shown in Figure 2.8 indicate that the reduction process generally has minimal effect on the relation between the maximum temperature and strain rate at the extinction point. As with other metrics for the PSR and premixed flame, the Skeletal-A model is in nearly perfect agreement with the detailed model, and the Skeletal-B and Skeletal-C models display relatively small discrepancies when compared to the detailed model.

As a quantitative summary of the errors in the skeletal models with respect to the detailed model, Table 2.3 shows the root-mean square (RMS) and maximum errors for various quantities of interest over all conditions (i.e., temperatures and equivalence ratios) considered in the present study. In general, the errors for the Skeletal-A model are extremely low, the errors for the Skeletal-B model are below 30% for all metrics considered. As expected, the Skeletal-C model shows the greatest amount of error, with the RMS errors maintained below 30%. The maximum errors across all reduced models occurs in the ignition delay time. As noted before, these errors are likely to be acceptable in most high-fidelity simulations of wildland fire given the significant increase in computational efficiency resulting from the reduction in number of species and reactions. Moreover, although the errors in ignition delay time are somewhat large in relative terms, they are small in absolute terms when compared to characteristic flow mixing times.

## 2.4 Conclusions

Three new skeletal chemical kinetic models have been developed and validated for the combustion of gas-phase products resulting from the pyrolysis of Douglas fir. The skeletal models were obtained by using the directed relation graph with error propagation method, "greedy" sensitivity analysis, and unimportant reaction elimination to reduce a detailed gas-phase model with 137 species and 4,533 reactions.

The three skeletal models had different sizes and resultant errors: the larger 71 species, 1,179 reaction skeletal model had a maximum error of roughly 1% for combustion properties of interest over a wide range of conditions, while the more reduced model with 54 species and 637 reactions yielded maximum errors of about 20% in ignition delay and laminar flame speed. The smallest 54 species, 204 reaction model had a maximum error of roughly 83% in ignition delay, with an average maximum error of 24%. These errors are reasonable given the complexity and uncertainty involved in modeling solid biomass combustion, although the larger skeletal model is preferable if sufficient computational resources are available to allow its integration within high-fidelity simulations of wildland fire. It should also be noted that the largest errors were observed for all three skeletal models in the prediction of the ignition delay time, but these errors were small in absolute terms, particularly when compared to characteristic flow mixing times.

The use of additional performance measures in different flows, such as diffusion flames, as targets for MARS or it's replacement, pyMARS, would be of interest moving forwards to reduce biomass combustion mechanisms.

*This chapter is based on a publication titled "Reduced Gas-Phase Kinetic Models for Burning of Douglas Fir" that was published in Frontiers in Mechanical Engineering* [42].

# Chapter 3

# Validation of Computationally Efficient Simulations of Douglas Fir Pyrolysis Using Time-Resolved Frequency Comb Measurements

*"Knowledge, like air, is vital to life. Like air, no one should be denied it."*

— V, *Alan Moore, V for Vendetta*

## 3.1 Introduction

The purpose of this chapter to is to introduce a numerical framework using large eddy simulations (LES) with adaptive mesh refinement (AMR) in OpenFOAM to simulate the solid wood combustion experiment performed by Makowiecki *et al.*[38]. In this experiment, simultaneous *in situ* measurements of mass loss, heat flux, optical imaging, surface temperature, gas-phase temperature, and water vapor concentration were made for a fuel sample under a cone calorimeter. The measurements specifically focused on the pyrolysis of dry Douglas fir and the gas-phase ignition and combustion of pyrolysis products. The experiment had carefully controlled boundary conditions, enabling the use of the resulting measurements for simulation validation, and the diagnostic suite was non-intrusive. The surface temperature of the fuel sample was measured with a calibrated infrared imaging camera and simultaneous gas-phase temperature and water vapor concentration were measured with near-infrared frequency comb laser absorption spectroscopy [57, 58]. This experiment thus combined both traditional and state-of-the-art quantitative diagnostics to provide rich time-resolved data for simulation validation.

The simulations presented here use fireDyMFoam [37], a new OpenFOAM solver based on

fireFoam [59] that allows the use of load-balanced AMR for computationally efficient simulations of various types of fire spread problems. Here we add a custom boundary condition based on a multi-step pyrolysis kinetic model to capture the composition of gas-phase pyrolysis products, and compare the simulation and experimental results both pre- and post-ignition. The use of AMR has the potential to enable computationally tractable simulations that capture large- and small-scale terrain, as well as detailed fuel features. Simulations that include such physically relevant details while incorporating physics- based modeling could serve as the basis for new subgrid-scale models for existing landscape-scale fire spread modeling efforts. However, before implementing these tools, small-scale tests in a more controlled scenario must be understood.

## 3.2 Experimental Description

The experimental data used for simulation validation in this study were previously presented and described by Makowiecki *et al.* [38]. The experimental configuration is shown in Figure 3.1 and consists of a $[120 \times 40 \times 20]$ mm oven-dried (85°C) Douglas fir fuel sample placed on a load cell (for mass measurements) and positioned beneath a cone calorimeter. The cone calorimeter generated a 21.9 kW/m$^2$ heat flux at the center of the sample, with uniformity over the full sample within 16% of the heat flux measured at the center. A calibrated infrared camera (FLIR A655SC) was used to measure the surface temperature of the sample, while gas-phase temperature and species mole fractions were measured with near-infrared frequency comb laser absorption spectroscopy [38, 57, 58].

This diverse suite of diagnostics provides simultaneous time-resolved measurements of surface temperature, mass loss, and line-of-sight absorption-weighted average gas-phase temperature and water mole fraction, nominally 4 mm above the surface. Additional details of the experimental setup and results can be found in the study of fuel moisture effects by Makowiecki *et al.* [38]. These experiments contained a spark igniter operating at several Hz near the outer-surface of the wood, which ignited the pyrolysate, on average, 89 s after the experiment began.

The experiment was repeated seven times and the variability from each experiment is indi-

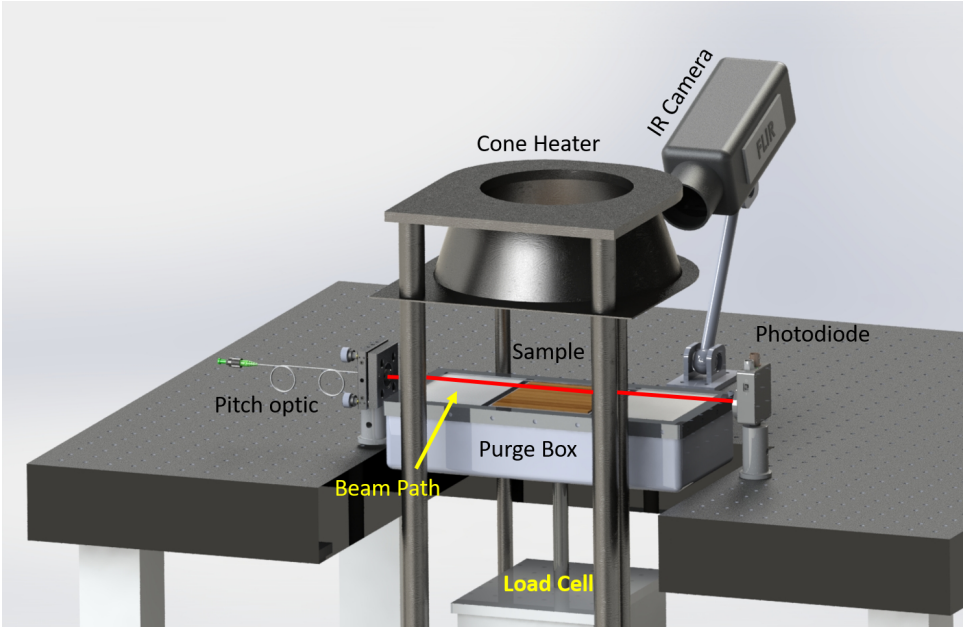


Figure 3.1: Experimental setup showing the configuration of the cone calorimeter, infrared (IR) camera, frequency comb laser beam path, and load cell.

cated in the results figures shown later in this paper. Because the physical properties of the samples have a large influence on the gas-phase simulation results, great care was taken while carrying out the experiments to completely dry the wood samples, accurately calculate the starting mass, and characterize the heat flux to the wood surface.

Although these small-scale experiments do not represent the full complexity found in real-world wildland fires, they do allow careful control of boundary conditions, as well as the ability to isolate variables of interest (e.g., heat flux and fuel moisture content). For the sake of having quantifiable boundary conditions for velocity and pressure, experiments were performed in a quiescent environment. Thus, these experiments are ideal for studying the detailed physical and chemical processes that must be modeled in simulations of wildland fuel pyrolysis and combustion. Experiments with additional fuel types were performed but the data has not yet been published; simulations of these other experiments are left as an important direction for future research.

## 3.3 Computational Solver

The numerical simulations are performed in OpenFOAM [35] using an extension of the fireFoam solver [59] called fireDyMFoam [36, 37]. Initially developed for simulations of pool fires [59], fireFoam has been used to model industrial fire problems in a number of different contexts and configurations [60–64]. The fireDyMFoam solver retains the physical modeling present in fireFoam, but additionally incorporates AMR and dynamic re-balancing of computational processors to enable computationally efficient, yet high-resolution, simulations of fire spread and suppression. This solver has been described in more detail by Lapointe *et al.* [36, 37], where the number of cpu-hours required for AMR simulations was reduced by roughly a factor of five compared to equivalently resolved static mesh simulations, and is used here to perform three-dimensional LES of solid fuel pyrolysis and combustion in coupled gas- and solid-phase regions.

### 3.3.1 Governing equations

Within the gaseous domain, the Favre-filtered compressible Navier-Stokes equations are solved along with conservation equations for mass, total enthalpy, and reacting species. These equations are given as [37]

$$\frac{\partial \rho}{\partial t} + \boldsymbol{\nabla} \cdot (\rho \boldsymbol{U}) = 0\,, \tag{3.1}$$

$$\frac{\partial (\rho \boldsymbol{U})}{\partial t} + \boldsymbol{\nabla} \cdot (\rho \boldsymbol{U}_i \boldsymbol{U}_j) = -\boldsymbol{\nabla} p_{\mathrm{rgh}} + \boldsymbol{\nabla} \cdot \tau_{ij} + \rho \boldsymbol{g}\,, \tag{3.2}$$

$$\frac{\partial \left[\rho (h + K)\right]}{\partial t} + \boldsymbol{\nabla} \cdot [\rho \boldsymbol{U} (h + K)] = \boldsymbol{\nabla} \cdot [\alpha_{\mathrm{eff}} \boldsymbol{\nabla} (\rho h)] + \frac{\partial p}{\partial t} + Q_{\mathrm{rxn}} + Q_{\mathrm{rad}}\,, \tag{3.3}$$

$$\frac{\partial (\rho Y_i)}{\partial t} + \boldsymbol{\nabla} \cdot (\rho \boldsymbol{U} Y_i) = \boldsymbol{\nabla} \cdot [\alpha_{\mathrm{eff}} \boldsymbol{\nabla} (\rho Y_i)] + \rho \omega_i\,, \tag{3.4}$$

$$\tau_{ij} = \boldsymbol{\nabla} \cdot \left[\mu (\boldsymbol{\nabla} \boldsymbol{U} + (\boldsymbol{\nabla} \boldsymbol{U})^T) - \lambda (\boldsymbol{\nabla} \cdot \boldsymbol{U}) \boldsymbol{I}\right]\,, \tag{3.5}$$

where $\rho$ is density, $\boldsymbol{U}$ is velocity, $p_{\mathrm{rgh}}$ is dynamic pressure, $p$ is total pressure, $\boldsymbol{g}$ is gravitational acceleration, $h$ is specific sensible enthalpy, $K$ is specific kinetic energy, and $Y_i$ is the mass fraction of the $i^{th}$ specie. Unity Lewis and Prandtl numbers are assumed and a one equation eddy-viscosity turbulence model is used to represent the turbulent contributions to the effective viscosity and

thermal diffusivity, denoted $\mu_{\text{eff}}$ and $\alpha_{\text{eff}}$, respectively. The heat transfer terms $Q_{\text{rxn}}$ and $Q_{\text{rad}}$ represent effects due to reactions and radiations, respectively, and $\omega_i$ is the reaction rate of the $i^{th}$ specie. The ideal gas law (relating $p$, $T$ and $\rho$) is used for closure to Equations 3.1-3.4.

Within the solid, one-dimensional conservation equations for mass, reacting species, and enthalpy are solved to model heat transfer and pyrolysis [64–66]. These equations are given as [37]

$$\frac{\partial \rho_{\text{s}}}{\partial t} = -\dot{R}_{\text{gas}}\,, \tag{3.6}$$

$$\frac{\partial(\rho_{\text{s}} h_{\text{s}})}{\partial t} - \frac{\partial}{\partial z}\left[\frac{\partial(\kappa_{\text{s}} T_{\text{s}})}{\partial z}\right] = S_{\text{rad}} + S_{\text{rxn}} + S_{\text{gas}} + S_{\text{flux}}\,, \tag{3.7}$$

$$\frac{\partial\left(\rho_{\text{s}} Y_{k,\text{s}}\right)}{\partial t} = \dot{R}_k\,, \tag{3.8}$$

where $\rho_{\text{s}}$ is the solid density, $\dot{R}_{\text{gas}}$ is pyrolysis gas production rate, $Y_{k,\text{s}}$ is the mass fraction of the $k^{\text{th}}$ solid chemical specie, $\dot{R}_k$ is the corresponding reaction rate, $h_{\text{s}}$ is the solid-phase specific enthalpy, and $\kappa_{\text{s}}$ is the thermal conductivity. Source terms are included in the solid-phase enthalpy equations to account for radiation ($S_{\text{rad}}$), reactions ($S_{\text{rxn}}$), gas production ($S_{\text{gas}}$), and gas motion within the solid ($S_{\text{flux}}$).

Gas-phase combustion is modeled using infinitely-fast chemistry. Prior work with fireDyM-Foam has shown that infinitely-fast chemistry can be used to accurately reproduce experimental measurements of diffusion flames in pool fires [36] and during solid phase pyrolysis [37], supporting the use of this computational simplification in the present study.

The solid- and gas-phase regions are coupled using mixed, mapped boundary conditions for temperature, fuel mass fraction, and velocity. Temperature and velocity boundary conditions follow those described by Vinayak [66]. Fuel mass fractions are modeled using a look-up table approach to assign temperature-dependent compositions to the gas-phase pyrolysis products, as described in the next section.

### 3.3.2 Pyrolysis kinetic model

From a physical standpoint, the pyrolysis process consists of thousands to millions of elementary reactions [17]. Reduced-order models are thus required to render the pyrolysis process

computationally tractable. Attempts to capture the complexity of the pyrolysis mechanism with significantly simpler kinetics have included single-component/single-step, single-component/multi-step, multi-component/single-step and multi-component/multi-step kinetics [18]. Ranzi *et al.* [34] published a gas-phase chemical mechanism that relied on species that are produced in their multi-component/multi-step pyrolysis kinetic model. These models have been updated over the years with the assistance of pyrolysis experiments, notably by Corbetta *et al.* [46], [45], and [26]. One common factor of these works is the lack of gaseous ignition or combustion modeling. The present study aims to combine the existing fireFoam (and by extension fireDyMFoam) framework for modeling solid-phase pyrolysis and gas-phase combustion with the multi-component/multi-step pyrolysis model published by Debiagi *et al.* [45].

For simplicity and computational speed, we predict the rate of formation of char and gas-phase pyrolysis products using a single-component, single-step approach with an irreversible Arrhenius reaction, as given by

$$\text{wood}^n \xrightarrow{k_{\text{pyro}}} \text{char} + \text{gas}\,,$$

with the pyrolysis reaction rate, $k_{\text{pyro}}$, given by

$$k_{\text{pyro}}(T) = \begin{cases} 0 & T < T_{\text{crit}} \\ AT^{\beta} \exp\left(-\frac{T_a}{T}\right) & T \geq T_{\text{crit}} \end{cases}. \tag{3.9}$$

Here, $n$ is the order of the reaction, $A$ is the pre-exponential factor, $\beta$ is the temperature dependent constant, $T$ is the local solid-phase temperature, $T_a$ is the activation temperature, where $T_a \equiv E_a/R_u$ (namely, the activation energy divided by the universal gas constant). Temperature-varying specific heats are applied for wood and char in the form of a power-law fit given by

$$c(T) = c_0 \left(\frac{T}{T_{\text{ref}}}\right)^{n_0}, \tag{3.10}$$

where $c_0$, $n_0$ and $T_{\text{ref}}$ are reference values of the specific heat, exponent, and temperature that must be defined for each fuel sample.

As defined in Equation (3.9), the solid-phase reaction only proceeds after the critical temperature $T_{\text{crit}}$ is reached. Once produced, the pyrolysis gases are immediately transferred out of the solid; this approximation was recently validated by Agarwal *et al.* [67]. In the present study, we assign a temperature-dependent composition of these gases using a custom boundary coupling approach to convert the generic "gas" produced by pyrolysis of the solid-phase to multi-species products predicted by Debiagi *et al.* [45]. This study uses multi-step, multi-species kinetics to convert the main constituents of wood (i.e., cellulose, hemicellulose, lignin and extractives) to combustible materials, intermediates, and char in a zero-dimensional process.

To incorporate this model within the OpenFOAM-7 pyrolysis framework, the equilibrium species mass fractions are tabulated as a function of temperature from 300 K to 1,500 K in 5 K increments. Calculations were performed zero-dimensionally (i.e., as functions of time only) using ordinary differential equation integration (ode23s) in MATLAB, and the composition corresponding to each temperature was determined from the steady-state, or equilibrium, mass fractions. These are applied as look-up table functions at the solid-gas boundary in a custom version of the `totalFlowRateAdvectiveDiffusive` boundary condition. Here, the average temperature across the solid-gas interface is used to evaluate the pyrolysate composition by relative mass fractions of species entering the gaseous domain. Examples of these boundary conditions are included in the sample case found in the public github repository where fireDyMFoam can also be found (`github.com/clapointe2011/public`). While these new boundary conditions rely on the average surface temperature of the solid, they could also be extended to a cell-by-cell basis depending on the cell-valued temperature.

### 3.3.3 Numerical approach

In the gas domain, first-order temporal integration and second-order spatial discretization are used. Total variation diminishing variants of the central differencing scheme are used for scalar divergence terms, stabilized central differencing is used for velocity divergence, and enthalpy gradients are limited to bound temperature. The solid region is numerically configured following

cases provided with OpenFOAM [35], resulting in first-order in time and second-order in space accuracy. Maximum advective Courant and solid diffusion numbers of 0.4 and 1, respectively, are used to set a global time step. Time integration is performed using the pressure-implicit with splitting of operators (PISO) algorithm, and a fixed number of 3 PISO loops are used. We use a finite-volume implementation of the discrete ordinate method to model radiative heat transfer, with the grey mean absorption emission radiation model, prescribed coefficients based on fireFoam tutorials, and 100 discrete angles.

Load-balanced AMR is used in the gas-phase region, where refinement is based on multiple fields simultaneously. Further details on the specific configuration of the AMR used here is provided in the next section, and additional description of the development, verification, and validation of AMR in the fireDyMFoam solver is provided in References [36, 37]. A flowchart of the current implementation of fireDyMFoam is shown in Figure 3.2.

## 3.4 Computational Simulations

In the following, we apply the fireDyMFoam solver described in Section 3.3 to simulate the experiments outlined in Section 3.2. We first outline the physical configuration of the simulations, followed by a description of the AMR approach used here, and then end with a comparison of the simulation and experimental results.

### 3.4.1 Physical configuration

The simulations use a 1 $m^3$ total domain size and a $[0.12 \times 0.04 \times 0.02]$ m Douglas fir solid fuel sample to represent the experiments. Although this simulation configuration, shown in Figure 3.3, is an idealization of the experimental configuration provided schematically in Figure 3.1, the available experimental measurements were all taken at or near the surface of the Douglas fir sample, away from the cone-calorimeter, structural supports, and other diagnostic equipment. Thus, the influence of the surroundings is minimal and it is not necessary to model the full experimental geometry to obtain good agreement with the measurements, as will be shown in Section 3.4.4.

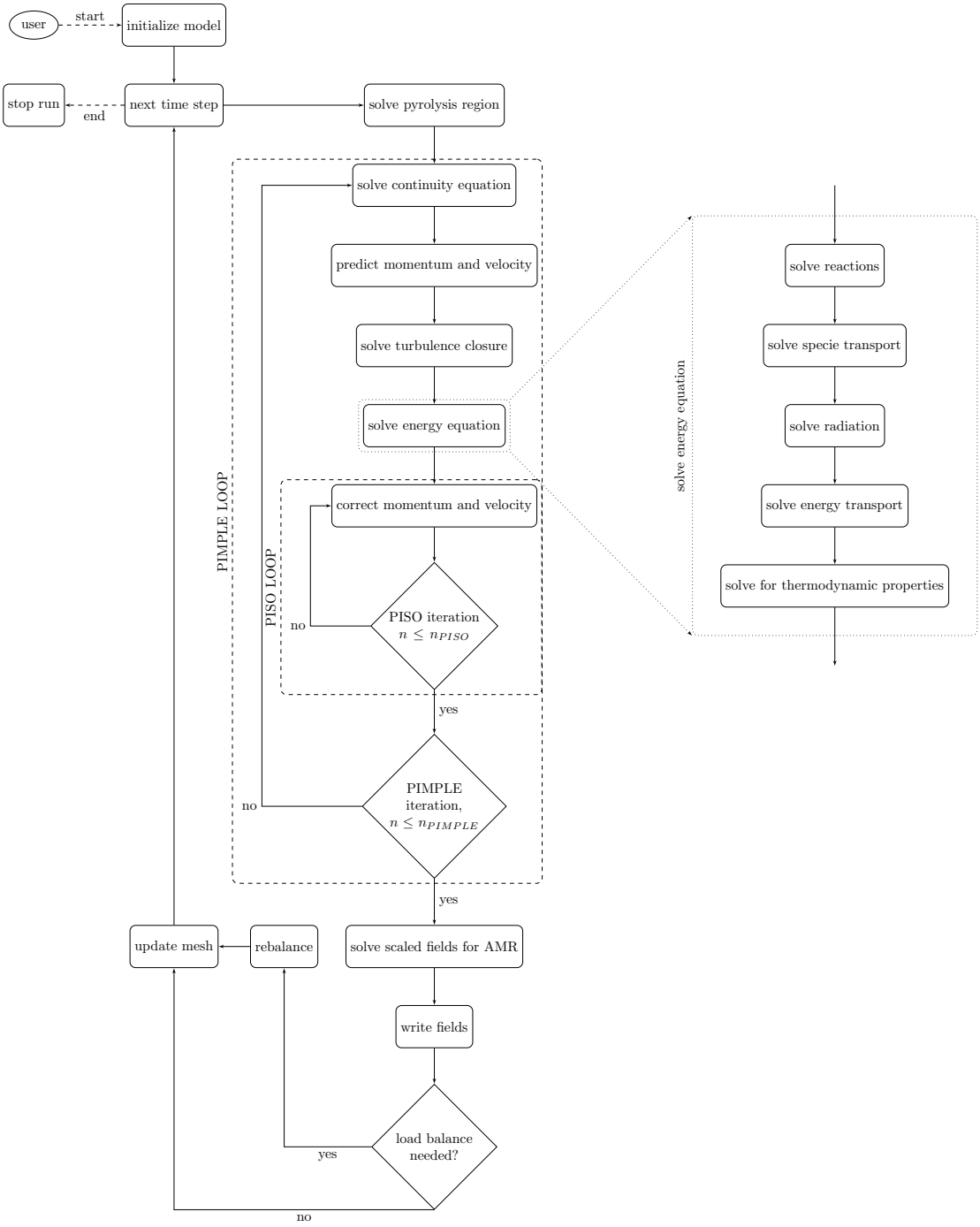


Figure 3.2: General flow for the fireDyMFoam solver in OpenFOAM.

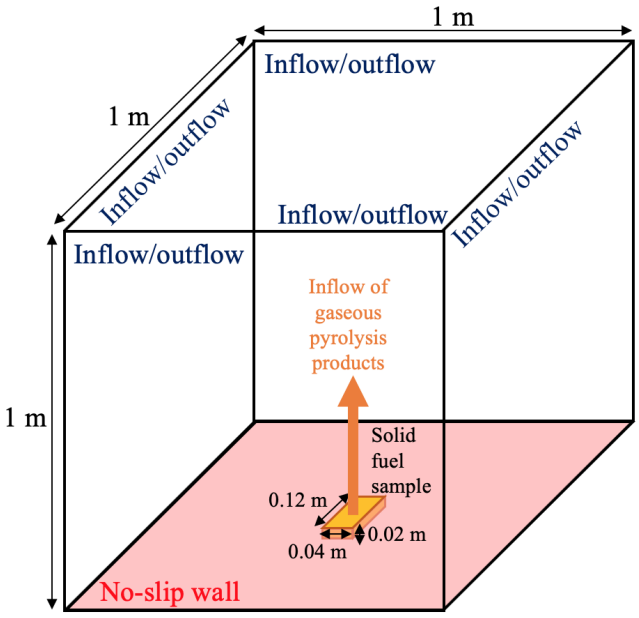


Figure 3.3: Schematic of the computational domain indicating boundary conditions, dimensions, and the location of the solid fuel sample on the bottom boundary.

The gaseous domain is initially filled with a quiescent mixture of air and water vapor to match the ambient experimental humidity. All sides of the gaseous region are open and allow for entrainment, with the exception of the base, which is modeled as a mild air co-flow (5 mm/s), and the solid-gas interface. This coupling takes the form of boundary conditions for velocity (to conserve the mass flux of gas from the solid region to pyrolysate species in the gaseous region), temperature (to conserve energy across the gas-solid interface), and species (converting generic "gas" product in the solid region to known species in the gaseous region). At 89 s, combustion is initiated via infinitely-fast chemistry, matching the time when the experiment was ignited via a spark.

In the solid region, physical properties are set to match those of the Douglas fir sample used in the experiment. Properties of the wood are assumed to be homogeneous, with wood density $\rho_{\text{wood}} = 524$ kg/m$^3$ based on experimental measurements, char density $\rho_{\text{char}} = 73$ kg/m$^3$, thermal conductivities $\kappa_{\text{wood}} = 0.11$ W/(m·K) and $\kappa_{\text{char}} = 0.065$ W/(m·K), emissivities of 0.759 and 0.957 for raw and charred wood, respectively. where $c_0$, $n_0$ and $T_{\text{ref}}$ are given in Table 3.1, and the specific

Table 3.1: Constants pertaining to the specific heat of wood and char as a function of temperature.

| Constant | Wood | Char |
|---|---|---|
| $c_0$ ($\mathrm{J{\cdot}kg^{-1}{\cdot}K^{-1}}$) | 1,003.4 | 1,219 |
| $n_0$ | 0.9578 | 0 |
| $T_{\mathrm{ref}}$ (K) | 273 | 273 |

Table 3.2: Constants pertaining to the solid-phase reaction and associated reaction rate.

| Constant | Value |
|---|---|
| $n$ | 4.86 |
| $A$ | $4 \times 10^8$ $\mathrm{s^{-1}(m^3 \cdot mol^{-1})^n}$ |
| $\beta$ | 0 |
| $T_a$ | 14,400 K |
| $T_{\mathrm{crit}}$ | 300 K |

heat of formation is set as $h_{s,\mathrm{wood}} = -4 \times 10^4$ kJ/kg [68, 69]. To model the radiative heat source used in the experiment, a heat flux of 21.9 $\mathrm{kW/m^2}$ is applied uniformly to the interface following the implementation in Vinayak [66]. The variable specific heat of Douglas fir wood and char are prescribed by parameters in Table 3.1. The pyrolysis reaction parameters are those in Table 3.2.

### 3.4.2 Pyrolysate Composition Specification

Initial mole fractions of cellulose, hemicellulose, `LIG-C`, `LIG-H`, `LIG-O`, `TANN`, and `TGL` for Douglas fir from References [45, 47, 48]; Table 2.1 lists these in terms of weight percentages. Chapter 2 showed the experimental surface temperature measurements of [38] to calculate the pyrolysate composition and compare to measured water mole fraction [42].

The composition of the gas-phase pyrolysis products corresponding to the Douglas fir sample are obtained by running out isothermal pyrolysis to steady state at various temperatures, as described in Sec. 3.3.2. The resulting concentrations of the eighteen pyrolysate species are shown as functions of temperature in Figure 3.4, and are constrained such that the sum over all species mass fractions is unity.

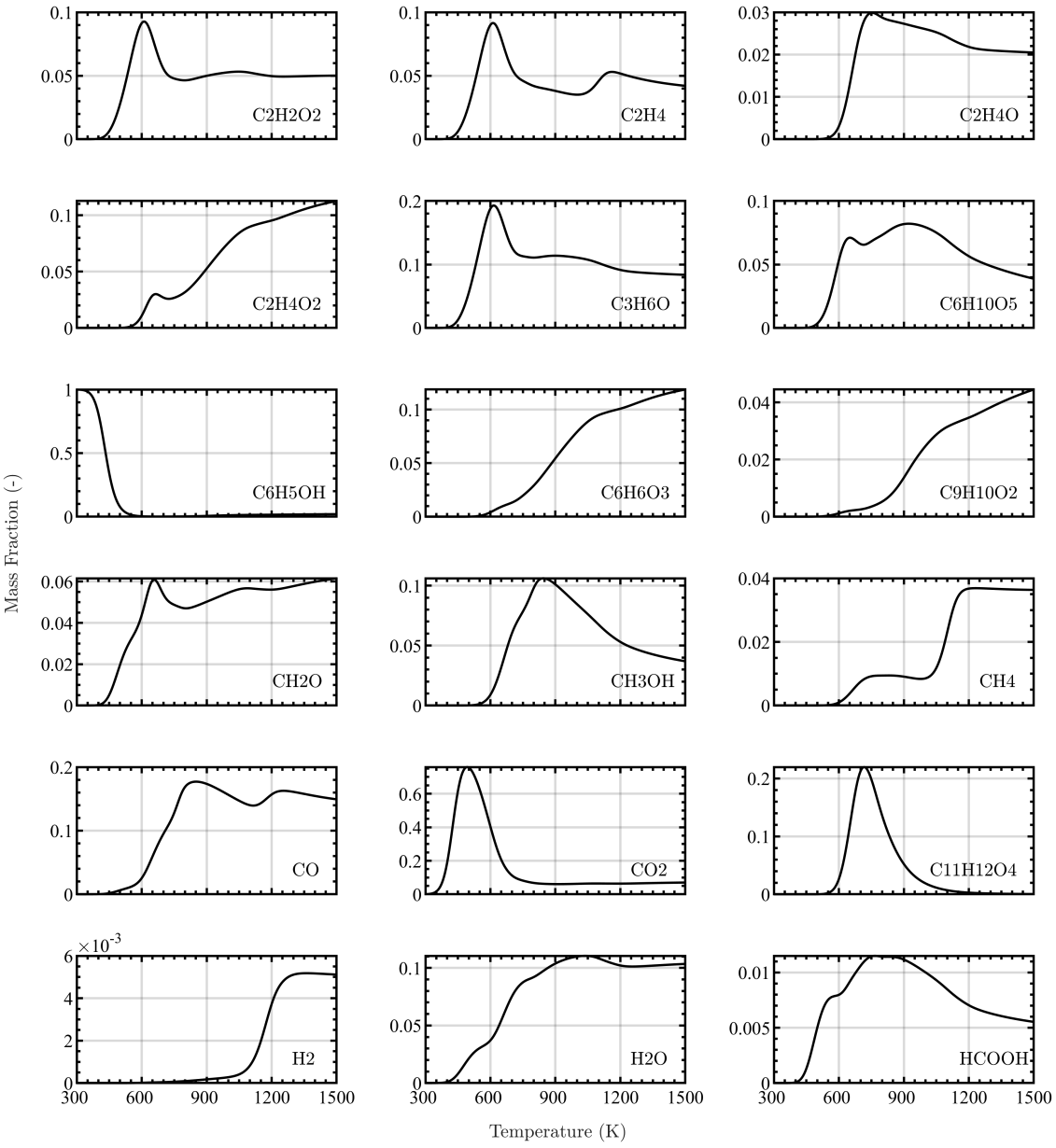


Figure 3.4: Equilibrium concentrations of 18 pyrolysate species as a function of temperature obtained from zero-dimensional integration of the multi-step pyrolysis kinetic model outlined by Debiagi *et al.*

### 3.4.3 AMR configuration

The computational domain is discretized at the coarsest level with a 4-cm uniform mesh. The cells within a $[0.20 \times 0.25 \times 0.10]$ m region centered on the bottom boundary are refined by three levels (i.e., eight times finer in each coordinate direction), corresponding to the region of interest.

The solid-gas interface containing cells within a $[0.12 \times 0.04]$ m rectangle, centered at the bottom of the domain, are refined with an additional level of AMR and are extruded downwards by 0.02 m to create the computational mesh for the solid. The resulting gas region mesh is composed of roughly 40,000 cells. The solid-phase domain has 192 one-dimensional (vertically oriented) regions, each with 45 cells, for 8,640 total cells.

Within the gaseous region, three levels of AMR are used to attain 5 mm resolution in areas of active mixing of air and pyrolysate. Refinement is performed in areas of high methane concentration and high gradients of methane concentration. Heat release is also included in the AMR criteria for refining areas of active combustion. Each parameter is scaled between values of zero and one; using methane concentration as an example, the normalized concentration is given by

$$[\widehat{\mathrm{CH_4}}] = \frac{[\mathrm{CH_4}] - \min([\mathrm{CH_4}])}{\max([\mathrm{CH_4}]) - \min([\mathrm{CH_4}])}\,, \tag{3.11}$$

where $[\widehat{\mathrm{CH_4}}]$ is the normalized methane concentration, and the absolute methane concentration is $[\mathrm{CH_4}]$. The criteria for refinement is based on the top 97.5% of normalized methane concentration, the top 99% of normalized methane concentration gradient, and the top 99.9% of normalized heat release.

An example AMR mesh at one time step, including the corresponding temperature field, is shown in Figure 3.5. Although the mesh does not change substantially during the later stages of the simulation, the AMR effectively provides a minimal mesh required to maintain the target resolution, resulting in an efficient numerical approach that does not require *a priori* knowledge of the flow. The majority of the simulation is run with roughly 65,000 cells. Comparable results were achieved with static mesh refinement (SMR) with nearly 385,000 cells.

### 3.4.4 Results

Because data collected from the frequency combs is line-of-sight averaged, simulated values for gas-phase temperature and species must be similarly processed. Values are linearly interpolated onto horizontal profiles across the center of the block at 2, 4, and 6 mm above the surface due to

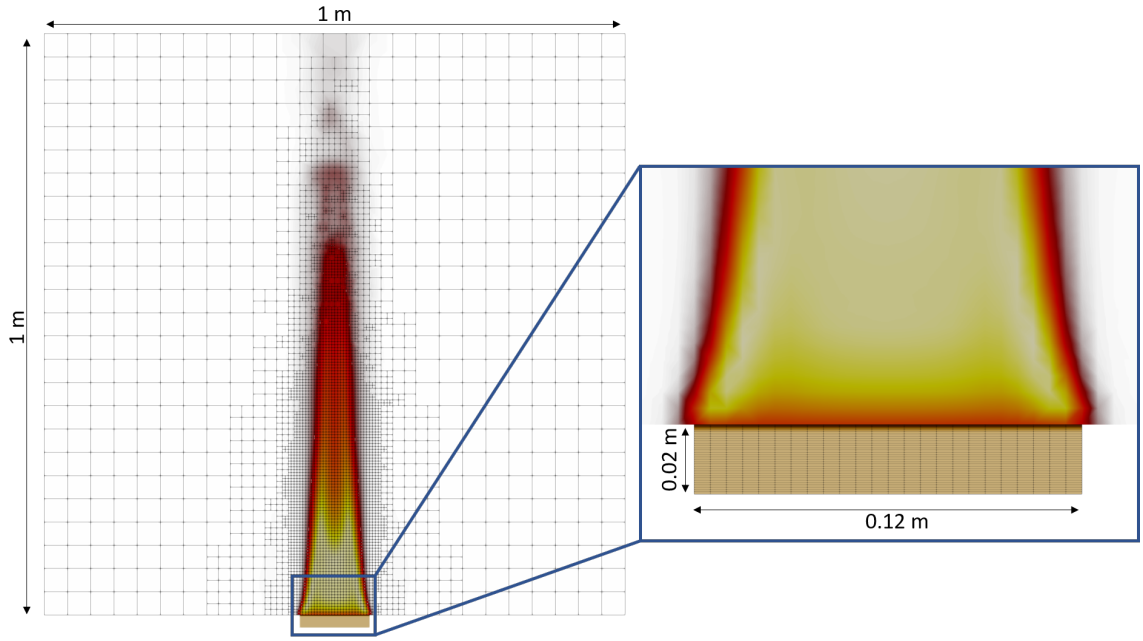


Figure 3.5: Gas- and solid-phase meshes, showing the temperature field from low (red, 750 K) to high (white, 1,650 K) and the char in the solid (inset) from low (tan, 0) to high (brown, 0.25) for the case of infinitely-fast chemistry with three levels of AMR in the gas-phase.

uncertainty in laser location attributable to swelling of the wood surface and beam steering (due to changes in the index of refraction) during the course of the experiment. Profile averages are then compared to experimental data.

Good agreement is observed between experimental and computational results for the solid surface temperature, as shown in Figure 3.6 for the simulated cases. The experimental surface temperatures were determined from the infrared camera using a constant surface emissivity, a time-varying mixture-dependent (wood and char) value is used computationally. The experimental mean was calculated from the beginning of each run until one experiment ignited, after that a dotted line is used to indicate an extrapolated experimental mean. Post-ignition surface temperature measurements are not shown for the experiment as the flame interferes with the measurement accuracy. Future experiments will utilize embedded thermocouples to capture the surface temperature post-ignition at near-surface locations and subsequent depths to further verify the solid model.

Figure 3.7 indicates that the simulated cumulative mass loss is accurate in capturing the mass

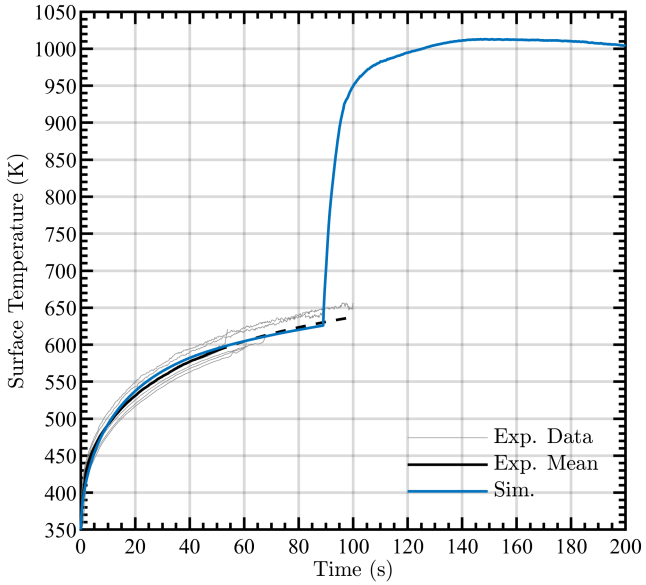


Figure 3.6: Simulated surface temperature during pyrolysis (blue line) compared to average experimental FLIR measurements prior to ignition (black solid and dotted lines, dotted lines are extrapolated from experimental mean once some experiments had ignited). Observed surface temperatures for each experiment are shown by gray lines.

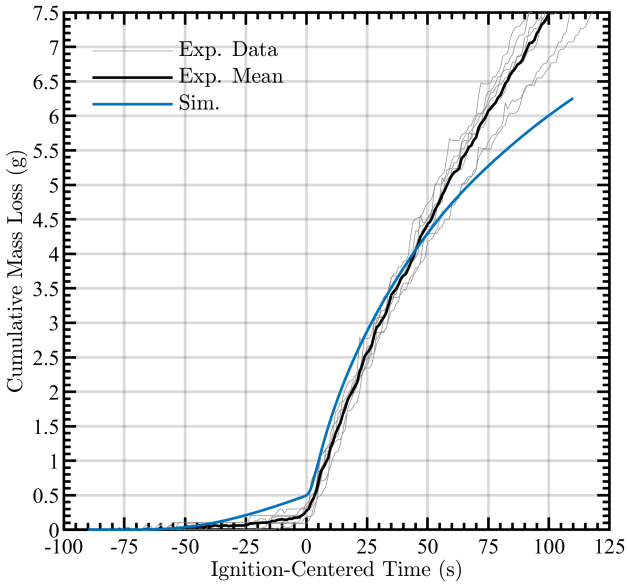


Figure 3.7: Simulated cumulative mass loss during pyrolysis and post-ignition (blue line) compared to the mean experimental measurements (black line). Observed mass loss time-series for each experiment are shown by gray lines.

loss during most of the combustion process. The experimental and simulated data are centered with respect to one another by setting the time of ignition to $t = 0$ s. Potential sources of discrepancy are

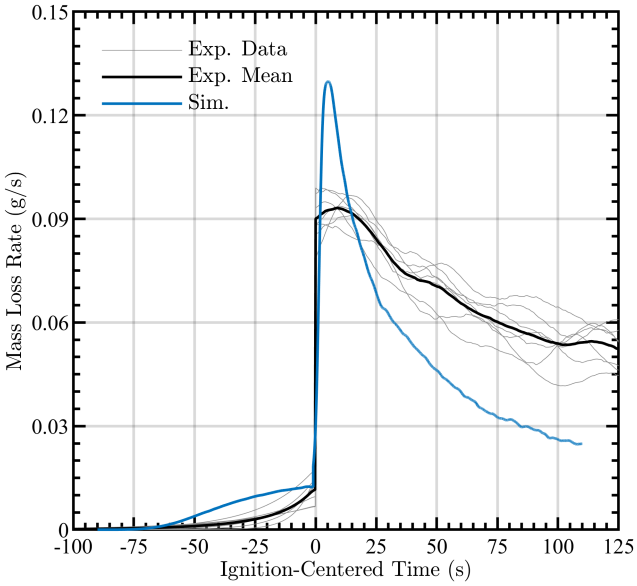


Figure 3.8: Simulated cumulative mass loss rate during pyrolysis and post-ignition (blue line) compared to the mean experimental measurements (black line). Observed mass loss rate profiles for each experiment are shown by gray lines.

that char oxidation and the physics of smoldering combustion are not explicitly solved in this model. Furthermore, the one-dimensional nature of the solid region inhibits heat transfer transversely and thus diminishes the mass loss at later times where high surface temperatures are prevalent. Of particular interest, even in the absence of finite-rate chemistry in the gas-phase combustion, it is possible to obtain agreement with the solid-surface temperature and cumulative mass loss with the time-resolved experiments. The mass loss rates from the simulations and experiments are shown in Figure 3.8, revealing reasonable agreement during the pyrolysis phase and qualitative agreement of the mass loss trends post-ignition. These data are also ignition-centered in time.

The simulated time-series of gas-phase temperature is shown in Figure 3.9. Included in the figure are "clouds" of simulated temperatures at the nominal height of 4 mm $\pm$ 2 mm to capture uncertainty in the measurement height. Two factors cause the height uncertainty: as pyrolysis occurs, it is expected that the wood sample surface would swell and deform in-homogeneously and laser beam steering due to the index of refraction changing in the gas above the sample. The gray lines in Figure 3.9 show results from seven independent experiments of the same configuration. These

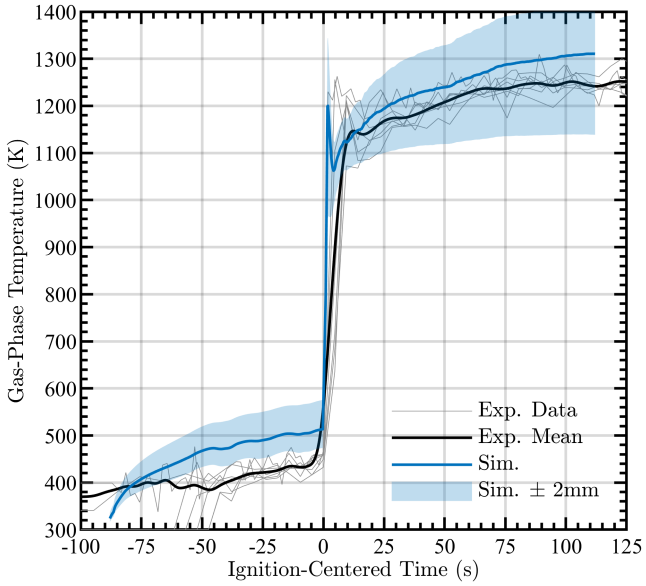


Figure 3.9: Simulated gas-phase temperature during pyrolysis and combustion (blue line) compared to experimental measurements nominally taken at 4 mm (black line). Clouds surrounding data provide measurements at ±2 mm from nominal measurement height. Observed gas-phase temperature measurements for each experiment are shown as gray lines.

results are centered at the time of ignition, enabling easier identification of temporal variations pre- and post-ignition. Simulations and averaging were carried out with the average ignition time of 89 s. Figure 3.9 shows that the simulation produces good agreement of gas-phase temperature after ignition although the gas-phase temperature is over-predicted during pyrolysis. This indicates that more sophisticated modeling of the solid phase may be necessary, which is an important direction for future research.

The water vapor mole fraction, normalized by ignition time, is shown in Figure 3.10 along with "clouds" of simulated temperatures at the nominal height of 4 mm ± 2 mm to capture uncertainty in the measurement height. A deficit of water vapor during pyrolysis and the deficit persists after ignition. This discrepancy points to the need for additional improvements to the pyrolysis boundary conditions post-ignition and to the composition of the pyrolysate. However, given the simplicity (i.e., infinitely-fast chemistry and use of only methane as the pyrolysate) of the computational model used here, the present results are promising for future simulations.

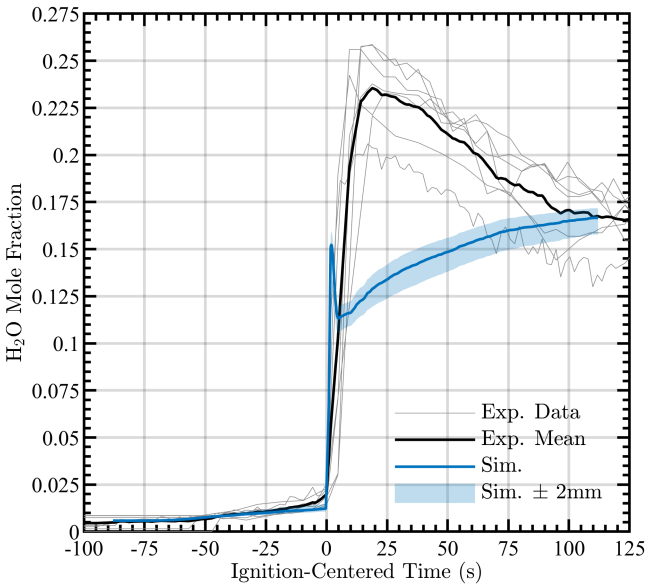


Figure 3.10: Simulated $H_2O$ mole fraction during pyrolysis and combustion (blue line) compared to experimental measurements nominally taken at 4 mm (black line). Clouds surrounding data provide measurements at ±2 mm from nominal measurement height. Observed gas-phase water mole fraction measurements for each experiment are shown by gray lines.

## 3.5 Conclusions

It has been shown that physics-based simulations in OpenFOAM can be performed to obtain agreement with experimental measurements of Douglas fir pyrolysis and combustion. These simulations leveraged AMR to achieve high computational efficiency for a resolution sufficient to model pyrolysis and combustion with infinite-rate chemistry. In particular, good agreement is shown with experimental time-series of gas and surface temperatures, and cumulative mass loss. The deficit in water vapor mole fraction in the gas-phase requires additional improvements to the custom boundary conditions to allow for additional pyrolysate fuel.

Future work will focus on extensions to include additional pyrolysate species, finite-rate chemistry, char oxidation, and smoldering combustion. With more pyrolysis and combustion relevant species, comparisons to the mid-infrared frequency comb measurements of [44] will be possible with the inclusion of the reduced biomass combustion model published by Glusman *et al.*[42]. Moreover, coupling these computationally efficient simulations with parameter estimation methods such as

approximate Bayesian computation [70], could allow for automated estimation of simulation parameters (i.e., heat of reaction and Arrhenius reaction coefficients) as well as initial conditions (i.e., temperature and water mole fraction) and/or boundary conditions (i.e., unmeasured parameters during experimental procedure).

*This chapter is based on a publication titled "Validation of Computationally Efficient Simulations of Douglas Fir Pyrolysis and Combustion Using Time-Resolved Frequency Comb Laser Measurements" that was published in Frontiers in Forests and Global Change: Fire and Forests* [43].

# Chapter 4

# The Effects of Reduced Chemical Models on Flow Characteristics and Species in a Buoyant Reacting Plume

*"Entities should not be multiplied beyond necessity."*

— William of Ockham

## 4.1 Introduction

Buoyancy, convection and ignition conditions are topics of interest when discussing wildfire propagation and modeling [71]. Specifically, Finney *et al.* show that wildfire flame fronts show a puffing instability, a similar behavior that was observed and quantified in reacting (pool fires) and non-reacting buoyant plumes [71]. Buoyant plumes will be the main focus of this work in which the puffing instability is one that leads to a regular, oscillatory motion of vortices being periodically shed. This phenomena, quantified by the puffing frequency, has been studied extensively for non-reacting plumes using various buoyant, non-reactive substances [39, 40, 72–74] and reacting plumes with various fuel sources, in various states of matter [75–78]. The work of Cetegen and Ahmed specifically concludes that the puffing frequency of a non-reacting plume scales as $L^{-3/5}$, while the reacting plume scales as $1.5L^{-1/2}$ [75] where $L$ is a length scale characteristic of the plume source (e.g., the diameter for a circular source). A similar correlation between the Strouhal number ($St$), non-dimensional frequency, and Froude number ($Fr$), the non-dimensional relation between inertial and buoyancy forces, was proposed by Finney *et al.*, specifically that $St = 1.6Fr^{-2/5}$ where the

non-dimensional numbers are defined as

$$St = \frac{fL}{U}\,, \tag{4.1}$$

$$Fr = \frac{U^2}{gL}\,. \tag{4.2}$$

In these two non-dimensional numbers, each variable represents a characteristic of the flow: $f$ is the frequency of oscillation, $U$ is a characteristic velocity, $L$ is the radius or diameter of the outlet and $g$ is the acceleration due to gravity. In addition to correlations of $St$ with respect to $Fr$, Cetegen and Kasper found later that $St$ was dependent on the Richardson number ($Ri$), defined as

$$Ri = \frac{(\rho_\infty - \rho)gL}{\rho_\infty U^2}\,, \tag{4.3}$$

where $\rho_\infty$ is the ambient density, and $\rho$ is the buoyant fluid's density [73]. This work noted a correlation of $St = 0.8Ri^{0.38}$ for axisymmetric plumes, which was later a correlation specifically for planar plumes was suggested as $St = 0.55Ri^{0.45}$, using diameter/width as the characteristic length [74]. The difference was attributed to changes in the rate of mixing and local buoyancy flux when comparing axisymmetric and planar plumes [74].

Much of the reacting plume simulations in the literature utilize substantial simplifications to handle the chemistry. Maragkos and Merci [79] used infinitely-fast chemistry and a modified Eddy Dissipation Model [80] within the context of a large eddy simulation. Luo [81] performed direct numerical simulations of a simple generic one-step, irreversible reaction that was governed by an Arrhenius rate. Zhou *et al.* [82] utilized the Burke-Schumann formulation of infinitely-fast chemistry of a generic fuel, set to model methane, in a large eddy simulation with a constraint on the mixture fraction to be bounded in the range of [0,1].

This chapter will focus on describing the effects of using the chemical kinetic models that were introduced in Ch. 2 and understanding how the fidelity of the chemical reduction affects the major species and flow characteristics when applied to a simulation of a reacting buoyant plume. The infinitely-fast chemistry of a lumped fuel specie will also be demonstrated and compared.

## 4.2 Background on Complex Chemistry in CFD Simulations

The implementation of detailed kinetic models of large fuels into computational fluid dynamic frameworks has proven to be an incredibly difficult problem [83, 84]. Researchers have approached this challenge using several strategies, including simplified chemistry by global reaction models, infinitely-fast chemistry, and flamelet approaches [85]. These various methods lack the detail to resolve the smallest scales and thus lack the ability to predict all products of combustion [86, 87]. Therefore the application of reduced chemical models and numerical solution techniques of stiff, larger kinetic mechanisms have been used in combustion applications when additional products of combustion are of interest.

### 4.2.1 Reduced Chemical Models

The idea of methodically reducing chemical mechanisms is one that specifically aims to reduce the number of species and reactions, while continuing to contain information critical for the time integration in a reacting flow. Reducing the number of species decreases the amount of computational time required to solve transport equations for each of the active scalar quantities (e.g., mass or mole fraction). Reducing the number of reactions decreases the amount of time required to calculate the source/sink term that arises in the aforementioned transport equations. There are numerous methods to systematically reduce chemical mechanisms with differing levels of generalization, user-input and automation. One of the first concepts was to remove reactions that did not hit a specified heat production rate; if a specie was no longer in any reaction, it was removed [88]. A successful, albeit time-intensive, method was removal of reactions by trial-and-error [89]. In the same year, Turányi published a sensitivity analysis study utilizing the Jacobi method to allow for an understanding of how small changes of one specie connected to the change of "important" species [90]. Chapter 2 introduced and utilized MARS (which has been released using Cantera as pyMARS [91]) which was built upon the following contributions: the Directed Relation Graph (DRG) [92], the variant of DRG with error propagation (DRGEP) [93], as well as DRGEP with

sensitivity analysis (DRGEPSA) [94].

There have been various efforts in implementing reduced chemical kinetic models into CFD simulations with varying applications from internal combustion engines [95], to supercritical $CO_2$ combustors [96], to tropospheric chemistry [97], and to laminar and turbulent flames (premixed and non-premixed) [98, 99]. Recently an article by Zettervall *et al.* reviewed and evaluated various kinetic models for methane combustion. The authors utilize the computational time to complete 1D flame simulations as their metric for computational cost and focus on profiles of major (CO, $CO_2$, $H_2$, $H_2O$) and intermediate species ($CH_2O$, CH, OH) for their accuracy metric [100].

### 4.2.2 Numerical Techniques for Solving Finite Rate Chemistry

The process of mechanism reduction for combustion applications is typically done *a priori* in a fashion to achieve minimal changes to the ignition delay time while maintaining critical species [101]. However, there are some on-the-fly numerical methods to reduce the computational burden of complex chemistry. Pope developed *in situ* adaptive tabulated chemistry (ISAT) [102] which was a computational technique used for probability density function (PDF) methods for turbulent combustion on various kinetic models. Liang *et al.* developed dynamic adaptive chemistry (DAC) [103] which performed on-the-fly reduction of kinetic models using DRG and performed well on mechanisms on the order of 500 species. These two methods were combined and dubbed tabulated dynamic adaptive chemistry (TDAC) by Contino *et al.* which performed well in simulations of internal combustion engines, where local thermodynamics were not in equilibrium and often the mixture is inhomogeneous [104]. Contino *et al.* showed that the combination of these methods was successful for mechanisms on the order of 500 species in complex flow environments [104].

Recent OpenFOAM-based developments for high performance computing (HPC) applications include dynamic load balancing of the stiff chemical solver within OpenFOAM, called DLBFoam [105], which has future potential integration with fireFoam and it's variants. Within a year of release, DLBFoam received development work to include the pyJac [106] analytical Jacobian implementation which reduces the cost of evaluating the Jacobian by 3-7.5 times compared to the finite

difference approach (like the one native to OpenFOAM) [107]. Morev *et al.* also implemented functions found in the LAPACK package [108] for the seulex solver within the OpenFOAM framework. The simulations performed by Tekgül *et al.* and Morev *et al.* utilized chemical kinetic models with 54 species and 269 reactions and performed very well in reducing the computational time by factors of 10-12 when compared to the standard methods. It is of particular note that the dynamic load balancing speed-up would potentially be diminished if higher tolerances were used in the process [105].

## 4.3 Computational Solver

The numerical simulations are performed in OpenFOAM [35] using the fireFoam solver [59] for two-dimensional simulations. Initially developed for simulations of pool fires [59], fireFoam has been used to model industrial fire problems in a number of different contexts and configurations [60–64]. At this time, fireDyMFoam is not suitable for two-dimensional simulations due to implementation limits of AMR (cell splitting creates new cells in the third-dimension).

### 4.3.1 Governing equations

Within the gaseous domain, the compressible Navier-Stokes equations are solved along with conservation equations for mass, total enthalpy, and reacting species. These equations are given as [37]

$$\frac{\partial \rho}{\partial t} + \boldsymbol{\nabla} \cdot (\rho \boldsymbol{U}) = 0\,, \tag{4.4}$$

$$\frac{\partial (\rho \boldsymbol{U})}{\partial t} + \boldsymbol{\nabla} \cdot (\rho \boldsymbol{U}_i \boldsymbol{U}_j) = -\boldsymbol{\nabla} p_{\mathrm{rgh}} + \boldsymbol{\nabla} \cdot \tau_{ij} + \rho \boldsymbol{g}\,, \tag{4.5}$$

$$\frac{\partial \left[\rho (h + K)\right]}{\partial t} + \boldsymbol{\nabla} \cdot [\rho \boldsymbol{U} (h + K)] = \boldsymbol{\nabla} \cdot [\alpha_{\mathrm{eff}} \boldsymbol{\nabla} (\rho h)] + \frac{\partial p}{\partial t} + Q_{\mathrm{rxn}} + Q_{\mathrm{rad}}\,, \tag{4.6}$$

$$\frac{\partial (\rho Y_i)}{\partial t} + \boldsymbol{\nabla} \cdot (\rho \boldsymbol{U} Y_i) = \boldsymbol{\nabla} \cdot [\alpha_{\mathrm{eff}} \boldsymbol{\nabla} (\rho Y_i)] + \rho \omega_i\,, \tag{4.7}$$

$$\tau_{ij} = \boldsymbol{\nabla} \cdot \left[\mu (\boldsymbol{\nabla} \boldsymbol{U} + (\boldsymbol{\nabla} \boldsymbol{U})^T) - \lambda (\boldsymbol{\nabla} \cdot \boldsymbol{U}) \boldsymbol{I}\right]\,, \tag{4.8}$$

where $\rho$ is density, $\boldsymbol{U}$ is velocity, $p_{\mathrm{rgh}}$ is dynamic pressure, $p$ is total pressure, $\boldsymbol{g}$ is gravitational acceleration, $h$ is specific sensible enthalpy, $K$ is specific kinetic energy, and $Y_i$ is the mass fraction

of the $i^{th}$ specie. Unity Lewis and Prandtl numbers are assumed. The heat transfer terms $Q_{\text{rxn}}$ and $Q_{\text{rad}}$ represent effects due to reactions and radiations, respectively, and $\omega_i$ is the reaction rate of the $i^{th}$ specie. The ideal gas law (equation of state, relating pressure, temperature and density by $p = \rho RT$) is used for closure to Equations 4.4-4.7.

### 4.3.2 Numerical approach

First-order temporal integration and second-order spatial discretization are used. Total variation diminishing variants of the central differencing scheme are used for scalar divergence terms, stabilized central differencing is used for velocity divergence, and enthalpy gradients are limited to bound temperature. Maximum advective Courant number of 0.5 are used to set a global time step. Time integration is performed using the pressure-implicit with splitting of operators (PISO) algorithm, and a fixed number of 3 PISO loops are used. We use a finite-volume implementation of the discrete ordinate method to model radiative heat transfer, with the grey mean absorption emission radiation model, prescribed coefficients based on fireFoam tutorials, and 16 discrete angles.

For simulations with finite-rate chemistry, the *in situ* adaptive tabulated chemistry (ISAT) [102] method is used to tabulate previous, explicit, chemistry solves into a binary tree and then are used to approximate the chemical source terms, specifically $\omega_i$ in Equation 4.7, to the nearest composition according to a tolerance of 3e-6 [109]. The use of DLBFoam [105, 107] was tested without the use of ISAT (as they are not compatible together, as noted by Tekgül *et al.*) and the performance of ISAT was 2-3 times faster than DLBFoam for the given numerical tolerance on the chemistry solver (absolute tolerance of 1e-8, relative tolerance of 1e-2).

For simulations with infinitely-fast chemistry (IFC), also referred to as "mixed-is-burnt", any computational cell with a mixture of fuel and oxidizer will combust to completion. This simplification of complex combustion chemistry is widely used to model diffusion flames, where the mixing time scale is the dominant limiting step [59]. The heat release rate can be adjusted by being spread out over time, reducing the *infinitely-fast* nature to mimic the more realistic chemical time scale (in OpenFOAM, this is dictated by a parameter `C` in `combustionProperties` [35]).

## 4.4 Computational Simulations

For the buoyant reacting flow study, two-dimensional simulations using various reduced skeletal models with the fireFoam solver on a static mesh with nested refinement regions are described in detail. Specifically, the computational mesh, different skeletal models, development of a lumped fuel specie similar to WFDS [24, 25] and ignition sources will be focused on in subsequent subsections.

### 4.4.1 Physical configuration

The simulations use a domain length of $L = 0.96$ m for all cases. The two-dimensional case has a 0.12 cm wide uniform inlet centered on the base with a co-flow outside of the inlet. The simulation configuration of a three-dimensional case is shown in Figure 4.1, the two-dimensional case is a simplification of this domain, utilizing only one cell in the third dimension and not solving for fluxes in-and-out of the domain. For both cases the velocity of inflow and co-flow are 5 mm/s and 2.5 mm/s, respectively. The temperature of the inflow and co-flow are 600 K and 300 K, respectively. The boundary conditions of all sides and the top are solved as open boundaries that allow for inflow and outflow. The composition of the inflow is comprised of pyrolysis species predicted at 800 K based on process outlined in Chapter 3, in Figure 3.4. This composition represents a first-order approximation of the surface temperature at ignition ($\sim$600 K) and that of the surface temperature after ignition ($\sim$1,000 K).

### 4.4.2 Reduced Chemical Kinetic Models

The skeletal models outlined in Chapter 2 (i.e., Skeletal-A, Skeletal-B, and Skeletal-C) have been implemented in various simulations to compare how reducing the complexity, and therefore accuracy, of the chemical modeling effects various flow characteristics. In addition to these skeletal models, an additional reduced model was produced, referred to here as Skeletal-D, which contains 40 species and 88 reactions. The generation of this model was done in a similar fashion as to Skeletal-A, -B and -C, but with a significantly large tolerance for error (1000%) in order to get

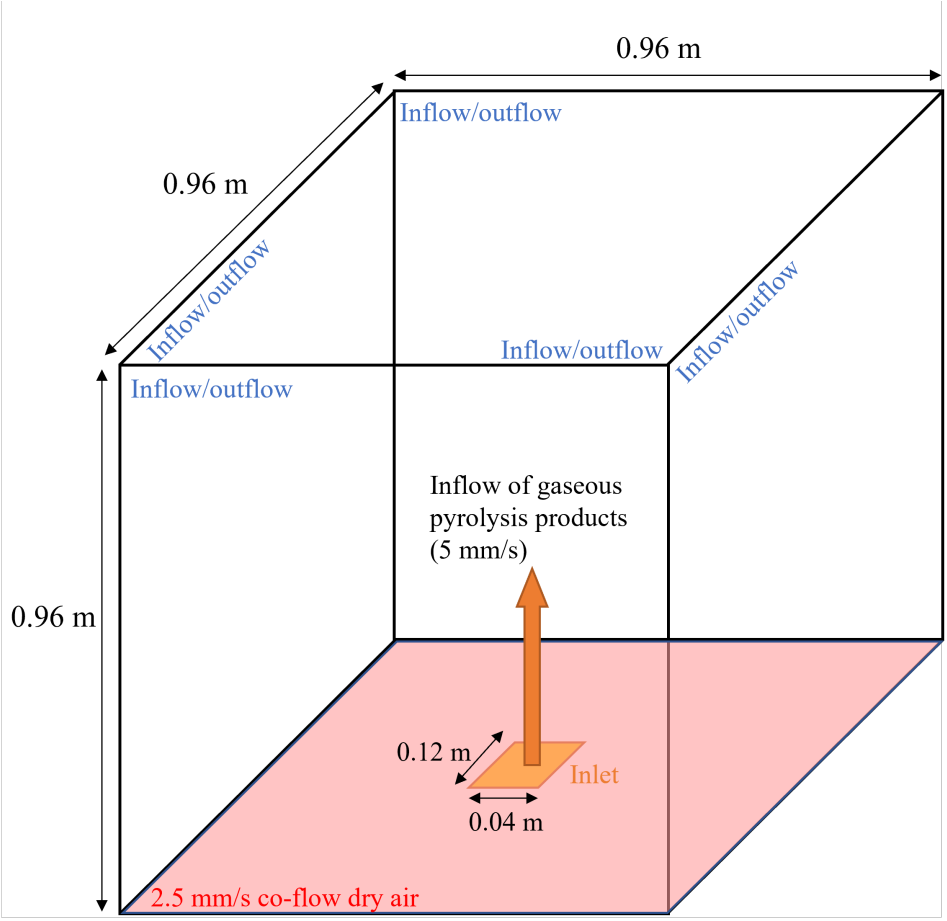


Figure 4.1: Schematic of the computational domain indicating boundary conditions, dimensions, and the location of the inlet and co-flow on the bottom boundary.

further reduction in size. The process for the calculation of Skeletal-D can be seen in Figure 4.2 in comparison to the other models. The final allowable error of Skeletal-D is predicted to be 840% based on maximum error of ignition delay time and peak temperature in a perfectly-stirred reactor. Information on the four skeletal models derived from the detailed mechanism of Ranzi *et al.* [34] can be found in Table 4.1. The input files for Skeletal-A, -B and -C are not included due to their length; however, they are freely available via this link to the Supplementary Materials of Glusman *et al.* [42], in Chemkin format as `skA.dat`, `skB.dat` and `skC.dat` along with the associated thermodynamics and transport files. The Skeletal-D kinetics in Cantera format (.cti) is included in Listing A.1 as it has not been published elsewhere, to date. The Cantera format is a compact form which includes

the thermodynamics and reaction information and is easily convertible to Chemkin or OpenFOAM formats.

The most notable differences of Skeletal-D with respect to the detailed mechanism are detailed in Figures 4.3-4.5. Specifically the ignition delay time in Figures 4.3 is lengthened by approximately an order of magnitude across temperatures expected during the ignition and combustion of the reactants for each of the equivalence ratios. The significant lowering of the peak temperature on the order of 200 K for $\phi = 0.5$ and $\phi = 1$ is observed in Figure 4.4, while $\phi = 1.5$ shows non-linear

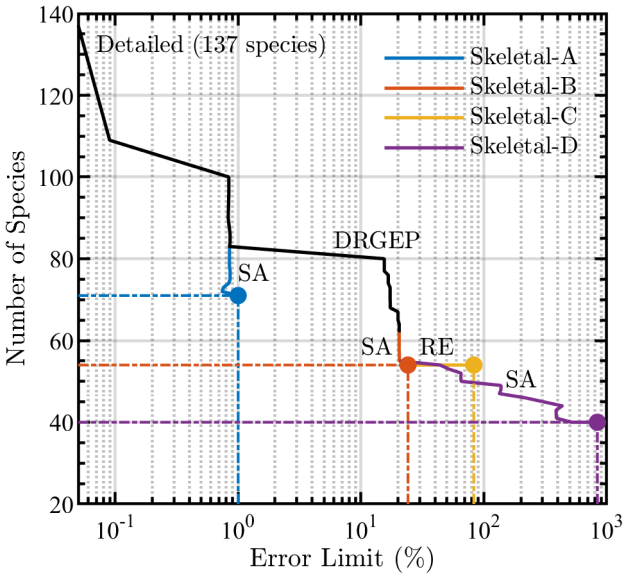


Figure 4.2: Number of species as a function of error limit during the reduction of the detailed model using the directed relation graph with error propagation (DRGEP), sensitivity analysis (SA) and reaction elimination (RE) methods. Dash-dot lines indicate the number of species for the given error limit in models Skeletal-A (blue lines), Skeletal-B (red lines), Skeletal-C (yellow lines), and Skeletal-D (purple lines).

Table 4.1: Detailed and skeletal model details, indicating the final number of species and reactions, as well as the error in the ignition delay time with respect to the detailed model.

| Model | # Species | # Reactions | Error % |
|---|---|---|---|
| Detailed | 137 | 4,533 | - |
| Skeletal-A | 71 | 1,179 | 0.81 |
| Skeletal-B | 54 | 637 | 24.1 |
| Skeletal-C | 54 | 204 | 82.9 |
| Skeletal-D | 40 | 88 | 840 |

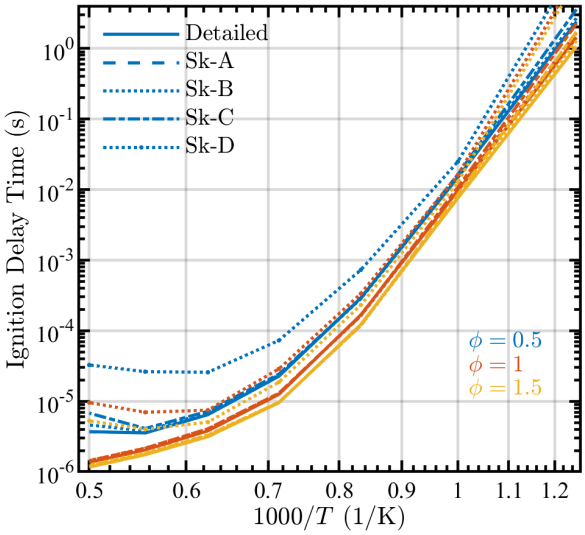


Figure 4.3: Ignition delay as a function of $1000/T$ in a PSR at equivalence ratios $\phi = [0.5, 1.0, 1.5]$ and $P = 1$ atm for the detailed (solid lines), Skeletal-A (dashed lines), Skeletal-B (dash-dot lines), Skeletal-C (dotted lines), Skeletal-D (dash-dot lines with circular markers) models.

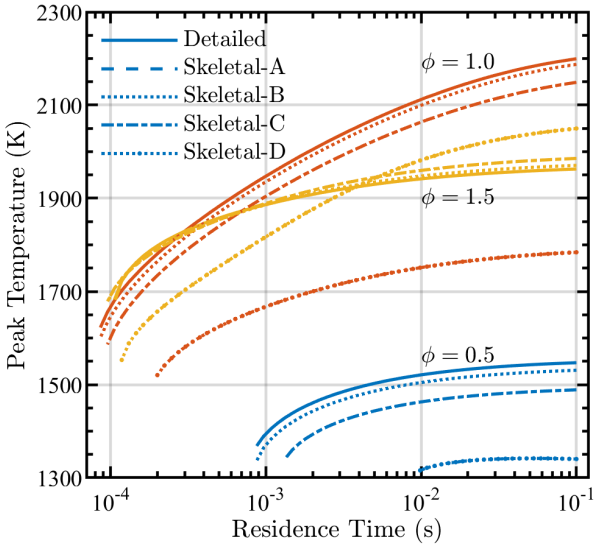


Figure 4.4: Peak temperature versus residence time in a PSR at equivalence ratios $\phi = [0.5, 1.0, 1.5]$ and $P = 1$ atm for detailed (solid lines), Skeletal-A (dashed lines), Skeletal-B (dash-dot lines), Skeletal-C (dotted lines), Skeletal-D (dash-dot lines with circular markers) models.

changes across residence times, but remains within 100 K.

The peak laminar flame speed of Skeletal-D is 78% of the detailed mechanism and occurs at much higher equivalence ratios. Figure 4.5 indicates that the predicted laminar flame speed of

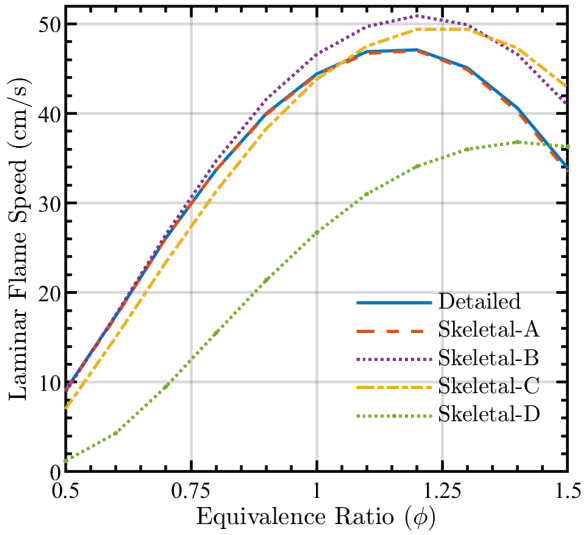


Figure 4.5: Laminar flame speed for a one-dimensional premixed flame as a function of equivalence ratio $\phi$ for detailed (solid lines), Skeletal-A (dashed lines), Skeletal-B (dash-dot lines), and Skeletal-C (dotted lines), Skeletal-D (dash-dot lines with circular markers) models. The reactants were at temperature 300 K and pressure 1 atm.

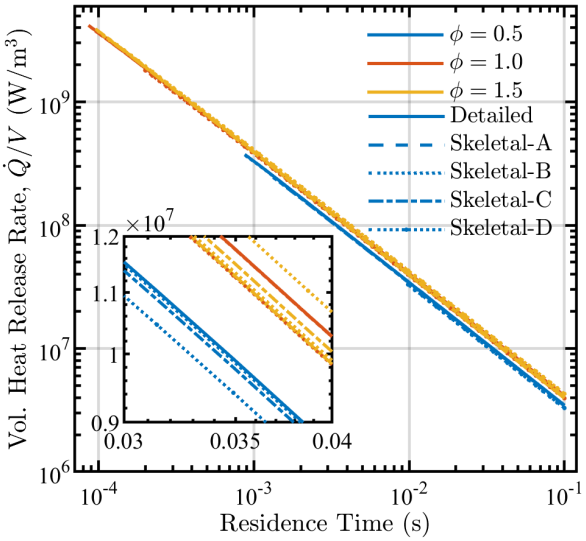


Figure 4.6: Volumetric heat release rate versus residence time in a PSR at equivalence ratios $\phi = [0.5, 1.0, 1.5]$ and $P = 1$ atm for detailed (solid lines), Skeletal-A (dashed lines), Skeletal-B (dash-dot lines), Skeletal-C (dotted lines), Skeletal-D (dash-dot lines with circular markers) models. The inset box shows detail of how close the data are.

Skeletal-D varies greatly when comparing to the predicted results of the detailed mechanism, as well as the skeletal models (Skeletal-A, -B and -C). The volumetric heat release rate in Figure 4.6

shows insignificant changes across the residence time for all values of equivalence ratio tested.

#### 4.4.2.1 Lumped Fuel Infinitely-Fast Chemistry Model

In addition, a composite, or lumped, fuel with physical and thermodynamic properties based on mixture-average properties of the inflow gases, sans $H_2O$ and $CO_2$, was produced. This process led to a lumped specie of the form $C_xH_yO_z$, where $x$ =1.961, $y$ =3.075 and $z$ =1.202, donned `FUEL1` in the corresponding reaction with air in Listing A.2. Infinitely-fast chemistry relies solely on the thermodynamic fits for individual species to calculate the heat addition due to reactions ($Q_{\text{rxn}}$) in Equation 4.6. In order to calculate the thermodynamics of the lumped specie, the mixture-average properties of the sixteen pyrolysate species were computed as reference quantities. The coefficients of the NASA polynomials [110] were computed for $a_0$ through $a_6$ to capture $c_p^0(T)$, $h^0(T)$ and $s^0(T)$ according to the following relations

$$c_p^0(T) = R_u \left(a_0 + a_1 T + a_2 T^2 + a_3 T^3 + a_4 T^4\right) , \tag{4.9}$$

$$h^0(T) = R_u T \left(a_0 + \frac{a_1}{2} T + \frac{a_2}{3} T^2 + \frac{a_3}{4} T^3 + \frac{a_4}{5} T^4 + \frac{a_5}{T}\right) , \tag{4.10}$$

$$s^0(T) = R_u \left(a_0 \ln T + a_1 T + \frac{a_2}{2} T^2 + \frac{a_3}{3} T^3 + \frac{a_4}{4} T^4 + a_6\right) , \tag{4.11}$$

where $R_u$ is the Universal Gas Constant, and all quantities are molar based. The results are shown in Figure 4.7. Very little visible changes between the mixture averaged reference properties and mixture averaged fit properties are perceptible, seen in Figure 4.7 panes (a)-(c). The relative error, defined as the magnitude of the difference between the reference and fit properties divided by the absolute value of the reference value quantifies there is very little error when considering the magnitude of the quantity of interest, seen in Figure 4.7 panes (d)-(f). As expected based on the work of Gordon, these parameters capture the thermodynamic state across a wide range of expected temperatures for the given fuel [110]. Temperatures are only shown from 600 to 3000 K as the fuel inlet temperature is 600 K and will react immediately with maximum temperature well below the 3000 K limit.

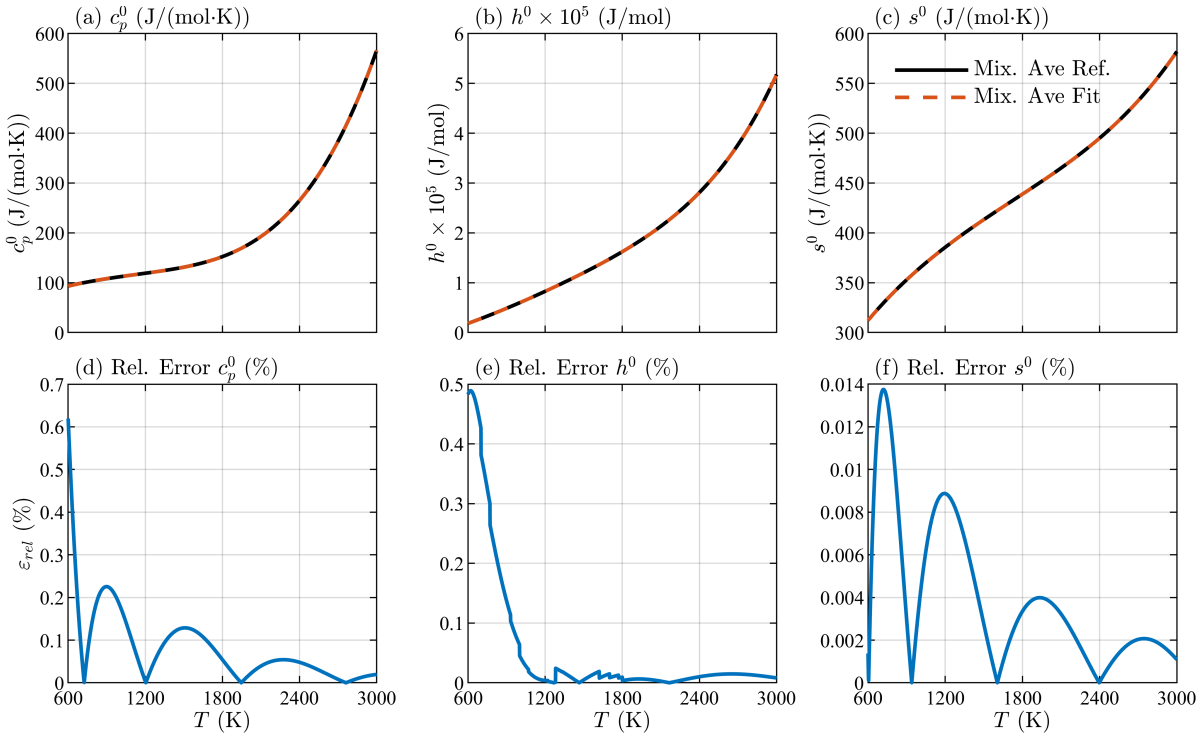


Figure 4.7: Comparison of referenced mixture averaged quantities, $c_p^0(T)$, $h^0(T)$ and $s^0(T)$, shown in a solid black line as a function of temperature and fitted quantities shown in dotted red line (a)-(c). The relative error, $\varepsilon_{\text{rel}}$, for each quantity is shown in a blue line (d)-(f).

### 4.4.3 Computational Mesh

In the two-dimensional case, the base grid is comprised of 15, 6.4 cm cells in each direction. The 2D mesh uses SMR in order to achieve 2 mm resolution for cells within a $[0.30 \times 0.55]$ m region centered on the domain. An example grid and rendering of temperature can be seen in Figure 4.8 and contains ∼44,000 cells. This computational grid allows for high resolution in the near-field of the buoyant plume and for ample downstream growth without the coarsening of cells interrupt the development.

### 4.4.4 Ignition Methods

Simulations were initially performed with 1,200 K inflow/co-flow temperatures to study auto-ignition of the pyrolysis products being flowed into the domain; while ignition occurred, this is unrealistic for future studies of spark-ignition. OpenFOAM offers two methods for modeling a spark:

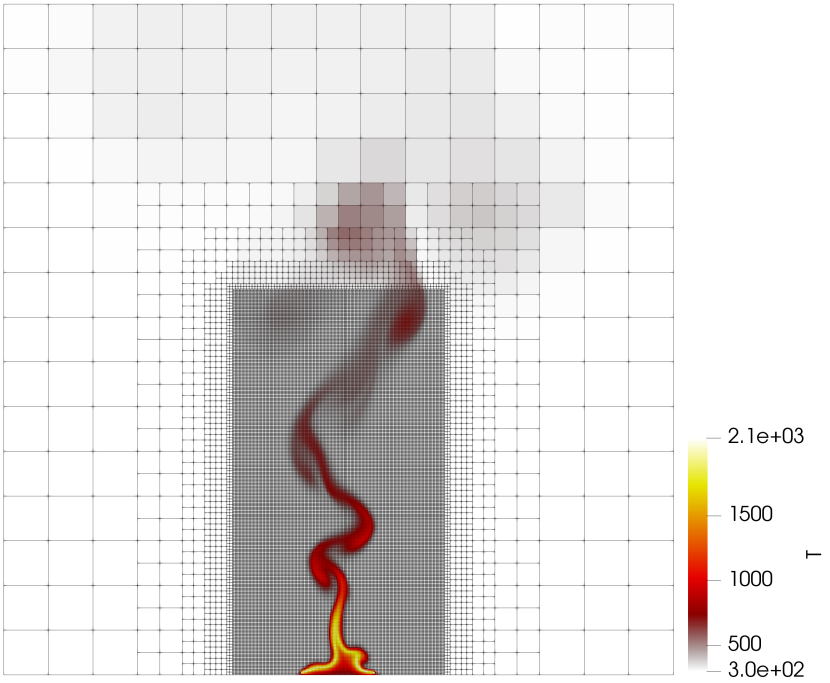


Figure 4.8: Two-dimensional mesh of combustion using Skeletal-D, showing the temperature field and SMR grid.

constraining specific cells to an increased temperature or turning specific cells into energy sources. Both methods have been shown to be effective in igniting mixtures, however, the temperature constraining method proved to be more easily implemented and more stable. Therefore, an array of cells were selected that would be held to an elevated temperature for a short period of time. Typical spark gaps last 10 to 100 ns and are 10 to 100 $\mu$m in size, reaching upwards of 50,000 K and 10 MPa [111]. In the 2D case, 55 cells were selected with a total area of $2.2e-4$ m$^2$, this process is visualized in Figure 4.9 for Skeletal-D. Similar time-series' are available for Skeletal-A, -B and -C in Figures B.1, B.2 and B.3, respectively, in Appendix B. The collection of cells are held to 1,800 K for 0.05 s beginning at $t = 5$ s illustrated in Figure 4.9(b)-(g). These conditions are only approximations of the conditions that exist in a spark gap.

Select frames (at $t = 5.06$ s and 5.14 s) are compared in Figure 4.10 to show qualitative agreement between the various reduced-order models moments after the ignition source is turned off. The flame height decreasing from left to right (in the direction of more reduction) can be

attributed to the increased error in ignition delay time between the various models. Zettervall *et al.* noted that models that had more reduction for methane combustion often would lead to longer ignition delay times predicted for a given temperature and equivalence ratio [100]; this is consistent with the results of ignition delay times for Skeletal-A, -B and -C in Figure 2.3 across all temperatures and selected equivalence ratios.

No specific ignition methods are required for the case of infinitely-fast chemistry of the lumped specie, $C_xH_yO_z$.

## 4.5 Results and Discussion

Each simulation runs for 30 s total, with 5 s of spin-up, 0.05 s of forced ignition (the infinitely-fast case did not require any ignition). The data collected, analyzed and presented in this section were taken from 7.5 s until 30 s for all cases. Time-averaged quantities will be denoted with an over-bar, i.e. $\overline{(\cdot)}$. All simulations presented here were performed on 2 processors on identical computational grids. Various metrics have been computed in Table 4.2 which indicate the time savings of the reduced chemical models, for a fixed number of processors and the fixed computational grid described in Section 4.4.3. Additionally, the total benefit of utilizing ISAT has been quantified based on the average time-step and average time per iteration to compute the average time for one second of simulated data for Skeletal-A and Skeletal-D in Table 4.3. The average time step of the reduced models with ISAT range between 25.8 and 26.5 ms, while simulations without tabulated chemistry require time steps between 17.6 and 18.2 ms; this changes the number of iterations required to reach a specific time, and metrics for average computational time per iteration and average computational time per one second of simulated data are provided. The usage of ISAT provides a factor of 2.63 to 3.96 speed-up over the various models, with more cost-savings for the more complex chemistry. When utilizing tabulated chemistry and comparing the three most reduced kinetics with respect to Skeletal-A, there is a 1.88 to 5.13 speed-up factor, with more cost-savings for the less complex chemistry. Infinitely-fast chemistry (IFC) provides a significant speed-up factor of 85.5 to 111.5 times due to the limited number of specie transport equations

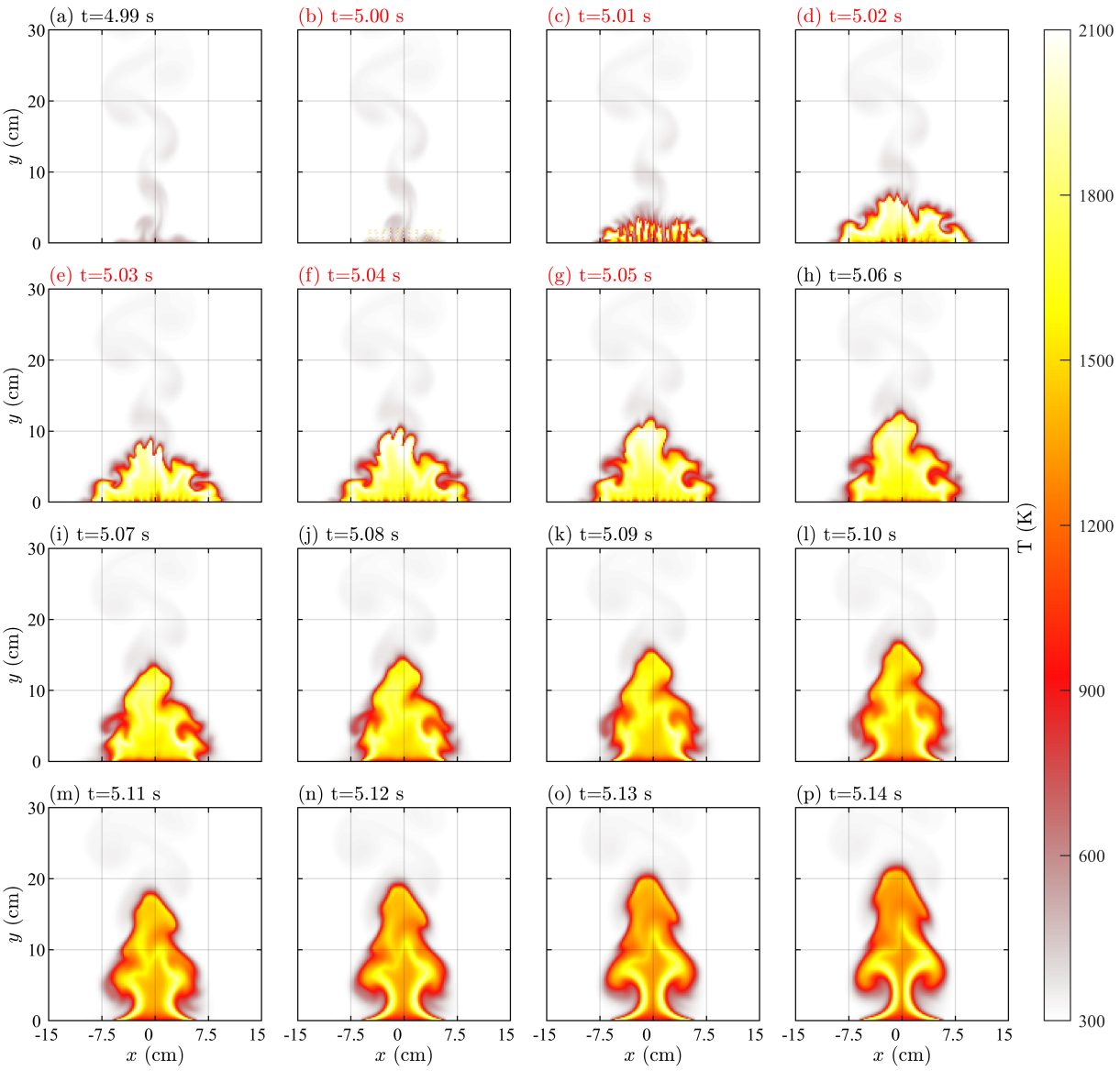


Figure 4.9: Time-series of temperature during ignition with Skeletal-D model, with 0.05 s spark beginning at $t = 5$ s. Time labels written in red indicate when the simulation is under-going the "sparking" process.

(four, and $N_2$ by difference) and reactions (one).

### 4.5.1 Time-Averaged Fields

Time-averaged field quantities — specifically temperature ($T$), heat release rate per unit volume ($\dot{q}$), and the $x$ and $y$ components of velocity ($U_x$ and $U_y$, respectively) — were computed over the final 22.5 s of the simulation to observe how the bulk flow parameters varied with the fidelity of the chemical model. The results are displayed in Figure 4.11 where mean velocity components

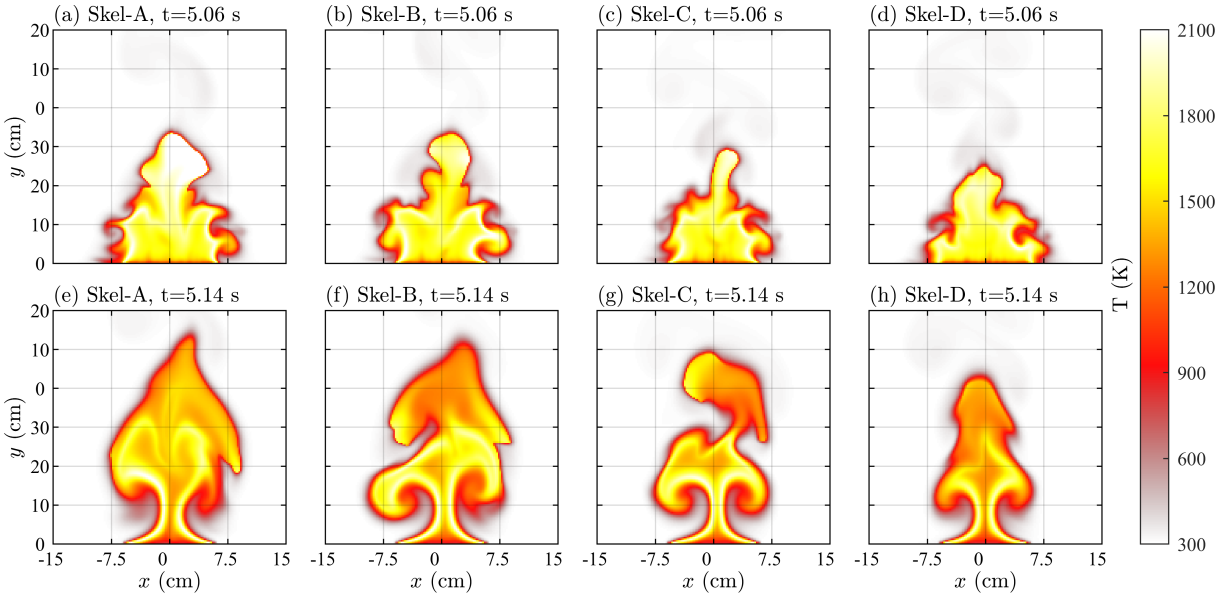


Figure 4.10: Temperature fields for $t = 5.06$ s (a)-(d) and for $t = 5.14$ s (e)-(h). Columns from left to right show the various skeletal kinetic models (Skeletal-A - Skeletal-D).

Table 4.2: Computational time metrics quantifying speed-up of Skeletal-A, -B, -C and -D reduced chemical models and infinitely-fast chemistry (IFC) based on average computational time per 1 s of simulated data and average computational time per 1 iteration.

| Model | Total Comp. Time | Ave. Comp. Time per Iteration | Ave. Comp. Time per 1 s Sim. Time | Speed-up per Iteration \| 1 s Sim. |
|---|---|---|---|---|
| Skeletal-A | 708 hrs | 21.96 s | 23.6 hrs | — |
| Skeletal-B | 389 hrs | 11.62 s | 13.0 hrs | 1.89 \| 1.84 |
| Skeletal-C | 258 hrs | 8.18 s | 8.6 hrs | 2.68 \| 2.74 |
| Skeletal-D | 137 hrs | 4.39 s | 4.6 hrs | 5.00 \| 5.13 |
| $C_xH_yO_z$ IFC | 8.28 hrs | 0.197 s | 0.276 hrs | 111.5 \| 85.5 |

Table 4.3: Computational time metrics quantifying speed-up of tabulated chemistry (ISAT) for Skeletal-A and Skeletal-D based on average computational time per 1 s of simulated data and average computational time per 1 iteration.

| Model | Ave. Time Step | Ave. Comp. Time per Iteration | Ave. Comp. Time per 1 s Sim. Time | Speed-up per Iteration \| 1 s Sim. |
|---|---|---|---|---|
| Skeletal-A w/ ISAT | 25.8 ms | 21.96 s | 23.6 hrs | 2.70 \| 3.96 |
| Skeletal-A w/o ISAT | 17.6 ms | 59.20 s | 93.5 hrs | — |
| Skeletal-D w/ ISAT | 26.5 ms | 4.39 s | 4.6 hrs | 1.80 \| 2.63 |
| Skeletal-D w/o ISAT | 18.2 ms | 7.91 s | 12.1 hrs | — |

are fairly unaffected by the change of chemistry model. However, the most notable difference is seen in $\overline{T}$ and $\overline{\dot{q}}$, the heat release rate per unit volume. Within panes (f)-(j) of Figure 4.11, one can see that the general trend of $\overline{\dot{q}}$ below 10 cm remains fairly consistent, however, the vertical extent and width of the HRR shrinks with the decreased complexity of the chemistry, with the exception of the IFC case which has continued heat release vertically. Upon closer inspection, this lengthening of the reaction zone is reflected in the mean temperature field, in panes (a)-(e) of Figure 4.11. The vertical extent of temperatures that are in the 700 to 800 K range show the same trend as the heat release rate per unit volume as the chemistry fidelity is reduced. These features are intimately linked as regions with higher temperatures are more likely to allow various chemical pathways to activate and thus release energy as reactants move to products. This type of behavior is also demonstrated in the peak temperature change of the reduced chemical kinetics shown in Figure 2.5 where fuel-lean and stoichiometric conditions exhibited the trend of decreasing peak temperature as the detailed mechanism was reduced further. The IFC model requires only ample mixing for reactions to occur, which causes the larger high temperature region as the progression of the combustion does not rely on mixing *and* overcoming the activation energy of chain initiation reactions.

The two velocity components do not vary between the various fidelity models, specifically adhering to the constant rate of entrainment predicted by Morton *et al.* for various types of thermal plumes [112]. Of additional note is the formation of the boundary layer along $y = 0$ cm in Fig-

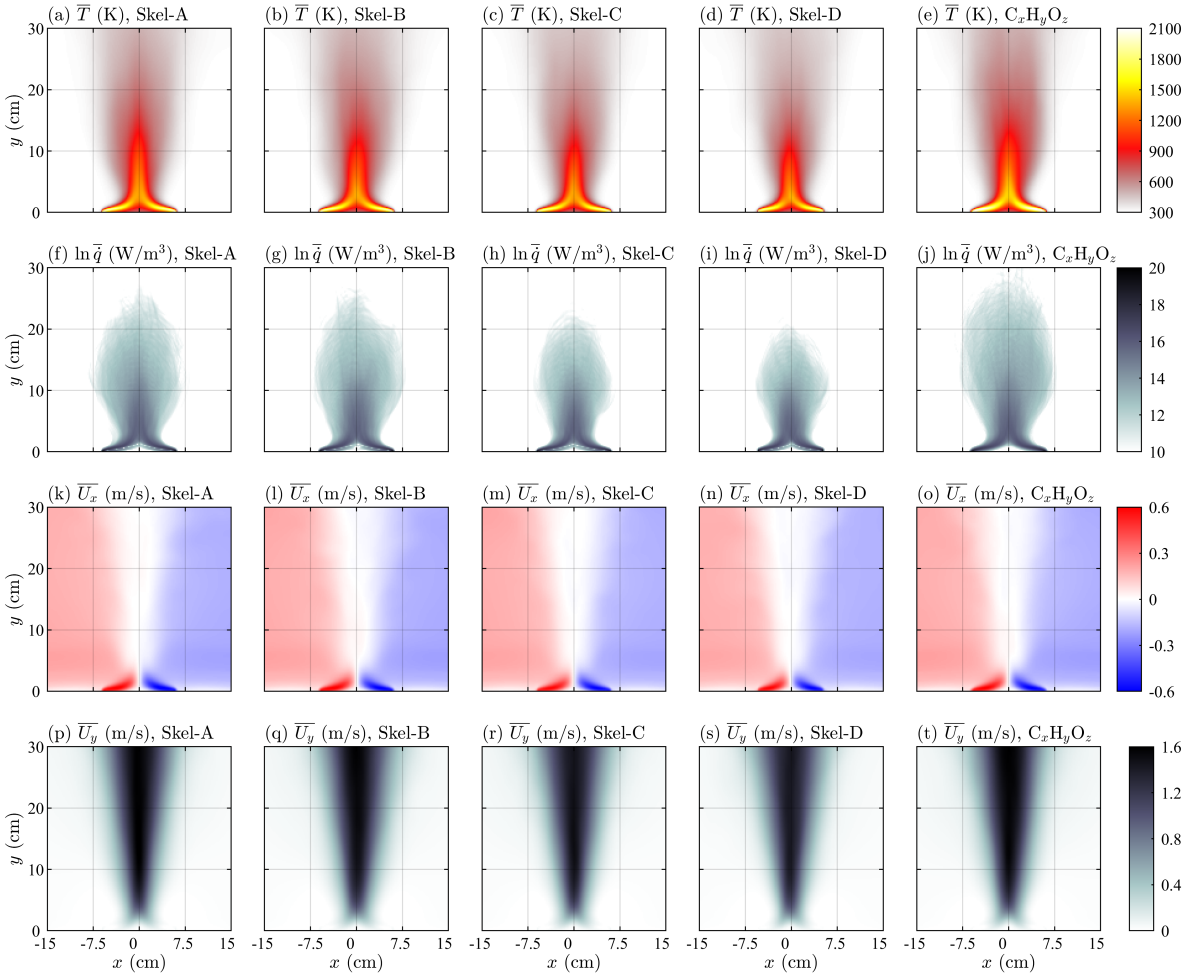


Figure 4.11: Time-averaged fields of the reacting plume of (a)-(e) mean temperature $\overline{T}$ (K), (f)-(j) natural logarithm of mean heat release rate per unit volume $\ln \overline{\dot{q}}$ (W/m$^3$), (k)-(o) mean horizontal velocity $\overline{U_x}$ (m/s) and (p)-(t) mean vertical velocity $\overline{U_y}$ (m/s). Columns from left to right show the various skeletal kinetic models (Skeletal-A - Skeletal-D) and infinitely-fast chemistry ($C_xH_yO_z$). Time averages are taken from $t$ = 7.5-30 s.

ure 4.11(k)-(o). While the base of the simulation, outside of the inlet, is modeled with a 2.5 mm/s co-flow of ambient air, a clear boundary layer is visible with respect to the entrainment structure (shown in red and blue). Within the plume, there is negligible velocity in the $x$ direction as the entrainment flow is quickly being turned in the $y$ direction at the plume's outer edges, seen in panes (p)-(t) of Figure 4.11.

The root mean square (RMS) errors are computed for the fields presented in Figure 4.11 and

Table 4.4: Root mean square (RMS) error, $\varepsilon_{RMS}$, of the time-averaged temperature, volumetric heat release rate, $x$ and $y$ component of velocity fields with respect to Skeletal-A.

| Model | $\varepsilon_{RMS}(\overline{T})$ (K) | $\varepsilon_{RMS}(\overline{\dot{q}})$ (kW/m$^3$) | $\varepsilon_{RMS}(\overline{U_x})$ (m/s) | $\varepsilon_{RMS}(\overline{U_y})$ (m/s) |
|---|---|---|---|---|
| Skeletal-B | 24.78 | 167 | 1.19e-02 | 4.45e-02 |
| Skeletal-C | 29.31 | 506 | 8.81e-03 | 3.86e-02 |
| Skeletal-D | 58.80 | 2592 | 1.74e-02 | 5.42e-02 |
| $C_xH_yO_z$ IFC | 40.33 | 853 | 8.81e-03 | 2.96e-02 |

are presented in Table 4.4. The errors presented demonstrate that the mean velocity fields and the mean temperature field are captured well by all the models, while the volumetric heat release rate is captured well by only Skeletal-B. The high variation in the volumetric heat release rate of Skeletal-C, -D and the lumped fuel IFC models are directly caused by the inconsistent ignition delay time predicted by the models.

The variance fields of quantities of interest are shown in Figure 4.12, where the variance of a quantity is defined by the perturbation value squared. For example, the temperature variance, $(T')^2$, is the difference between the local $T$ field and mean $T$ field, squared; thus, $(T')^2 = \left(T - \overline{T}\right)^2$. Areas of high, time-averaged variance indicate parts of the flow that are most different than the mean flow. Quantities shown do not vary significantly from one model to another (along columns). The $(T')^2$ field, Figure 4.12(a)-(e), indicates that the region of flame expands and contracts at the neck of the plume, and has a left/right sway showing the region of highest variance. Further up, the temperature variance shows the turbulent nature of the flow, which advects high temperature combustion products throughout the plume's extent. The IFC case shows significantly more temperature variance on the average, meaning that the puffing and flapping modes are more vigorously activated. The $(\dot{q}')^2$ field, Figure 4.12(f)-(j) again shows the flame expanding and contracting through the neck of the plume and the variation along the lower center of the plume. The variance of the velocity component fields, $(U_x')^2$ and $(U_y')^2$, are shown in Figure 4.12(k)-(o) and (p)-(t), respectively. Both fields show the variable nature in the plume's "far-field" where turbulence takes over. Below 3 cm, the velocity is extremely low resulting in more laminar, steady flow.

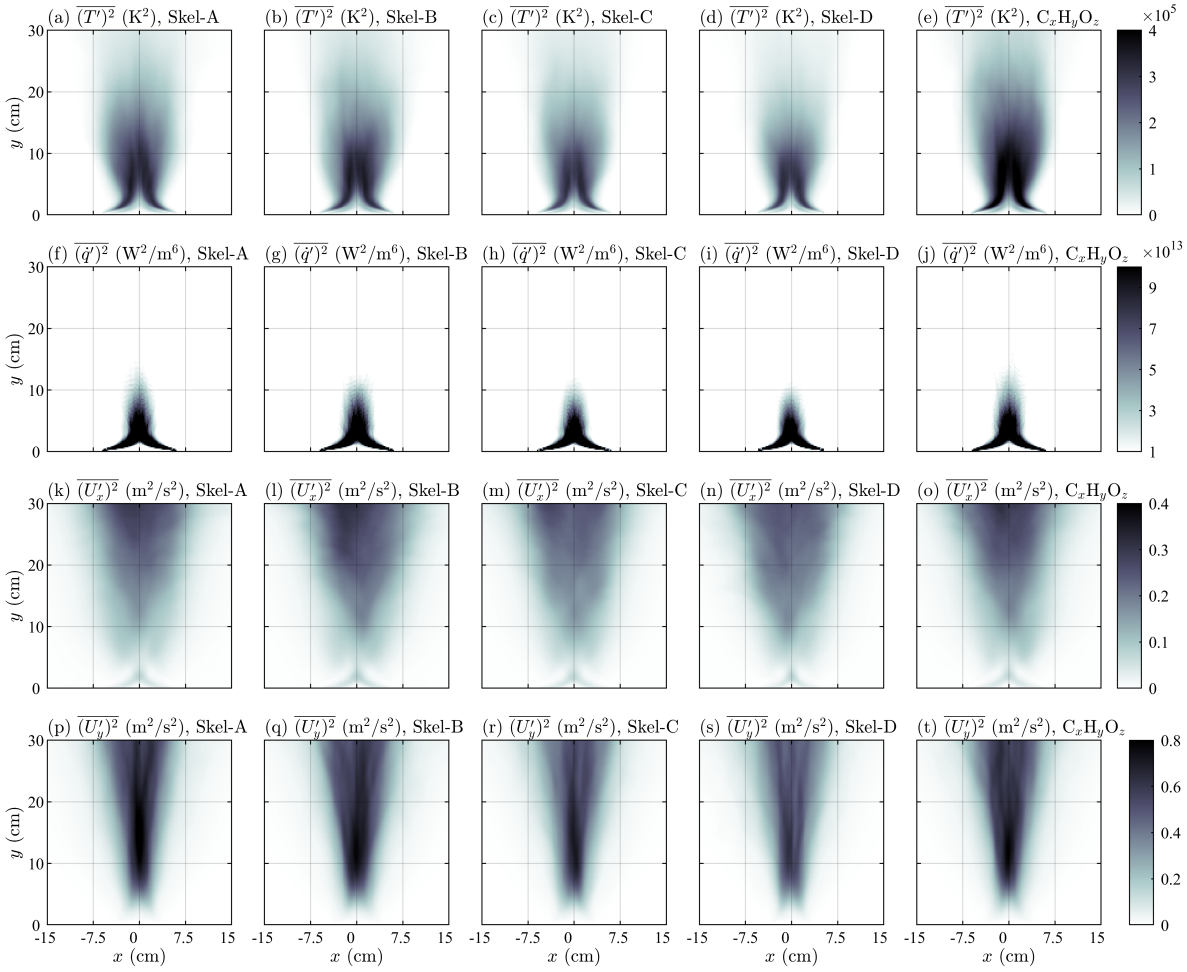


Figure 4.12: Time-averaged fields of the reacting plume of (a)-(e) mean temperature variance $\overline{(T')^2}$ (K$^2$), (f)-(j) mean heat release rate variance $\overline{(\dot{q}')^2}$ (W$^2$/m$^6$), (k)-(o) mean horizontal velocity variance $\overline{(U_x')^2}$ (m$^2$/s$^2$) and (p)-(t) mean vertical velocity variance $\overline{(U_y')^2}$ (m$^2$/s$^2$). Columns from left to right show the various skeletal kinetic models (Skeletal-A - Skeletal-D) and infinitely-fast chemistry (C$_x$H$_y$O$_z$). Time averages are taken from $t$ = 7.5-30 s.

### 4.5.2 Time-Averaged Flow Property Profiles

Time-averaged, vertical profiles taken at $x = 0$ m and horizontal profiles taken at $y = 4$ mm, 3 cm, 6 cm, 12 cm and 18 cm are plotted in Figures 4.13 and 4.14 for various properties of the flow. The vertical profiles are taken for heights ranging from $y = 0$ to 0.55 m (the full vertical extent of the 2 mm resolution section of the grid), and the horizontal profiles are taken across the full horizontal extent of the 2 mm resolution section, from -15 to 15 cm.

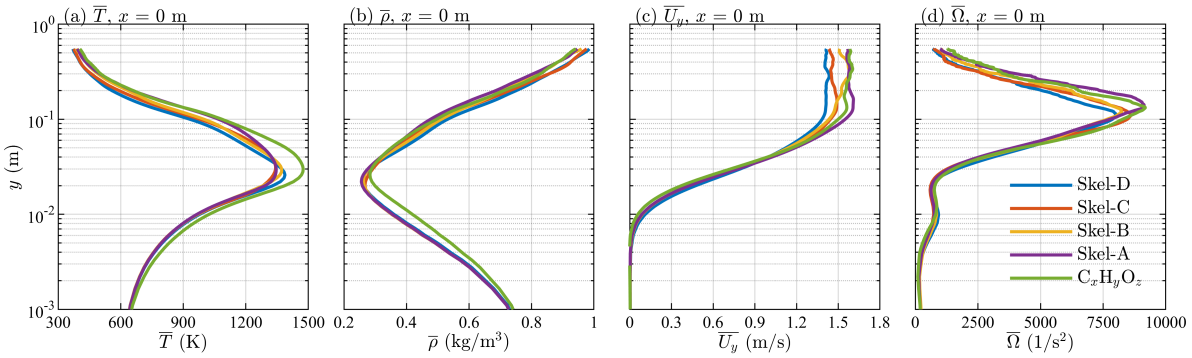


Figure 4.13: Time-averaged, centerline ($x = 0$ m), profiles of the reacting plume of (a) mean temperature $\overline{T}$ (K), (b) mean density $\overline{\rho}$ (kg/m$^3$), (c) mean vertical velocity $\overline{U_y}$ (m/s) and (d) mean enstrophy $\overline{\Omega}$ (1/s$^2$) for each of the various skeletal kinetic models (Skeletal-A - Skeletal-D) and infinitely-fast chemistry ($C_xH_yO_z$). Time averages are taken from $t$ =7.5-30 s.

Figure 4.13 indicates little to no variation over the near-field of the reacting plumes, demonstrating that the reaction kinetics are similar enough to not change flow characteristics in this region. Generally, the profiles remain monotonic when comparing Skeletal-A, -B, -C and -D which is demonstrated best when comparing the temperature, density and vertical velocity profiles in panes (a)-(c), respectively. After the peak temperature at 3 cm above the base, Skeletal-A represents the highest temperature, corresponding to the lowest density and therefore highest velocity. The antithesis can be said for Skeletal-D with the lowest predicted temperature, highest resulting density and slowest vertical velocity. The exception is the IFC simulation which has higher temperature and density, and thus lower vertical velocity on the average when compared to the finite-rate simulations. The enstrophy field ($\Omega$) is calculated based on the curl of the velocity field as

$$\Omega = \frac{1}{2}||\boldsymbol{\nabla} \times \boldsymbol{u}||^2 = \frac{1}{2}\omega_i\omega_i \ , \tag{4.12}$$

where $\omega_i$ is the vorticity component in the $i^{\text{th}}$ direction. Qualitatively speaking, the enstrophy profiles are very similar, with only the magnitude changing, specifically in a way that matches the magnitude of the vertical component of velocity. Given the two-dimensional and symmetric nature of the flow, the magnitude of enstrophy will be dictated most by the magnitude of $U_y$, and the higher fidelity chemistry leads to higher magnitude velocity components and thus higher enstrophy.

Figure 4.14 shows horizontal, time-averaged profiles at various heights, including 4 mm which

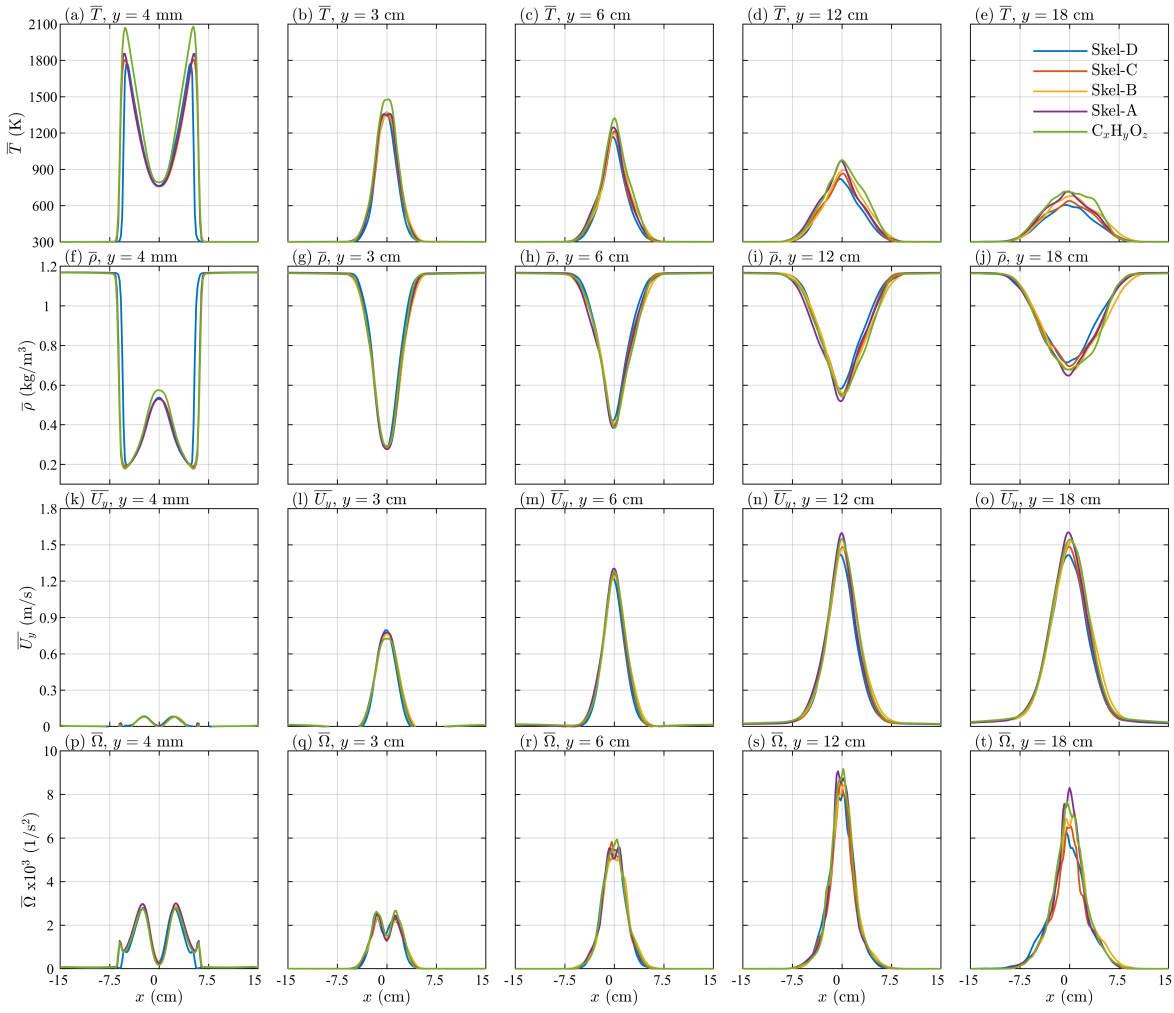


Figure 4.14: Time-averaged, horizontal profiles at $y = 4$ mm, 3 cm, 6 cm, 12 cm and 18 cm, respectively corresponding to columns, of the reacting plume of (a)-(e) mean temperature $\overline{T}$ (K), (f)-(j) mean density $\overline{\rho}$ (kg/m$^3$), (k)-(o) mean vertical velocity $\overline{U_y}$ (m/s) and (p)-(t) mean enstrophy $\overline{\Omega}$ (1/s$^2$) for each of the various skeletal kinetic models (Skeletal-A - Skeletal-D) and infinitely-fast chemistry ($C_xH_yO_z$). Time averages are taken from $t$ =7.5-30 s.

corresponds to the approximate height of the laser in the work presented in Chapter 3. Other heights indicate the development of the flow variables through the near-field, while remaining in the highly resolved area of the simulation. Many of the profiles are very similar to one another, specifically noting the symmetry across $x = 0$ m thus causing the same patterns discussed previously to exist when comparing centerline profiles. However, the profiles at 4 mm in panes (a), (f), (k) and (p) of Figure 4.14 show the direct influence of the inflow conditions causing the centerline trough in

temperature, vertical velocity and enstrophy; and centerline peak in density. Of particular note is how Skeletal-D exhibits clearly "thinner" profiles as compared to the other skeletal models at the lowest height. This is attributed to the longer ignition delay time, thus delaying the expansion of the reaction zone. The same reasoning explains why the IFC simulation captures the "width" of the flame as compared to the higher fidelity models, as the ignition delay time is non-existent for practical purposes. The nature of "mixed-is-burnt" chemistry modeling accounts for the higher and wider peaks of temperature within the inlet ($\pm$6 cm), where only mixing is required for combustion to take place. The preheat zone is not required for the reaction to continue, like in the case of finite-rate chemistry. As the flow reaches higher in the domain, IFC begins to align with the highest fidelity model thus giving confidence to quantifying bulk flow properties using this approximation for the chemical reactions.

The RMS errors are computed for the centerline (CL) profiles as well as heights corresponding to $y$=$D/30$=4 mm (H1) and $y$=1.5$D$=18 cm (H5) presented in Figures 4.13 and 4.14 and are presented in Table 4.5. The IFC of the lumped fuel proves to be the best at capturing the time-averaged, centerline profile of Skeletal-A, followed by each finite-rate chemistry case in terms of their respective fidelity. For buoyant plumes, reacting or non-reacting, capturing the buoyancy-driven features, mainly $\rho$, provides the main flow features, i.e. $U_y$ and $\Omega$. In the case of reacting buoyant plumes that contain perfect gases, $T$ and $\rho$ are related by the ideal gas law, so if the centerline temperature is well captured, the other flow variables presented will also be predicted well along the centerline [113]. The correlation between predicting temperature, and therefore density well and predicting vertical velocity and enstrophy carries through to the horizontal profiles, although here the IFC case does not do as well as the Skeletal-B or Skeletal-C models. This is clearly due to the over-prediction of flame temperature and concludes that additional tuning of `C` (mixing parameter in OpenFOAM's IFC implementation) or radiation parameters are required for this particular model to be used more accurately for these cases.

Table 4.5: Root mean square (RMS) error, $\varepsilon_{RMS}$, of the time-averaged, centerline (CL), height of 4 mm (H1), and height of 18 cm (H5) of temperature, density, vertical velocity and enstrophy profiles with respect to Skeletal-A.

| Model | $\varepsilon_{RMS}(\overline{T})$ (K) CL \| H1 \| H5 | $\varepsilon_{RMS}(\overline{\rho})$ (kg/m$^3$) CL \| H1 \| H5 (x10$^{-3}$) | $\varepsilon_{RMS}(\overline{U_y})$ (cm/s) CL \| H1 \| H5 | $\varepsilon_{RMS}(\overline{\Omega})$ (1/s$^2$) CL \| H1 \| H5 |
|---|---|---|---|---|
| Skeletal-B | 33.0 \| 7.8 \| 21.8 | 19.4 \| 3.1 \| 22.9 | 6.1 \| 0.2 \| 5.6 | 749 \| 43 \| 335 |
| Skeletal-C | 51.5 \| 23.0 \| 30.2 | 38.4 \| 7.3 \| 19.0 | 10.8 \| 0.2 \| 4.2 | 1078 \| 88 \| 519 |
| Skeletal-D | 76.7 \| 259.1 \| 45.3 | 49.7 \| 157.8 \| 27.9 | 15.4 \| 1.2 \| 6.0 | 1292 \| 276 \| 546 |
| $C_xH_yO_z$ IFC | 36.7 \| 110.0 \| 32.6 | 20.9 \| 20.4 \| 18.9 | 3.0 \| 0.5 \| 3.5 | 464 \| 112 \| 231 |

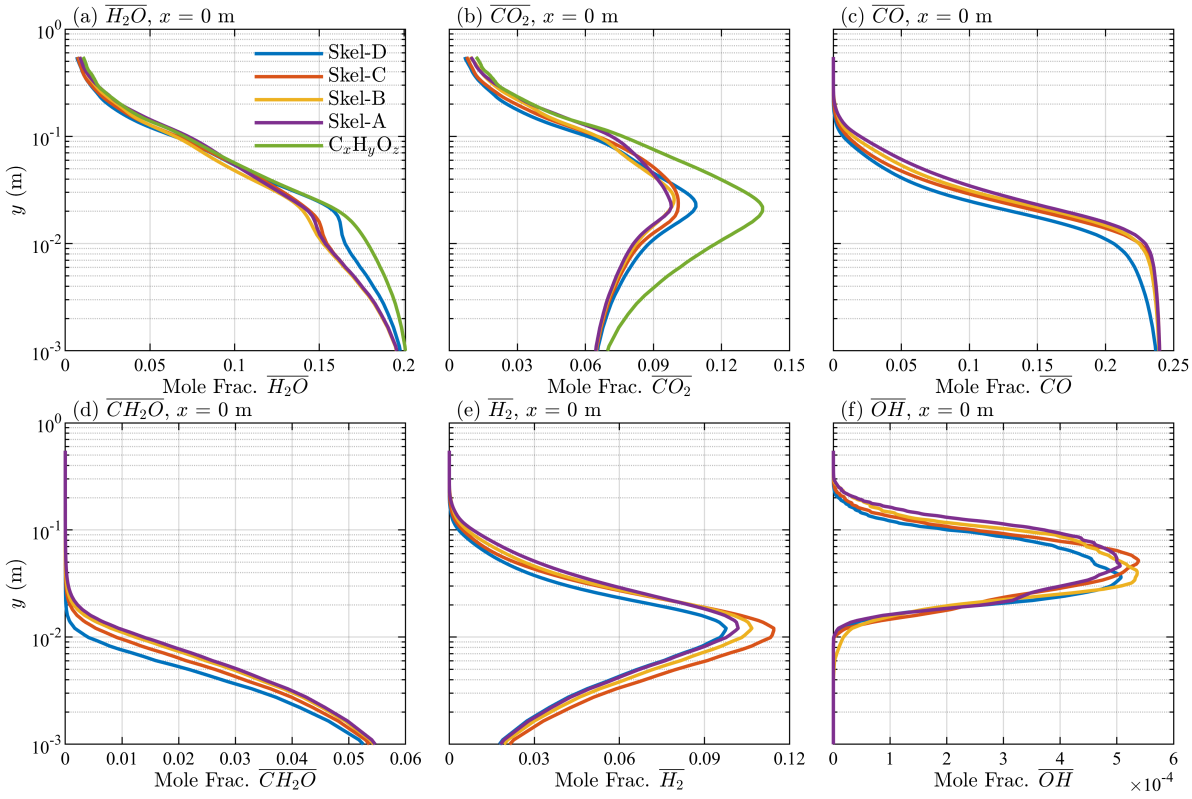


Figure 4.15: Time-averaged, centerline ($x$ = 0 m), profiles of the reacting plume of (a) mean water mole fraction $\overline{X_{\mathrm{H_2O}}}$, (b) mean carbon dioxide mole fraction $\overline{X_{\mathrm{CO_2}}}$, (c) mean carbon monoxide mole fraction $\overline{X_{\mathrm{CO}}}$, (d) mean formaldehyde mole fraction $\overline{X_{\mathrm{CH_2O}}}$, (e) mean hydrogen mole fraction $\overline{X_{\mathrm{H_2}}}$ and (f) mean hydroxyl radical mole fraction $\overline{X_{\mathrm{OH}}}$ for each of the various skeletal kinetic models (Skeletal-A - Skeletal-D) and infinitely-fast chemistry ($C_xH_yO_z$). The $C_xH_yO_z$ model does not contain species besides $H_2O$ and $CO_2$. Time averages are taken from $t$ =7.5-30 s.

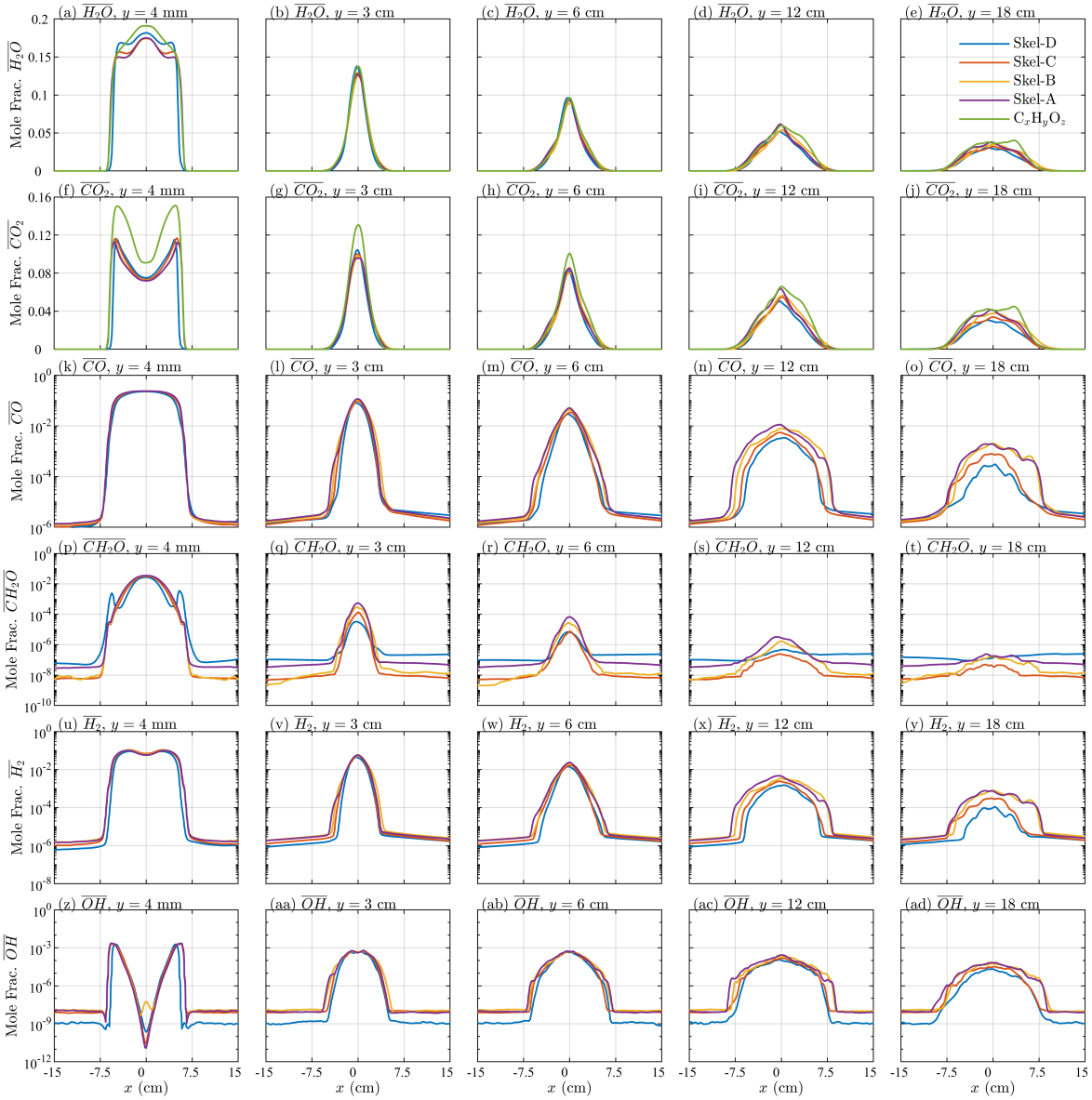


Figure 4.16: Time-averaged, horizontal profiles at $y$ = 4 mm, 3 cm, 6 cm, 12 cm and 18 cm, respectively corresponding to columns, (a)-(e) mean water mole fraction $\overline{X_{\mathrm{H_2O}}}$, (f)-(j) mean carbon dioxide mole fraction $\overline{X_{\mathrm{CO_2}}}$, (k)-(o) mean carbon monoxide mole fraction $\overline{X_{\mathrm{CO}}}$, (p)-(t) mean formaldehyde mole fraction $\overline{X_{\mathrm{CH_2O}}}$, (u)-(y) mean hydrogen mole fraction $\overline{X_{\mathrm{H_2}}}$ and (z)-(ad) mean hydroxyl radical mole fraction $\overline{X_{\mathrm{OH}}}$ for each of the various skeletal kinetic models (Skeletal-A - Skeletal-D) and infinitely-fast chemistry ($\mathrm{C}_x\mathrm{H}_y\mathrm{O}_z$). The $\mathrm{C}_x\mathrm{H}_y\mathrm{O}_z$ model does not contain species besides $\mathrm{H_2O}$ and $\mathrm{CO_2}$. Time averages are taken from $t$ =7.5-30 s.

### 4.5.3 Time-Averaged Specie Profiles

Time-averaged, vertical profiles of taken at $x = 0$ m and horizontal profiles taken at $y = 4$ mm, 3 cm, 6 cm, 12 cm and 18 cm are plotted in Figures 4.15 and 4.16 for various important species.

The vertical profiles are taken for heights ranging from $y = 0$ to 0.55 m (the full vertical extent of the 2 mm resolution section of the grid), and the horizontal profiles are taken across the full horizontal extent of the 2 mm resolution section, from -15 to 15 cm.

The non-linear nature of mechanism reduction is demonstrated through the non-monotonic nature of the various specie plots shown in Figure 4.15 where the fidelity of the chemical model is not necessarily representative of the relative mole fraction predicted by it, when compared to the other skeletal models. Along the centerline, the temperature reaches the maximum at around 10 cm, which correlates well with the destruction of carbon monoxide (c), formaldehyde (d) and hydrogen gas (e); it also is represented by the intense production of the hydroxyl radical (f) for the four finite-rate cases (the IFC case omits these species). The centerline peak in temperature also accounts for the change in the profile of water (a), where the mole fraction reduction, via mixing with air, of water slows down through the flame, where it is produced by combustion. This process is further extenuated by the production of carbon dioxide (b) where a clear peak occurs through the flame front. The benefits and drawbacks of IFC are clearly displayed throughout Figure 4.15 by the clear absence of $C_xH_yO_z$ prediction of mole fractions in panes (c)-(f). Furthermore, the near-field concentrations of $H_2O$ and $CO_2$ are clearly outlying when compared to the higher fidelity models, specifically Skeletal-A, -B and -C. Due to the fact that in the near-field, IFC can only produce water and carbon dioxide, it is not surprising that these are over-predicted as intermediate and dissociative species do not exist, which would lower their respective concentrations. However, as the flow increases in height, the mole fractions of $H_2O$ and $CO_2$ begin to track with the other chemical models.

Figure 4.16 allows the classification of the various fidelity's when comparisons of formaldehyde (p)-(t) and the hydroxyl radical (z)-(ad) are examined. The nominal mole fraction of $CH_2O$ and OH differ by roughly an order of magnitude outside of the plume, but are predicted well within the reaction zone. The lack of agreement outside of the reaction zone is likely due to the different specie sets in each skeletal model leading to different equilibrium concentrations at lower temperatures in trace species. The general agreement within the reacting plume further increases the confidence

Table 4.6: Root mean square (RMS) error, $\varepsilon_{RMS}$, of the time-averaged, centerline (CL), height of 4 mm (H1), and height of 18 cm (H5) of $H_2O$ and $CO_2$ mole fraction profiles with respect to Skeletal-A.

| Model | $\varepsilon_{RMS}(\overline{X_{H_2O}})$ (x$10^{-5}$) CL \| H1 \| H5 | $\varepsilon_{RMS}(\overline{X_{CO_2}})$ (x$10^{-5}$) CL \| H1 \| H5 |
|---|---|---|
| Skeletal-B | 356.7 \| 33.5 \| 258.4 | 315.9 \| 45.9 \| 287.7 |
| Skeletal-C | 389.6 \| 249.5 \| 253.5 | 497.5 \| 320.5 \| 343.1 |
| Skeletal-D | 592.4 \| 2037.5 \| 376.0 | 760.4 \| 1872.6 \| 552.7 |
| $C_xH_yO_z$ IFC | 478.7 \| 1030.7 \| 406.6 | 1062.8 \| 2344.9 \| 476.2 |

in the reduction method and the resulting skeletal models. Furthermore, the overall agreement in main combustion species over various heights in the flow is encouraging for each reduced model. The deviations as height increases are attributable to each model predicting the end of reactions at different heights. Once again, IFC does not capture near-field mole fractions of $H_2O$ and $CO_2$, but does capture the thickness of the profiles predicted by the higher fidelity models. The predictions of water and carbon dioxide improve with height downstream of the inlet and align closely with Skeletal-A in magnitude and profile shape.

The RMS errors are computed for the centerline (CL) profiles as well as heights corresponding to $y$=$D/30$=4 mm (H1) and $y$=1.5$D$=18 cm (H5) presented in Figures 4.15 and 4.16 and are presented in Tables 4.6 and 4.7. Skeletal-B does consistently well at modeling the mole fractions of important species to combustion processes predicted when utilizing Skeletal-A for the chemical kinetics. Of particular interest is how well the infinitely-fast chemistry case captures the centerline and H5 water mole fraction for the level of simplification involved in IFC. On the contrary, there are two orders of magnitude between the RMS error of Skeletal-B compared to that of Skeletal-D and the IFC case at H1 in water mole fraction. This would indicate that Skeletal-D and IFC would not be suitable choices for predicting near-field water mole fraction, specifically when considering implementing this work into the framework presented in Chapter 3. Furthermore, the RMS error data for species not available in IFC at H1 indicate that Skeletal-D may not be the best choice when the quantities of interest are various species that are the products or indicators of combustion.

Table 4.7: Root mean square (RMS) error, $\varepsilon_{RMS}$, of the time-averaged, centerline (CL), height of 4 mm (H1), and height of 18 cm (H5) of CO, $CH_2O$, $H_2$ and OH mole fraction profiles with respect to Skeletal-A.

| Model | $\varepsilon_{RMS}(\overline{X_{CO}})$ (x$10^{-5}$) CL \| H1 \| H5 | $\varepsilon_{RMS}(\overline{X_{CH_2O}})$ (x$10^{-5}$) CL \| H1 \| H5 | $\varepsilon_{RMS}(\overline{X_{H_2}})$ (x$10^{-5}$) CL \| H1 \| H5 | $\varepsilon_{RMS}(\overline{X_{OH}})$ (x$10^{-5}$) CL \| H1 \| H5 |
|---|---|---|---|---|
| Skeletal-B | 359.0 \| 96.2 \| 15.0 | 21.8 \| 46.4 \| 4.84e-03 | 162.4 \| 216.2 \| 6.3 | 2.7 \| 1.5 \| 0.5 |
| Skeletal-C | 691.2 \| 780.6 \| 51.1 | 67.8 \| 188.3 \| 8.31e-03 | 318.2 \| 587.6 \| 20.4 | 4.1 \| 9.1 \| 1.2 |
| Skeletal-D | 1151.3 \| 1971.0 \| 68.1 | 135.5 \| 424.1 \| 1.14e-02 | 440.9 \| 979.3 \| 27.1 | 5.8 \| 45.1 \| 1.7 |

### 4.5.4 Line of Sight Averaged Temperature and Water Mole Fraction

The properties and composition of the inflow mimicked the general composition of the pyrolysate diffusing off the Douglas fir block of wood in Chapter 3, sans the water vapor in the ambient air. The resulting temperature, Figure 4.14(a), and water mole fraction, Figure 4.16(a), profiles at a height of 4 mm show clear inhomogeneities across the line of sight where measurements were taken in the previous chapter. Specifically, Skeletal-D exhibits a thinner flame which results in a significant drop in the temperature and water mole fraction that would be "seen" by laser diagnostics at in this region. Specifically the line of sight average of the mean temperature, denoted $\langle\overline{T}\rangle$, and mean water mole fraction, denoted $\langle\overline{H_2O}\rangle$, are presented in Table 4.8.

These line of sight averaged quantities do not have a one-to-one correspondence with those presented in Chapter 3, but do hint at the upper limit of water vapor production for a given amount of pyrolysate. This leads to the conclusion that the boundary conditions implemented to capture

Table 4.8: Line of sight averages at $y = 4$ mm over the 12 cm inlet of the skeletal models and infinitely-fast chemistry and relative difference with respect to that of Skeletal-A.

| Model | $\langle\overline{T}\rangle$ (K) | $\langle\overline{H_2O}\rangle$ | Relative Difference (%) $\langle\overline{T}\rangle$ \| $\langle\overline{H_2O}\rangle$ |
|---|---|---|---|
| Skeletal-A | 1228 | 0.1517 | — |
| Skeletal-B | 1219 | 0.1515 | 0.73 \| 0.13 |
| Skeletal-C | 1222 | 0.1541 | 0.49 \| 1.58 |
| Skeletal-D | 1115 | 0.1508 | 9.20 \| 0.59 |
| $C_xH_yO_z$ IFC | 1374 | 0.1643 | 11.89 \| 8.31 |

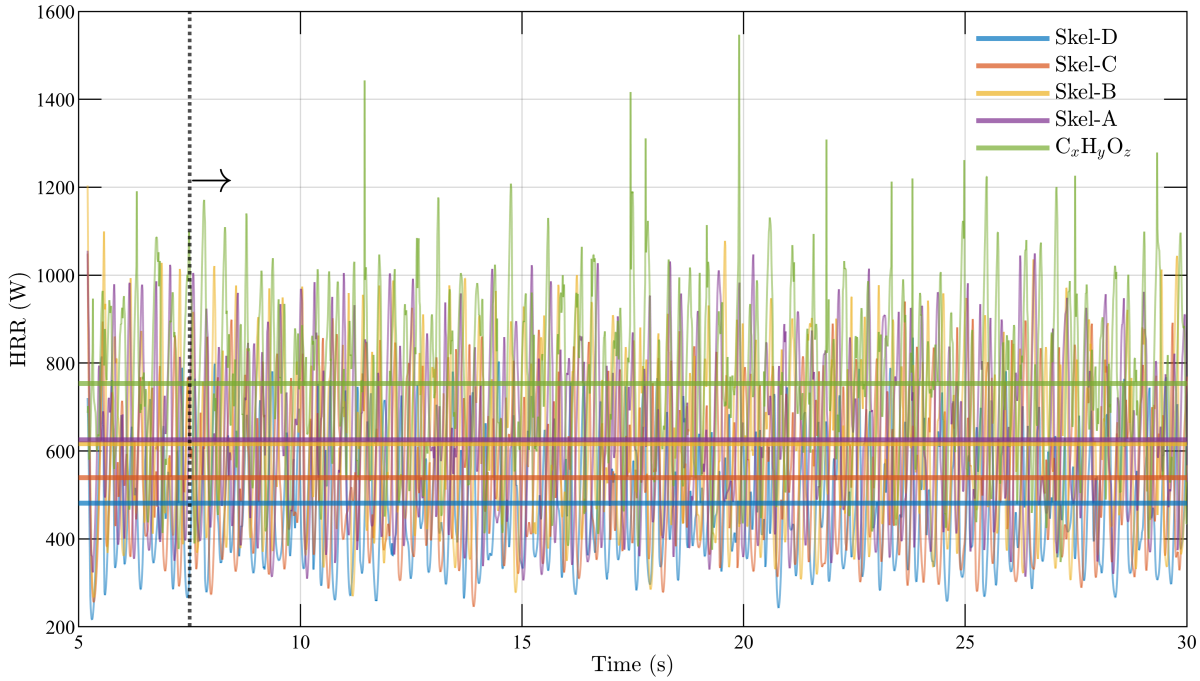


Figure 4.17: Time-series of integrated heat release rate (HRR) with dashed black line showing $t = 7.5$ s when signal processing begins; solid colored lines show average value of HRR for each reduced kinetic model and infinitely-fast chemistry.

the gas in the solid-region becoming pyrolysate in the gas-region may under-predict the amount of fuel in the composition (this would show up as nitrogen at the interface between the regions).

### 4.5.5 Heat Release and the Puffing Frequency

The time history of the volume integrated heat release rate (HRR) is shown for the four skeletal models and IFC case in Figure 4.17, along with the respective mean value, ($\overline{\text{HRR}}$). The HRR signal is a highly fluctuating quantity that is dependent on the extent of reactions taking place in the entire domain. Based on the average temperature and heat release fields in Figure 4.11(a)-(j), one can see that majority of the heat release occurs at the neck of plume where the highest temperatures exist. This is also observed in the variances of the temperature and heat release fields in Figure 4.12(a)-(j), where the highest variances occur in the neck of the plume.

The total heat release is calculated by integrating the HRR profiles in Figure 4.17 with respect

Table 4.9: Total heat release of the skeletal models and infinitely-fast chemistry and relative difference with respect to that of Skeletal-A.

| Model | Total Heat Release (kJ) | Relative Difference (%) |
|---|---|---|
| Skeletal-A | 15.84 | — |
| Skeletal-B | 15.30 | 3.41 |
| Skeletal-C | 13.37 | 15.59 |
| Skeletal-D | 11.93 | 24.68 |
| $C_xH_yO_z$ IFC | 22.60 | 42.68 |

to time. The total heat release and relative error of each reduced model is reported in Table 4.9. As expected based on the volumetric heat release, shown in Figure 4.6, as the fidelity of the finite-rate chemical kinetics is reduced, the amount of total heat release decreases. Infinitely-fast chemistry produces almost 50% more heat release when compared to Skeletal-A, attributable to the larger region of the reaction taking place, depending only on the fuel and oxidizer mixing and that IFC inherently models complete combustion.

The volume integrated total heat release compares poorly between the various models which reflects the size of the domain in which heat release is actively occurring, visualized in Figure 4.11. One notes that below $y = 10$ cm where the maximum heat release rate is, the various models are similar. The maximum, or peak, heat release rate per unit volume (HRR/V) is shown as a time-series in Figure 4.18 along with the average value of HRR/V, also shown in Table 4.10. The data shown in Table 4.10 indicates an agreement for Skeletal-B, Skeletal-C and the lumped fuel in capturing the maximum heat release rate per unit volume of Skeletal-A; the Skeletal-D model results in a higher relative difference than the other simplified models. The error in the lumped fuel specie points to a need to reduced the error of the thermodynamic property fit at 298 K, where the enthalpy function would represent the enthalpy of formation. The heat release rate is strongly tied to the enthalpy of formation and the sensible enthalpy.

The characteristic "puffing" behavior can be distinguished in panes (h)-(p) of Figure 4.9 where combustion products are being accelerated upwards due to buoyancy (lower density compared to the ambient fluid) which entrains denser fluid from the edges of the domain. The puffing is visually

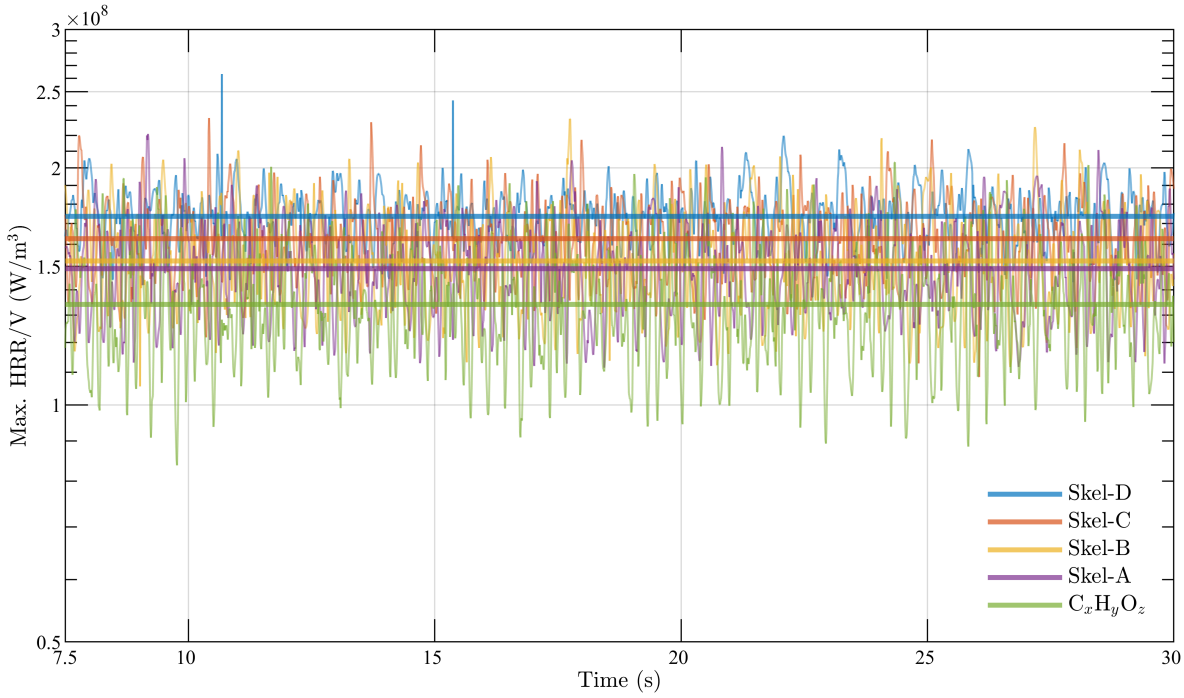


Figure 4.18: Time-series of maximum heat release rate per unit volume (HRR/V); solid colored lines show average value of HRR/V for each reduced kinetic model and infinitely-fast chemistry.

Table 4.10: Peak heat release per unit volume of the skeletal models and infinitely-fast chemistry and relative difference with respect to that of Skeletal-A.

| Model | Peak Heat Release per Volume ($MW/m^3$) | Relative Difference (%) |
|---|---|---|
| Skeletal-A | 3352 | — |
| Skeletal-B | 3428 | 2.26 |
| Skeletal-C | 3658 | 9.13 |
| Skeletal-D | 3906 | 16.52 |
| $C_xH_yO_z$ IFC | 3020 | 9.90 |

noted by the "pooling" and "necking" of the plume, due to the combination of combustion products being mixed with the entrained air.

To quantify the puffing frequency, the fast-Fourier transform (FFT) of the fluctuating volume integrated heat release rate, HRR′, signal is used and converted to a power spectral density (PSD). The HRR′ signal at a given time is defined by the following:

$$\mathrm{HRR}'(t) = \int_V \dot{q}(t,x,y,z)dV - \overline{\int_V \dot{q}(t,x,y,z)dV} \ , \tag{4.13}$$

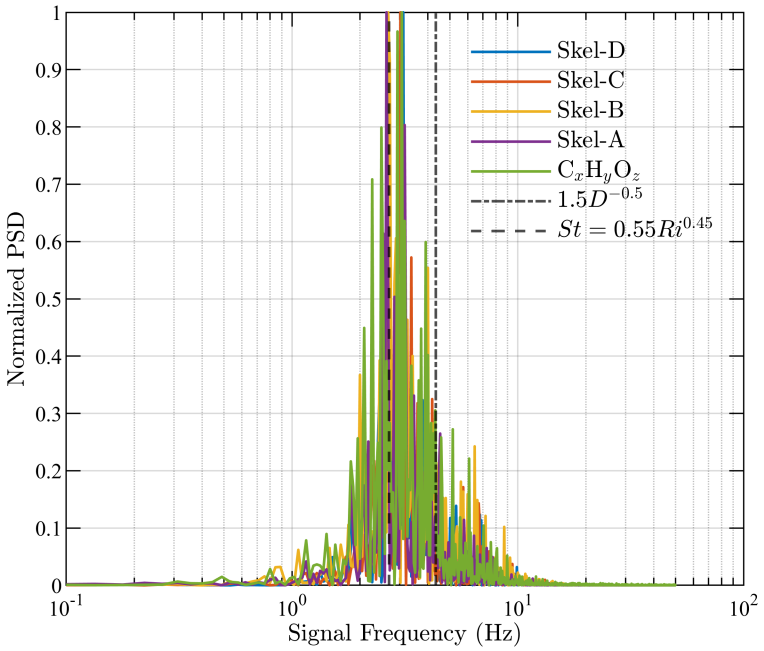


Figure 4.19: Analytical power spectral density of the HRR′ signal, using an FFT for Skeletal-A, -B, -C and -D and infinitely-fast chemical models. The dot-dash line is the 4.33 Hz frequency predicted by $1.5D^{-0.5}$ for reacting plumes. The dash-dash line is the 2.695 Hz frequency predicted by $St = 0.55Ri^{0.45}$ for planar plumes.

where $\dot{q}$ is the heat release rate, per unit volume (in units of kg/(m·s$^3$) or W/m$^3$), thus the measure HRR($t$) is one of power (in units of W). The HRR profile in Figure 4.17, is a preferable candidate for the PSD given the oscillatory nature of the signal and the spatial independence of the computed value.

The noisy nature of the HRR signal creates a broadband frequency spectrum in the PSD, seen in Figure 4.19, therefore an estimated PSD is presented through the use of Welch's method [114], in Figure 4.20. This method breaks up the time-domain signal, computing the FFT and PSD of each individual portion and then averaging the various results of each PSD to create a less noisy frequency spectrum with 0.01 Hz discretization. Comparisons of the true PSD and associated approximated PSD are shown in Appendix C in Figures C.1 through C.5.

The puffing frequency of a 3D reacting plume has been predicted to vary with diameter as $1.5D^{-0.5}$, thus predicting a dominant frequency at 4.33 Hz, regardless of the fuel [75]. This

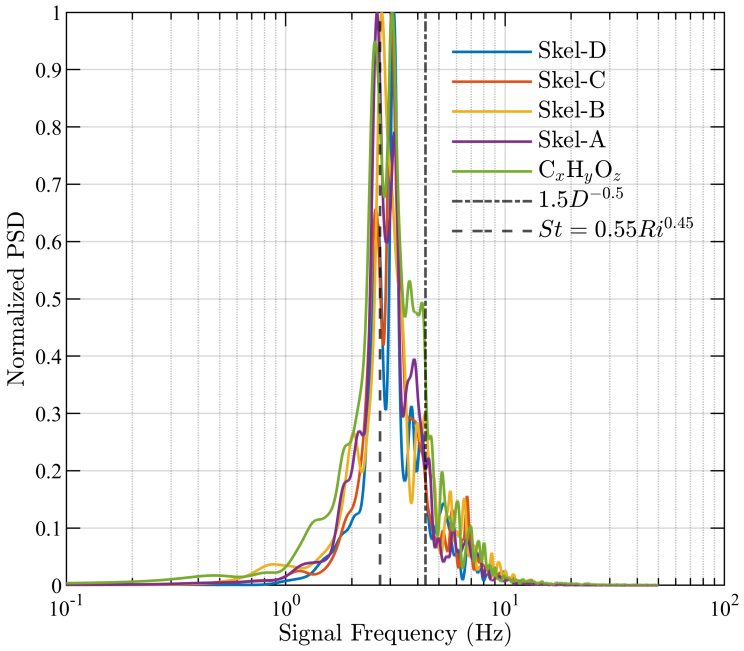


Figure 4.20: Average power spectral density of the HRR′ signal, using Welch's method for Skeletal-A, -B, -C and -D and infinitely-fast chemical models. The dot-dash line is the 4.33 Hz frequency predicted by $1.5D^{-0.5}$ for reacting plumes. The dash-dash line is the 2.695 Hz frequency predicted by $St = 0.55Ri^{0.45}$ for planar plumes.

prediction was updated in later work for planar plumes to $St = 0.55Ri^{0.45}$ using the diameter/width as the characteristic length scale [74] and will be used for comparison to the 2D reacting plumes. Since the density will vary throughout the centerline of a reacting buoyant plume, a characteristic density at combustion temperatures is used, based on perfectly-stirred reactor post-combustion conditions, namely $\rho = 0.178$ kg/m$^3$. The ambient density is 1.164 kg/m$^3$, the inflow velocity is 0.005 m/s from an inlet of width 0.12 m and acceleration due to gravity is 9.81 m/s$^2$. Using the planar plume correlation, a characteristic frequency of 2.695 Hz is predicted. The 3D reacting plume and planar plume characteristic frequencies are visualized on Figures 4.19 and 4.20 for visual comparison.

The first and second most dominant frequencies of the various fidelity chemical models are presented in Table 4.11. The relative error of each model's first and second most dominant frequencies, predicted by the fluctuating heat release rate signal, are compared to the predicted value of

Table 4.11: First and second most dominant frequencies and relative error of the skeletal models and infinitely-fast chemistry, based on power spectral density of HRR′ with respect to Skeletal-A and the $St = 0.55Ri^{0.45}$ correlation for planar plumes.

| Model | Dominant Frequencies (Hz) | Norm. PSD ($2^{\text{nd}}$ Peak) | Relative Error to Skel-A (%) | Relative Error to $St = 0.55Ri^{0.45}$ (%) |
|---|---|---|---|---|
| Skeletal-A | 2.66 \| 3.08 | 0.87 | — | 1.3 \| 14.3 |
| Skeletal-B | 2.67 \| — | — | 0.4 \| — | 0.9 \| — |
| Skeletal-C | 3.02 \| 2.58 | 0.66 | 13.5 \| 3.0 | 12.1 \| 4.3 |
| Skeletal-D | 3.11 \| 2.63 | 0.63 | 16.9 \| 1.1 | 15.4 \| 2.4 |
| $C_xH_yO_z$ IFC | 3.07 \| 2.55 | 0.95 | 15.4 \| 4.1 | 13.9 \| 5.4 |

2.695 Hz, noting in Figure 4.20 that an additional, peak in the IFC, Skeletal-C and Skeletal-D cases of 2.55, 2.58 and 2.63 Hz, respectively (with a normalized PSDs of 0.95, 0.66 and 0.63, respectively) show up as the second most dominant mode of oscillation. Further, Skeletal-A indicates a second mode at 3.08 Hz which is very similar to frequencies predicted by the more reduced models. This points to the potential of two modes being activated in the reacting plumes. Skeletal-B lacks a second peak when using the average PSD and is left off. With the second peak being taken into consideration, each of the various models predicts a frequency at nearly the 2.695 Hz predicted planar plume puffing frequency or at slightly higher 3.1 Hz which is not reflected in any empirical fits for reacting or non-reacting buoyant plumes. This dual-mode PSD may be resolved if longer simulation times were performed to get stronger dominant frequencies of each respective signal as the data analyzed would provide around eighty to ninety total puffs, for each simulation.

The overall agreement of the predicted puffing frequency from planar (pseudo-2D) plume theory in a non-reacting helium plume and the observed puffing frequency of a purely 2D reacting plume backs up at nearly three decades of work in which non-reacting plumes have been used in lieu of their reacting counterparts [40, 73, 115]. Additionally, the findings presented by Cetegen and Ahmed for the puffing frequency being fairly independent of the fuel burned, both in composition and in phase, were demonstrated by the two dominant frequencies being captured by all five chemical kinetic models [75].

To validate the method of utilizing the fluctuating volume integrated heat release as an

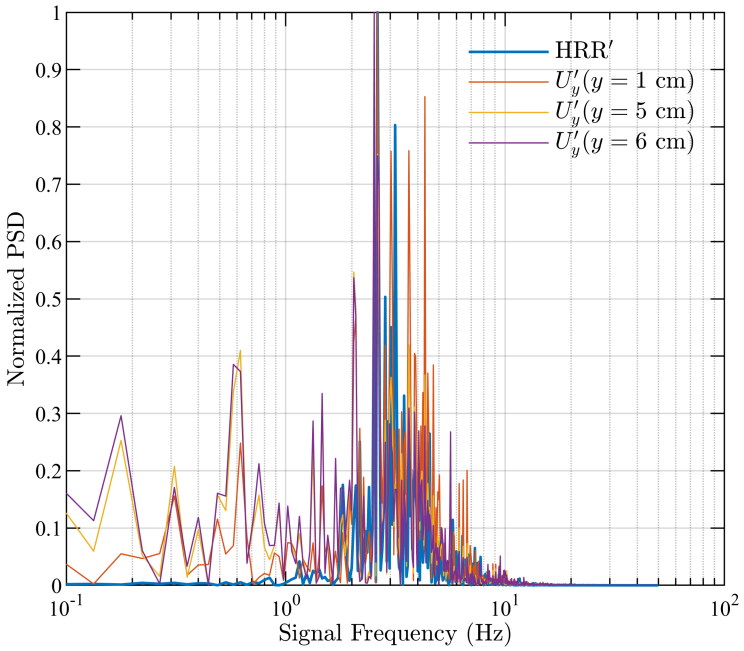


Figure 4.21: Comparison of the normalized PSD, calculated via HRR′ (blue), and $U_y'$ at 1 cm (red), 5 cm (yellow) and 6 cm (purple) along the centerline for Skeletal-A.

objective quantity to extract the puffing frequency from, it will be compared to a typical method of utilizing the fluctuating stream-wise velocity ($U_y'$) at specific downstream distances from the inlet [79, 81, 82, 116, 117]. Figure 4.21 shows the normalized PSD comparing the two methods of obtaining the frequency spectrum associated with the Skeletal-A case for three choices of distances downstream. Appendix D contains the same comparisons for Skeletal-B, -C, -D and infinitely-fast chemistry of the lumped specie, $C_xH_yO_z$ in Figures D.1 through D.4. Of particular note is that the usage of HRR′ as the quantity of interest for obtaining the frequency content is accurate when comparing to using $U_y'$ at the typical height of $D/2$ (shown in purple). An additional benefit is the lack of low-frequency content in the HRR′ PSD. While this method was able to work for the cases shown, it would require additional study before more widely accepted as an objective method for quantifying the puffing frequency of reacting plumes.

## 4.6 Conclusions

In this work, the relative benefits and influence on the flow of reduced combustion models and numerical techniques for solving complex, multi-step chemistry in a CFD simulation were assessed. The simulations were performed in two-dimensions, utilizing a static, nested grid; the extension to three-dimensions would allow for the use of AMR and additional scalability of tabulated chemistry for more benefits. While data was not available to compare to the original mechanism, significant cost savings of a five times speed-up were shown when comparisons were made to the reduced model that incurred 0.81% error, Skeletal-A, with respect to the full parent mechanism. Furthermore, the use of tabulated chemistry showed that even for reduced chemistry, there is between a 2 and 4 times speed-up which allows for more realistic, complex simulations to be performed in a tractable amount of time. Infinitely-fast combustion of a lumped fuel specie with mixture-averaged properties of the pyrolysate provided a speed-up factor of 85 when compared with Skeletal-A in the real-time required to simulate one second of data, on average.

The simulations presented in this work demonstrated the influence of ignition delay time and total heat release on the flow properties and specie concentrations. It was shown that the more reduced, finite-rate, models lead to a longer ignition delay time, thus hindering the expansion of the reacting plume resulting in a slightly smaller reaction zone with less heat release. The results of the smaller, cooler, plume were shown to decrease the vertical velocity, enstrophy and resulted in a deficit in various species in the flame at low heights. The qualitative and quantitative agreement across the flow structure, specie concentrations and puffing frequency leads to the conclusion that simulating reacting plumes correctly relies on capturing the mixing of fuel and oxidizer and capturing the heat release of the reaction; this would represent a mixing-limited diffusion flame. In the case of a mixing-limited diffusion flame, infinitely-fast chemistry has been an appropriate approximation to reduce the complexities associated with multi-step chemistry when general flow structure is the interested factor [59, 79, 81, 82, 117]. In general, the infinitely-fast chemistry model presented here, of the lumped specie designed to have consistent thermodynamic properties to that

of the inflow composition, showed good agreement with the highest fidelity model when comparing bulk flow properties. The main drawback, and benefit, of using infinitely-fast chemistry is the lack of chemical species, which in turn allows for significant computational speed-up. Further, infinitely-fast chemistry results in a larger high-temperature area, analogous to the flame, due to the "mixed-is-burnt" model that requires only fuel and oxidizer to mix, neglecting any temperature requirements for a reaction to take place.

A potentially new method for characterizing the puffing frequency of simulated reacting plumes through the heat release rate was discussed and compared to the subjective method of utilizing a probe of streamwise velocity at a point in space. While frequencies predicted via the heat release rate agreed well with theory and the frequencies predicted by the vertical velocities, additional studies would need to be carefully performed to validate this method.

Simulations in 3D are on-going for the case of fixed inflow composition of the eighteen species with the Skeletal-D model and utilizing infinitely-fast chemistry of the lumped fuel, $C_xH_yO_z$. These simulations will be compared to the puffing frequency relation based on the inflow diameter [75] and the predicted frequencies suggested by Wimer *et al.* based on the hydraulic diameter of the inflow geometry [39]. These simulations will also provide the best possible comparison in the line-of-sight average of gas-phase temperature and water mole fraction when comparing to the work of Makowiecki *et al.* at times near ignition [38]. A further goal is to integrate the work performed in this chapter into the computational framework described in Chapter 3 in which the solid and gas phases are connected.

*This chapter is comprised of material suitable for a publication that will be submitted to Combustion and Flame.*

# Chapter 5

# Conclusions and Future Work

*"The question is not how far. The question is, do you possess the constitution, the depth of faith, to go as far is as needed?"*

— Il Duce, *Troy Duffy, The Boondock Saints*

## 5.1 Summary of Work

The integration of finite-rate, multi-step and multi-specie chemical modeling into complex simulations with the goal of modeling meter-scale biomass pyrolysis, ignition and combustion has proved to be a difficult task. In this thesis, steps towards the lofty goal of fully integrated complex chemistry into a computational fluid dynamics simulation have been made in each the chapters. In the introduction, the following questions were posed as guides throughout this work, the subsequent summaries of each chapter will address these overarching questions.

- To what degree can the detailed, gas-phase, combustion kinetic models be reduced while still predicting bulk quantities (i.e., ignition delay time, laminar flame speed, heat release, etc.) and maintaining volatile species important to soot formation?
- Can multi-component/multi-specie pyrolysis and combustion kinetics be utilized in a single framework that consists of coupled solid and gas domains?
- Can highly reduced models (i.e., single-step, finite-rate chemistry or single-step, infinite-rate chemistry) be used to predict quantities of flaming biomass combustion?

Multiple new skeletal models of various fidelity were introduced in Chapter 2 based on the comprehensive biomass combustion mechanism of Ranzi *et al.*. The skeletal models were intimately linked to the pyrolysate composition of a biomass pyrolysis model of Debiagi *et al.* in order to determine the most important species in the combustion modeling. The resulting skeletal models, donned Skeletal-A, -B and -C, had quantifiable error, based on the errors in ignition delay time and peak temperature in a perfectly-stirred reactor, of 0.81%, 24.1% and 82.9%, respectively. Comparisons of each of the models and the detailed combustion mechanism were made with respect to ignition delay time, peak temperature and volumetric heat release rate in a perfectly-stirred reactor, the laminar flame speed in a one-dimensional premixed flame, and the maximum extinction temperature and strain rate for an opposed-jet diffusion flame. The newly developed models showed good agreement with the detailed model, for premixed and non-premixed combustion but required a simulation framework for the various effects of model reduction on the 3D combustion process to be studied.

In Chapter 3, the very simulation framework aforementioned was developed. Physics-based 3D simulations in OpenFOAM were performed to model the experiment performed by Makowiecki *et al.* of Douglas fir pyrolysis and combustion. The simulations utilized fireDyMFoam, developed by Lapointe, which is a derivative of fireFoam but includes adaptive mesh refinement (AMR) and dynamic load-rebalancing for more efficient parallel processing. In order to utilize the solid modeling capabilities of the fireFoam/fireDyMFoam framework, boundary conditions that captured the velocity, temperature and composition were developed. Specifically, the composition of the pyrolysate was calculated as a function of the biomass surface temperature *a priori*, the temperature of the solid included effects of direct radiation being applied, to model the cone calorimeter used in the experimental work. At the time of this work's publication, two pyrolysate species were utilized, namely water and methane by difference, and infinitely-fast chemistry was used. The simulations showed good agreement with mass loss (rate), surface temperature and gas-phase temperature for the pre- and post-ignition time-series but deviated from the post-ignition gas-phase water mole fraction experimental data. The discrepancy of these data point to the need for additional attention

to the composition and velocity boundary conditions. Infinitely-fast chemistry should over-predict water as it represents the theoretical maximum limit of complete combustion, thus the under-prediction of water directly correlates to an under-prediction of pyrolysate.

The incremental steps of Chapters 2 and 3 culminated in the material presented in Chapter 4, studying reacting buoyant plumes. Typically, the post-combustion mixture is approximated by a buoyant, non-reactive specie such as helium flowing into air. However, in this case, physics-based 2D simulations using fireFoam were performed that utilized the various skeletal models from Chapter 2, as well as a highly reduced model with 840% error and infinitely-fast chemistry of a lumped molecule that captured the thermodynamic state of the inflow composition. The inflow of the finite-rate simulations consisted of the eighteen pyrolysate species, predicted in Chapter 3 at a temperature representative of the post-ignition surface temperature. The inflow velocity was selected to mimic the diffusion/low-speed advection of species off a pyrolyzing surface. To achieve additional speed-up of the time required to complete the simulations, tabulated chemistry was utilized; which voided the use of dynamic rebalancing. The use of AMR can be utilized in the absence of the dynamic load balancing, however the AMR in fireDyMFoam is not designed for use in a 2D domain. Therefore, static, nested refinement was selected for resolving the nearly one meter domain down to two millimeters in the region of interest surrounding the inflow. Qualitative and quantitative comparisons of the four finite-rate cases with the skeletal models and the infinitely-fast case showed good agreement in the flow parameters and in the prediction of specie profiles, both vertically and horizontally - especially in the far-field. The discrepancies in ignition delay time and total heat release played the largest roles in changes of the results of the reacting plumes. Of particular note, the puffing frequency of the reacting buoyant plumes was characterized by the time-series of volume integrated heat release rate and agreed well with the empirical prediction published by Cetegen and Kasper for planar non-reacting plumes.

## 5.2 Future Research Directions

The skeletal models produced in Chapter 2 and utilized throughout this thesis were based on predicting the pyrolysis products and combustion of Douglas fir. While this specie of tree is predominantly found in the Front Range, a composition of different biomass species could be created. It would be interesting in attempting a skeletal reduction to create a more general reaction and to study how the chemical model changes as the input composition changes slightly. Furthermore, a sensitivity study of the various pyrolysate species would allow for simplifications to the pyrolysate composition, and further reduce the skeletal model derived from it. Recently, the python-based Model Automatic Reduction Software (pyMARS) [91] was released which utilizes purely open-source handling of the reduction through Cantera. This would allow for the addition of outer-loop optimization of various reduction parameters and conditions. It also allows for the pyrolysis kinetic solution to be solved for inside of the reduction loop, which could be packaged to run alongside OpenFOAM as a pre-processing step, or during run time.

The work in Chapter 3 represented the combination of cutting-edge experimental techniques and multi-phase computational simulations. Since the time of publication, additional experimental data was produced by Makowiecki *et al.* in an enclosed testing rig that is specifically rich for multi-specie pyrolysis model to attempt to model. These experiments were primarily comprised of pyrolysis experiments where species such as formaldehyde, methane, carbon monoxide, carbon dioxide, methanol and water were measured over thirty minute runs. In order to capture the pyrolysis gases, additional effort must be taken with respect to the temperature, velocity and composition boundary conditions utilized. Specifically, the use of mixed boundary conditions leads to a less combustible pyrolysate composition as nitrogen makes up any difference from a total mass/mole fraction of unity. Additionally, it would be important to include smouldering and soot modeling in the future to capture additional modes of combustion and particulate matter relevant to wildfire propagation and environmental concern.

The most recent work in Chapter 4 pushed the capabilities of fireDyMFoam, the incompati-

bilities of the solver with 2D simulations and dynamic load balancing with tabulated chemistry. The 2D compatibility should be able to be resolved by utilizing the built-in functionality of `extrudeMesh` after AMR adds cells in the third dimension. This represents an ineloquent solution, and likely would negate some of the cost-savings associated with using AMR. Tabulated chemistry utilizes information about chemical reactions that has previously been calculated and saved for later use. Dynamic load rebalancing is simply a reconstruction of the data followed by the decomposition of the latest time on the latest grid to allow for a more optimal distribution of cells per each processor. The OpenFOAM version of ISAT is not currently coded to be a reconstructed quantity, and in fact, may be as simple as collating and saving the tabulated binary tree results — this requires additional attention and study to verify.

While studying the literature on reacting plumes, specifically the work of Cetegen and Ahmed, the puffing frequency was mainly dependent on the characteristic length scale. However, in this work, the planar plume relation for a non-reacting plume showed good agreement with the simulated puffing frequency of the reacting plume. The relationship between the Strouhal and Richardson numbers for reacting versus a non-reacting plumes comes down to the density of the fluid of interest (i.e., the buoyant, non-reactive specie or the buoyant, products of combustion). Therefore, if all else is constant, the chemistry should not change the associated dynamical behavior from that predicted by a density-equivalent non-reacting buoyant plume. However, factors such as flame speed may change this relationship which would require additional study. The typical method of analyzing the puffing frequency of simulated plumes utilizes the choice of probing location, which introduces a subjective choice to capture a global instability. While the objective method of utilizing integrated heat release rate was introduced in Chapter 4, it would require additional simulations of various fuels, geometric configurations, Richardson and Strouhal numbers for validation.

Revisiting the work from Chapter 3 presented in Glusman *et al.* that predicted the water mole fraction at the surface and then considered the remainder of the pyrolysate to be methane, could be updated with the method of approximating thermodynamics by a lumped specie. This could be managed by analyzing the composition tables predicted as a function of temperature

to calculate the mixture-averaged quantities at the various temperatures and fitting the NASA polynomials in a similar fashion as described in Section 4.4.2.1 to simulate the composition, sans $CO_2$ and $H_2O$. This would allow for a better representation of the composition when compared to the method originally used, to use methane and water only. Additionally, non-unity Lewis number effects should be explored with the multi-component mixture of the pyrolysate.

## 5.3 On-going Work

Three simulations are currently underway but need to continue running before statistically converged, and are therefore not shown in the previous chapter. These are 3D runs of a pyrolyzing block with Skeletal-C combustion kinetics, and two reacting buoyant plumes with a 12×4 cm inlet using Skeletal-D and the lumped fuel specie with infinitely-fast chemistry. The temperature field of the combined solid and gaseous regions, that simulate the experiment in Chapter 3 with the eighteen pyrolysate species and use the custom boundary conditions, is shown in Figure 5.1. This simulation uses Skeletal-C to model the combustion kinetics and has only the initial ignition simulated. The reacting buoyant plume work of Chapter 4 has been extended to 3D with adaptive mesh refinement for use with Skeletal-D and the $C_xH_yO_z$ lumped specie with infinitely-fast chemistry.

## 5.4 Final Remarks

It is my hope that this work opens the door to future studies that use complex chemical models to understand the pyrolysis, ignition and combustion of lignocellulosic biomass. The intention behind the first two papers being published in an open-source journal is to allow the various skeletal models and OpenFOAM framework developed to be useful and widely, and freely, distributed to all. Happy OpenFOAMing!

*"All models are approximations. Essentially, all models are wrong, but some are useful."*

— George E. P. Box

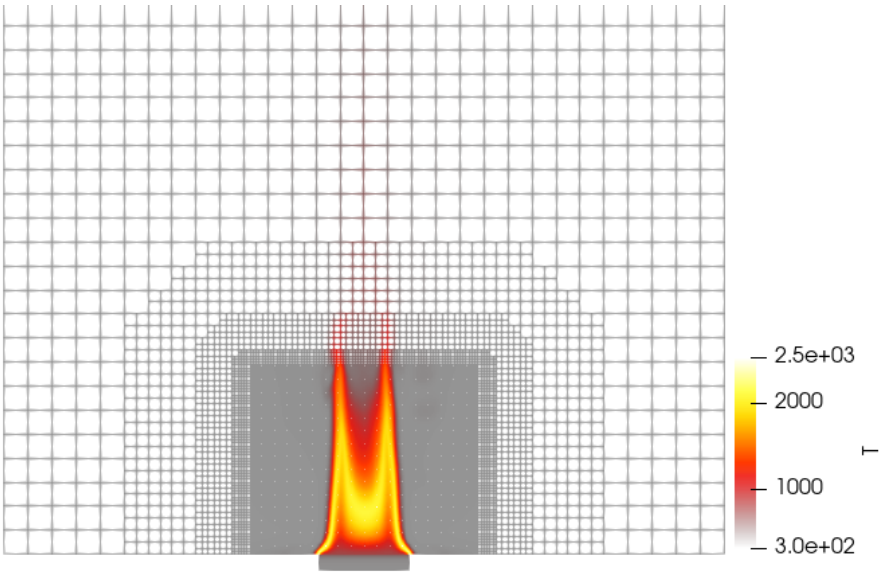


Figure 5.1: Temperature field with statically-refined mesh of pyrolyzing block of Douglas fir with Skeletal-C combustion model and eighteen pyrolysate species composition, in 3D.

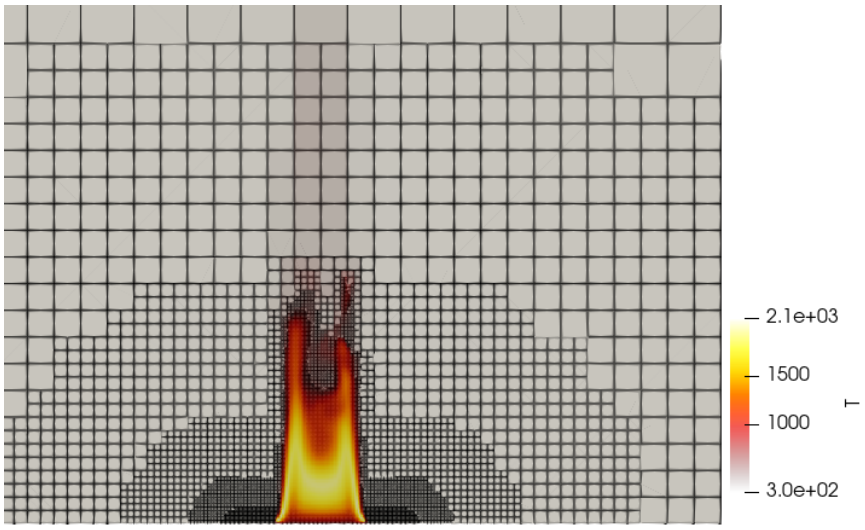


Figure 5.2: Temperature field with adaptive mesh refinement of fixed temperature and composition inflow of eighteen pyrolysate species and Skeletal-D combustion model, in 3D.

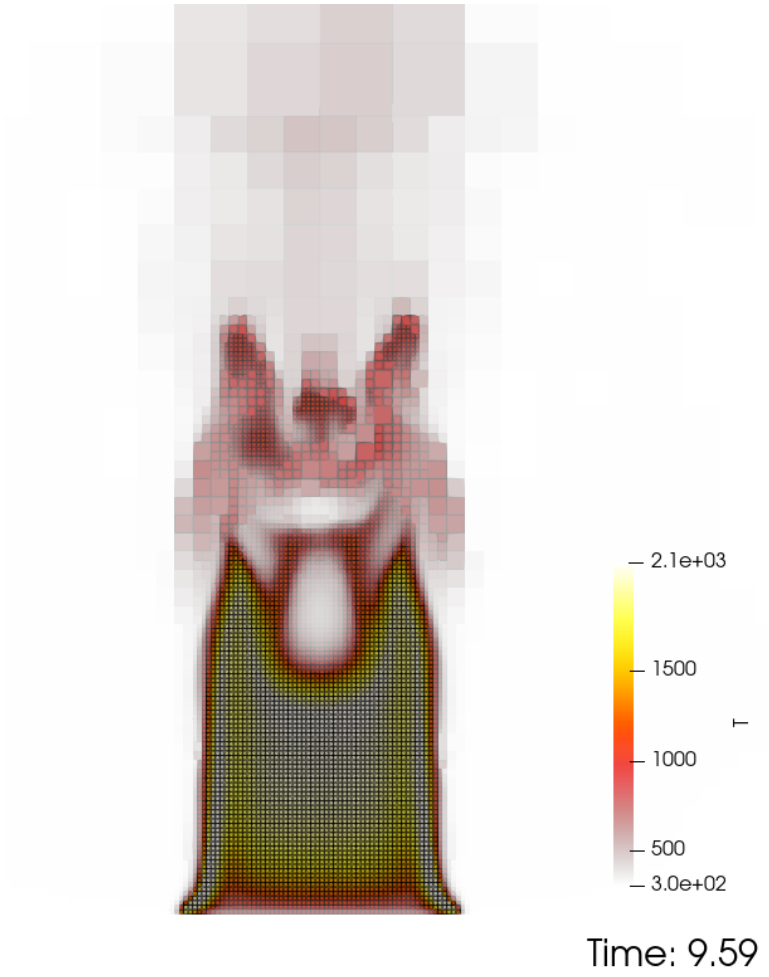


Figure 5.3: Temperature field with adaptive mesh refinement of fixed temperature and lumped fuel inflow of $C_xH_yO_z$ and infinitely-fast chemistry, in 3D.

## Bibliography


[1] National Interagency Fire Center (NIFC), Year-to-date Statistics 1983-2020, https://https://www.nifc.gov/fire-information/statistics/wildfires, (2021).

[2] A. L. Westerling, H. G. Hidalgo, D. R. Cayan, T. W. Swetnam, Warming and earlier spring increase western us forest wildfire activity, science 313 (2006) 940–943.

[3] Insurance Information Institute, Facts + statistics: Wildfires, https://www.iii.org/fact-statistic/facts-statistics-wildfires, (2021).

[4] H. Hanson, M. Bradley, J. Bossert, R. Linn, L. Younker, The potential and promise of physics-based wildfire simulation, Environmental Science & Policy 3 (2000) 161–172.

[5] A. Brown, M. Bruns, M. Gollner, J. Hewson, G. Maragkos, A. Marshall, R. McDermott, B. Merci, T. Rogaume, S. Stoliarov, J. Torero, A. Trouvé, Y. Wang, E. Weckman, Proceedings of the first workshop organized by the IAFSS Working Group on Measurement and Computation of Fire Phenomena (MaCFP), Fire Safety Journal 101 (2018) 1–17.

[6] M. A. Finney, FARSITE, Fire Area Simulator–model development and evaluation, 4, US Department of Agriculture, Forest Service, Rocky Mountain Research Station, (1998).

[7] J. L. Coen, M. Cameron, J. Michalakes, E. G. Patton, P. J. Riggan, K. M. Yedinak, Wrf-fire coupled weather–wildland fire modeling with the weather research and forecasting model, Journal of Applied Meteorology and Climatology 52 (2013) 16–38.

[8] R. Linn, J. Reisner, J. Colman, J. Winterkamp, Studying wildfire behavior using FIRETEC, Int. J. Wild. Fire 11 (2002) 233–246.

[9] A. L. Sullivan, Wildland surface fire spread modelling, 1990–2007. 1 physical and quasi-physical models, International Journal of Wildland Fire 18 (2009) 349–368.

[10] W. E. Mell, R. J. McDermott, G. P. Forney, Wildland fire behavior modeling perspectives, new approaches and applications, Proceedings of 3rd Fire Behavior and Fuels Conference, Spokane, Washington, USA, (2010).

[11] D. Morvan, Physical phenomena and length scales governing the behaviour of wildfires a case for physical modelling, Fire Technology 47 (2011) 437–460.

[12] R. Linn, J. Winterkamp, D. Weise, C. Edminster, A numerical study of slope and fuel structure effects on coupled wildlfire behavior, Int. J. Wild. Fire 19 (2010) 179–201.

[13] R. Barbero, J. Abatzoglou, N. Larkin, C. Kolden, B. Stocks, Climate change presents increased potential for very large fires in the contiguous united states, International Journal of Wildland Fire 24 (2015) 892–899.

[14] A. L. Westerling, Increasing western us forest wildfire activity sensitivity to changes in the timing of spring, Phil. Trans. R. Soc. B 371 (2016) 20150178.

[15] C. V. Barber, J. Schweithelm, Trial by fire, World Resources Institute, Washington, DC (2000).

[16] M. Keywood, M. Kanakidou, A. Stohl, F. Dentener, G. Grassi, C. Meyer, K. Torseth, D. Edwards, A. M. Thompson, U. Lohmann, *et al.*, Fire in the air: Biomass burning impacts in a changing climate, Critical Reviews in Environmental Science and Technology 43 (2013) 40–83.

[17] A. Demirbaş, Mechanisms of liquefaction and pyrolysis reactions of biomass, Energy conversion and management 41 (2000) 633–646.

[18] C. Di Blasi, Modeling chemical and physical processes of wood and biomass pyrolysis, Progress in energy and combustion science 34 (2008) 47–90.

[19] V. Vand, A theory of the irreversible electrical resistance changes of metallic films evaporated in vacuum, Proceedings of the Physical Society (1926-1948) 55 (1943) 222.

[20] J. Cai, W. Wu, R. Liu, An overview of distributed activation energy model and its application in the pyrolysis of lignocellulosic biomass, Renewable and Sustainable Energy Reviews 36 (2014) 236–246.

[21] S. Papari, K. Hawboldt, A review on the pyrolysis of woody biomass to bio-oil: Focus on kinetic models, Renewable and Sustainable Energy Reviews 52 (2015) 1580–1595.

[22] C. Lautenberger, Gpyro–a generalized pyrolysis model for combustible solids–users' guide, Version 0.700, February 19 (2009).

[23] C. Lautenberger, Gpyro3d: A three dimensional generalized pyrolysis model, Fire Safety Science 11 (2014) 193–207.

[24] W. Mell, A. Maranghides, R. McDermott, S. L. Manzello, Numerical simulation and experiments of burning douglas fir trees, Combustion and Flame 156 (2009) 2023–2041.

[25] K. McGrattan, S. Hostikka, R. McDermott, J. Floyd, C. Weinschenk, K. Overholt, Fire dynamics simulator user's guide, NIST special publication 1019 (2013).

[26] G. Gentile, P. E. A. Debiagi, A. Cuoci, A. Frassoldati, E. Ranzi, T. Faravelli, A computational framework for the pyrolysis of anisotropic biomass particles, Chemical Engineering Journal 321 (2017) 458–473.

[27] A. Cuoci, A. Frassoldati, T. Faravelli, E. Ranzi, A computational tool for the detailed kinetic modeling of laminar flames: Application to c2h4/ch4 coflow flames, Combustion and Flame 160 (2013) 870–886.

[28] J. E. Keeley, A. D. Syphard, Historical patterns of wildfire ignition sources in california ecosystems, International journal of wildland fire 27 (2018) 781–799.

[29] A. Fernandez-Pello, C. Lautenberger, D. Rich, C. Zak, J. Urban, R. Hadden, S. Scott, S. Fereres, Spot fire ignition of natural fuel beds by hot metal particles, embers, and sparks, Combustion science and technology 187 (2015) 269–295.

[30] M. Frenklach, H. Wang, C. Yu, M. Goldenberg, C. Bowman, R. Hanson, D. Davidson, E. Chang, G. Smith, D. Golden, *et al.*, Gri-mech-1.2, an optimized detailed chemical reaction mechanism for methane combustion, Gas Research Institute (1995).

[31] X. Zhou, S. Mahalingam, Evaluation of reduced mechanism for modeling combustion of pyrolysis gas in wildland fire, Combustion Science and Technology 171 (2001) 39–70.

[32] M. W. Jarvis, T. J. Haas, B. S. Donohoe, J. W. Daily, K. R. Gaston, W. J. Frederick, M. R. Nimlos, Elucidation of biomass pyrolysis products using a laminar entrained flow reactor and char particle imaging, Energy & Fuels 25 (2010) 324–336.

[33] C. K. Westbrook, F. L. Dryer, Chemical kinetic modeling of hydrocarbon combustion, Progress in energy and combustion science 10 (1984) 1–57.

[34] E. Ranzi, A. Cuoci, T. Faravelli, A. Frassoldati, G. Migliavacca, S. Pierucci, S. Sommariva, Chemical kinetics of biomass pyrolysis, Energy & Fuels 22 (2008) 4292–4300.

[35] The OpenFOAM Foundation, OpenFOAM Repository, `https://openfoam.org/`, (2019).

[36] C. Lapointe, N. T. Wimer, J. F. Glusman, A. S. Makowiecki, J. W. Daily, G. B. Rieker, P. E. Hamlington, Efficient simulation of turbulent diffusion flames in openfoam using adaptive mesh refinement, Fire Safety Journal 111 (2020) 102934.

[37] C. Lapointe, N. T. Wimer, S. Simons-Wellin, J. F. Glusman, G. B. Rieker, P. E. Hamlington, Efficient simulations of propagating flames and fire suppression optimization using adaptive mesh refinement, Fluids 6 (2021) 323.

[38] A. Makowiecki, J. Steinbrenner, N. Wimer, J. Glusman, C. Lapointe, J. Daily, P. Hamlington, G. Rieker, Dual frequency comb spectroscopy of solid fuel pyrolysis and combustion: Quantifying the influence of moisture content in douglas fir, Fire Safety Journal 116 (2020) 103185.

[39] N. T. Wimer, C. Lapointe, J. D. Christopher, S. P. Nigam, T. R. Hayden, A. Upadhye, M. Strobel, G. B. Rieker, P. E. Hamlington, Scaling of the puffing strouhal number for buoyant jets and plumes, Journal of Fluid Mechanics 895 (2020).

[40] N. T. Wimer, M. S. Day, C. Lapointe, M. A. Meehan, A. S. Makowiecki, J. F. Glusman, J. W. Daily, G. B. Rieker, P. E. Hamlington, Numerical simulations of buoyancy-driven flows using adaptive mesh refinement: structure and dynamics of a large-scale helium plume, Theoretical and Computational Fluid Dynamics 35 (2021) 61–91.

[41] C. B. Lapointe, Efficient Simulation of Complex Fire Phenomena in OpenFOAM using Adaptive Mesh Refinement, Ph.D. thesis, University of Colorado Boulder, (2020).

[42] J. F. Glusman, K. E. Niemeyer, A. S. Makoweicki, N. T. Wimer, C. B. Lapointe, G. B. Rieker, P. E. Hamlington, J. W. Daily, Reduced gas-phase kinetic models for burning of douglas fir, Frontiers in Mechanical Engineering 5 (2019).

[43] J. F. Glusman, C. B. Lapointe, A. S. Makoweicki, S. Simons-Wellin, G. B. Rieker, J. W. Daily, P. E. Hamlington, Validation of computationally efficient simulations of douglas fir pyrolysis and combustion using time-resolved frequency comb laser measurements, Frontiers in Forests and Global Change 5 (2022).

[44] A. S. Makowiecki, D. I. Herman, N. Hoghooghi, E. F. Strong, R. K. Cole, G. Ycas, F. R. Giorgetta, C. B. Lapointe, J. F. Glusman, J. W. Daily, P. E. Hamlington, N. R. Newbury, I. R. Coddington, G. B. Rieker, Mid-infrared dual frequency comb spectroscopy for combustion analysis from 2.8 to 5 $\mu$m, Proceedings of the Combustion Institute (2020).

[45] P. E. A. Debiagi, C. Pecchi, G. Gentile, A. Frassoldati, A. Cuoci, T. Faravelli, E. Ranzi, Extractives extend the applicability of multistep kinetic scheme of biomass pyrolysis, Energy & Fuels 29 (2015) 6544–6555.

[46] M. Corbetta, A. Frassoldati, H. Bennadji, K. Smith, M. J. Serapiglia, G. Gauthier, T. Melkior, E. Ranzi, E. M. Fisher, Pyrolysis of centimeter-scale woody biomass particles kinetic modeling and experimental validation, Energy & Fuels 28 (2014) 3884–3898.

[47] T. Faravelli, A. Frassoldati, G. Migliavacca, E. Ranzi, Detailed kinetic modeling of the thermal degradation of lignins, Biomass and Bioenergy 34 (2010) 290–301.

[48] K. Schwetz, A. Lipp, Ullmann's encyclopedia of industrial chemistry, VCH Deerfield Beach 28 (1985) 315.

[49] P. Schroeder, R. Wright, S. Coburn, B. Sodergren, K. Cossel, S. Droste, G. Truong, E. Baumann, F. Giorgetta, I. Coddington, N. Newbury, G. Rieker, Dual Frequency Comb Laser Absorption Spectroscopy in a 16 MW Gas Turbine Exhaust, Proceedings of the Combustion Institute 36 (2017) 4565–4573.

[50] E. Ranzi, M. Dente, A. Goldaniga, G. Bozzano, T. Faravelli, Lumping procedures in detailed kinetic modeling of gasification, pyrolysis, partial oxidation and combustion of hydrocarbon mixtures, Progress in Energy and Combustion Science 27 (2001) 99–139.

[51] K. E. Niemeyer, C.-J. Sung, M. P. Raju, Skeletal mechanism generation for surrogate fuels using directed relation graph with error propagation and sensitivity analysis, Combustion and Flame 157 (2010) 1760–1770.

[52] K. E. Niemeyer, C.-J. Sung, On the importance of graph search algorithms for drgep-based mechanism reduction methods, Combustion and Flame 158 (2011) 1439–1443.

[53] K. E. Niemeyer, C.-J. Sung, Mechanism reduction for multicomponent surrogates a case study using toluene reference fuels, Combustion and Flame 161 (2014) 2752–2764.

[54] K. E. Niemeyer, C.-J. Sung, Reduced chemistry for a gasoline surrogate valid at engine-relevant conditions, Energy & Fuels 29 (2015) 1172–1185.

[55] V. Hiremath, S. R. Lantz, H. Wang, S. B. Pope, Large-scale parallel simulations of turbulent combustion using combined dimension reduction and tabulation of chemistry, Proceedings of the Combustion Institute 34 (2013) 205–215.

[56] D. G. Goodwin, R. L. Speth, H. K. Moffat, B. W. Weber, Cantera an object-oriented software toolkit for chemical kinetics, thermodynamics, and transport processes, `https://cantera.org/`, (2018). Version 2.4.0.

[57] P. J. Schroeder, R. J. Wright, S. Coburn, B. Sodergren, K. C. Cossel, S. Droste, G. W. Truong, E. Baumann, F. R. Giorgetta, I. Coddington, *et al.*, Dual frequency comb laser absorption spectroscopy in a 16 mw gas turbine exhaust, Proceedings of the Combustion Institute 36 (2017) 4565–4573.

[58] I. Coddington, N. Newbury, W. Swann, Dual-comb spectroscopy, Optica 3 (2016) 414–426.

[59] Y. Wang, P. Chatterjee, J. de Ris, Large eddy simulation of fire plumes, Proceedings of the Combustion Institute 33 (2011) 2473–2480.

[60] K. Meredith, J. de Vries, Y. Wang, Y. Xin, A comprehensive model for simulating the interaction of water with solid surfaces in fire suppression environments, Proceedings of the Combustion Institute 34 (2013) 2719–2726.

[61] N. Ren, Y. Wang, S. Vilfayeau, A. Trouvé, Large eddy simulation of turbulent vertical wall fires supplied with gaseous fuel through porous burners, Combustion and Flame 169 (2016) 194–208.

[62] S. Vilfayeau, N. Ren, Y. Wang, A. Trouvé, Numerical simulation of under-ventilated liquid-fueled compartment fires with flame extinction and thermally-driven fuel evaporation, Proceedings of the Combustion Institute 35 (2015) 2563–2571.

[63] Y. Ding, C. Wang, S. Lu, Modeling the pyrolysis of wet wood using FireFOAM, Energy Conversion and Management 98 (2015) 500–506.

[64] K. Fukumoto, C. Wang, J. Wen, Large eddy simulation of upward flame spread on PMMA walls with a fully coupled fluid-solid approach, Combustion and flame 190 (2018) 365–387.

[65] M. Chaos, M. M. Khan, N. Krishnamoorthy, J. L. de Ris, S. B. Dorofeev, Evaluation of optimization schemes and determination of solid fuel properties for cfd fire models using bench-scale pyrolysis tests, Proceedings of the Combustion Institute 33 (2011) 2599–2606.

[66] A. Vinayak, Mathematical Modeling & Simulation of Pyrolysis & Flame Spread in OpenFOAM, Master's thesis, University of Wuppertal, (2017).

[67] G. Agarwal, M. Chaos, Y. Wang, Validation of pyrolysis model in transient heating scenarios and diverse spectral boundary conditions, Fire Safety Journal 120 (2021) 103064.

[68] W. Parker, Prediction of the heat release rate of douglas fir, Fire Safety Science 2 (1989) 337–346.

[69] K. Ragland, D. Aerts, A. Baker, Properties of wood for combustion analysis, Bioresource technology 37 (1991) 161–168.

[70] J. D. Christopher, N. T. Wimer, C. Lapointe, T. R. Hayden, I. Grooms, G. B. Rieker, P. E. Hamlington, Parameter estimation for complex thermal-fluid flows using approximate bayesian computation, Physical Review Fluids 3 (2018) 104602.

[71] M. A. Finney, J. D. Cohen, J. M. Forthofer, S. S. McAllister, M. J. Gollner, D. J. Gorham, K. Saito, N. K. Akafuah, B. A. Adam, J. D. English, Role of buoyant flame dynamics in wildfire spread, Proceedings of the National Academy of Sciences 112 (2015) 9833–9838.

[72] G. Hunt, T. Van den Bremer, Classical plume theory: 1937–2010 and beyond, IMA journal of applied mathematics 76 (2011) 424–448.

[73] B. M. Cetegen, K. D. Kasper, Experiments on the oscillatory behavior of buoyant plumes of helium and helium-air mixtures, Physics of fluids 8 (1996) 2974–2984.

[74] B. Cetegen, Y. Dong, M. Soteriou, Experiments on stability and oscillatory behavior of planar buoyant plumes, Physics of Fluids 10 (1998) 1658–1665.

[75] B. M. Cetegen, T. A. Ahmed, Experiments on the periodic instability of buoyant plumes and pool fires, Combustion and flame 93 (1993) 157–184.

[76] E. Weckman, A. Sobiesiak, The oscillatory behaviour of medium-scale pool fires, volume 22, Symposium (International) on Combustion, (1989).

[77] M. Sibulkin, A. G. Hansen, Experimental study of flame spreading over a horizontal fuel surface, Combustion Science and Technology 10 (1975) 85–92.

[78] A. Hamins, T. Kashiwagi, R. R. Buch, *et al.*, Characteristics of pool fire burning, ASTM special technical publication 1284 (1996) 15–41.

[79] G. Maragkos, B. Merci, Large eddy simulations of ch4 fire plumes, Flow, Turbulence and Combustion 99 (2017) 239–278.

[80] B. F. Magnussen, B. H. Hjertager, On mathematical modeling of turbulent combustion with special emphasis on soot formation and combustion, volume 16, Symposium (international) on Combustion, (1977).

[81] K. Luo, Instabilities, entrainment and mixing in reacting plumes, European Journal of Mechanics-B/Fluids 23 (2004) 443–460.

[82] X. Zhou, K. Luo, J. Williams, Vortex dynamics in spatio-temporal development of reacting plumes, Combustion and Flame 129 (2002) 11–29.

[83] S. B. Pope, Z. Ren, Efficient implementation of chemistry in computational combustion, Flow, turbulence and combustion 82 (2009) 437–453.

[84] T. Lu, C. K. Law, Toward accommodating realistic fuel chemistry in large-scale computations, Progress in Energy and Combustion Science 35 (2009) 192–215.

[85] B. Fiorina, D. Veynante, S. Candel, Modeling combustion chemistry in large eddy simulation of turbulent flames, Flow, Turbulence and Combustion 94 (2015) 3–42.

[86] S. B. Pope, Small scales, many species and the manifold challenges of turbulent combustion, Proceedings of the Combustion Institute 34 (2013) 1–31.

[87] R. Hilbert, F. Tap, H. El-Rabii, D. Thévenin, Impact of detailed chemistry and transport models on turbulent combustion simulations, Progress in Energy and Combustion Science 30 (2004) 61–117.

[88] M. Frenklach, K. Kailasanath, E. Oran, Systematic development of reduced reaction mechanisms for dynamic modeling, NASA Technical Report 19870046713 (1986).

[89] T. Turányi, Reduction of large reaction mechanisms, New Journal of Chemistry 14 (1990) 795–803.

[90] T. Turányi, Sensitivity analysis of complex kinetic systems. tools and applications, Journal of mathematical chemistry 5 (1990) 203–248.

[91] P. Mestas, P. Clayton, K. Niemeyer, pyMARS: automatically reducing chemical kinetic models in Python, Journal of Open Source Software 4 (2019) 1543.

[92] T. Lu, C. K. Law, A directed relation graph method for mechanism reduction, Proceedings of the Combustion Institute 30 (2005) 1333–1341.

[93] P. Pepiot-Desjardins, H. Pitsch, An efficient error-propagation-based reduction method for large chemical kinetic mechanisms, Combustion and Flame 154 (2008) 67–81.

[94] X. Zheng, T. Lu, C. Law, Experimental counterflow ignition temperatures and reaction mechanisms of 1, 3-butadiene, Proceedings of the Combustion Institute 31 (2007) 367–375.

[95] Y. Ra, R. D. Reitz, A reduced chemical kinetic model for ic engine combustion simulations with primary reference fuels, Combustion and Flame 155 (2008) 713–738.

[96] K. Manikantachari, L. Vesely, S. Martin, J. O. Bobren-Diaz, S. Vasu, Reduced chemical kinetic mechanisms for oxy/methane supercritical co2 combustor simulations, Journal of Energy Resources Technology 140 (2018).

[97] R. Lowe, A. Tomlin, Low-dimensional manifolds and reduced chemical models for tropospheric chemistry simulations, Atmospheric Environment 34 (2000) 2425–2436.

[98] B. Somers, The simulation of flat flames with detailed and reduced chemical models, Ph.D. thesis, Gastec NV NL, (1994).

[99] L. Pulga, G. Bianchi, S. Falfari, C. Forte, A machine learning methodology for improving the accuracy of laminar flame simulations with reduced chemical kinetics mechanisms, Combustion and Flame 216 (2020) 72–81.

[100] N. Zettervall, C. Fureby, E. J. Nilsson, Evaluation of chemical kinetic mechanisms for methane combustion: A review from a cfd perspective, Fuels 2 (2021) 210–240.

[101] A. Stagni, A. Frassoldati, A. Cuoci, T. Faravelli, E. Ranzi, Skeletal mechanism reduction through species-targeted sensitivity analysis, Combustion and Flame 163 (2016) 382–393.

[102] S. B. Pope, Computationally efficient implementation of combustion chemistry using in situ adaptive tabulation, Combustion Theory and Modelling (1997).

[103] L. Liang, J. G. Stevens, J. T. Farrell, A dynamic adaptive chemistry scheme for reactive flow computations, Proceedings of the Combustion Institute 32 (2009) 527–534.

[104] F. Contino, H. Jeanmart, T. Lucchini, G. D'Errico, Coupling of in situ adaptive tabulation and dynamic adaptive chemistry: An effective method for solving combustion in engine simulations, Proceedings of the Combustion Institute 33 (2011) 3057–3064.

[105] B. Tekgül, P. Peltonen, H. Kahila, O. Kaario, V. Vuorinen, Dlbfoam: An open-source dynamic load balancing model for fast reacting flow simulations in openfoam, Computer Physics Communications 267 (2021) 108073.

[106] K. E. Niemeyer, N. J. Curtis, C.-J. Sung, pyjac: Analytical jacobian generator for chemical kinetics, Computer Physics Communications 215 (2017) 188–203.

[107] I. Morev, B. Tekgül, M. Gadalla, A. Shahanaghi, J. Kannan, S. Karimkashi, O. Kaario, V. Vuorinen, Fast reactive flow simulations using analytical jacobian and dynamic load balancing in openfoam, Physics of Fluids 34 (2022) 021801.

[108] E. Anderson, Z. Bai, C. Bischof, L. S. Blackford, J. Demmel, J. Dongarra, J. Du Croz, A. Greenbaum, S. Hammarling, A. McKenney, *et al.*, LAPACK Users' guide, SIAM, (1999).

[109] M. Singer, S. Pope, Exploiting isat to solve the reaction–diffusion equation, Combustion theory and modelling 8 (2004) 361.

[110] S. Gordon, Computer program for calculation of complex chemical equilibrium compositions, rocket performance, incident and reflected shocks, and Chapman-Jouguet detonations, volume 273, Scientific and Technical Information Office, National Aeronautics and Space Administration, (1980).

[111] S. P. M. Bane, Spark ignition: experimental and numerical investigation with application to aviation safety, Ph.D. thesis, California Institute of Technology, (2010).

[112] B. Morton, G. I. Taylor, J. S. Turner, Turbulent gravitational convection from maintained and instantaneous sources, Proceedings of the Royal Society of London. Series A. Mathematical and Physical Sciences 234 (1956) 1–23.

[113] F. J. Diez, W. J. Dahm, Effects of heat release on turbulent shear flows. part 3. buoyancy effects due to heat release in jets and plumes, Journal of Fluid Mechanics 575 (2007) 221–255.

[114] P. Welch, The use of fast fourier transform for the estimation of power spectra: a method based on time averaging over short, modified periodograms, IEEE Transactions on audio and electroacoustics 15 (1967) 70–73.

[115] T. O'hern, E. Weckman, A. Gerhart, S. Tieszen, R. Schefer, Experimental study of a turbulent buoyant helium plume, Journal of Fluid Mechanics 544 (2005) 143–171.

[116] M. A. Meehan, N. T. Wimer, P. E. Hamlington, Richardson and Reynolds number effects on the near-field of buoyant plumes: Temporal variability and puffing, Journal of Fluid Mechanics (submitted 2022).

[117] A. F. Ghoniem, I. Lakkis, M. Soteriou, Numerical simulation of the dynamics of large fire plumes and the phenomenon of puffing, volume 26, Symposium (International) on Combustion, (1996).

# Appendix A

## Chemistry Models

Listing A.1: Multi-step Skeletal-D model in Cantera syntax

```
units(length='cm', time='s', quantity='mol', act_energy='cal/mol')
ideal_gas(name='gas',
         elements="C H Cl O N Ar He",
         species="""N2      O2       H2       H2O      H2O2
                   CO       CO2      CH2O     HCOOH    CH4
                   CH3OH    C2H2     C2H2O2   C2H4     C2H4O
                   CH3CHO   C2H4O2   C2H3CHO  C3H4O3   C3H6O
                   C5H4O2   CYC5H6   C6H5OH   C6H6O3   C6H8O4
                   C6H10O5  C8H10O3  C9H10O2  C11H12O4 O
                   H        OH       HO2      HCO      CH3
                   CH2OH    C2H3     CH3CO    CH2CHO   C2-QOOH""",
         reactions='all',
         transport='Mix',
         initial_state=state(temperature=300.0, pressure=OneAtm))
#-------------------------------------------------------------------------------
# Species data
#-------------------------------------------------------------------------------
species(name='N2',
       atoms='N:2',
       thermo=(NASA([300.00, 1050.00],
                  [ 3.85321336E+00, -2.44053349E-03, 5.35160392E-06,
                   -3.75608397E-09, 9.22684330E-13, -1.07969550E+03,
                    1.60217419E+00]),
               NASA([1050.00, 3500.00],
                  [ 2.71287897E+00, 1.90359754E-03, -8.54297556E-07,
                    1.84170938E-10, -1.54715988E-14, -8.40225273E+02,
                    7.15926558E+00])),
       transport=gas_transport(geom='linear',
                               diam=3.621,
                               well_depth=97.53,
                               polar=1.76,
                               rot_relax=4.0))
species(name='O2',
       atoms='O:2',
       thermo=(NASA([300.00, 760.00],
                  [ 3.46035080E+00, -8.85011121E-04, 5.15281056E-06,
                   -5.40712413E-09, 1.87809542E-12, -1.02942573E+03,
                    5.02236126E+00]),
               NASA([760.00, 3500.00],
                  [ 2.81750648E+00, 2.49838007E-03, -1.52493521E-06,
                    4.50547608E-10, -4.87702792E-14, -9.31713392E+02,
                    7.94729337E+00])),
       transport=gas_transport(geom='linear',
                               diam=3.458,
```

```
                            well_depth=107.4,
                            polar=1.6,
                            rot_relax=3.8))
species(name='H2',
       atoms='H:2',
       thermo=(NASA([300.00, 750.00],
                   [ 3.08866003E+00, 2.53968841E-03, -5.72992027E-06,
                     5.71701843E-09, -1.98865970E-12, -9.92148124E+02,
                    -2.43823459E+00]),
              NASA([750.00, 3500.00],
                   [ 3.73110902E+00, -8.86706214E-04, 1.12286897E-06,
                    -3.74349782E-10, 4.17963674E-14, -1.08851547E+03,
                    -5.35285855E+00])),
       transport=gas_transport(geom='linear',
                            diam=2.92,
                            well_depth=38.0,
                            polar=0.79,
                            rot_relax=280.0))
species(name='H2O',
       atoms='H:2 O:1',
       thermo=(NASA([300.00, 1590.00],
                   [ 4.03530937E+00, -6.87559833E-04, 2.86629214E-06,
                    -1.50552360E-09, 2.55006790E-13, -3.02783278E+04,
                    -1.99201641E-01]),
              NASA([1590.00, 3500.00],
                   [ 2.30940463E+00, 3.65433887E-03, -1.22983871E-06,
                     2.11931683E-10, -1.50333493E-14, -2.97294901E+04,
                     8.92765177E+00])),
       transport=gas_transport(geom='nonlinear',
                            diam=2.605,
                            well_depth=572.4,
                            dipole=1.844,
                            rot_relax=4.0))
species(name='H2O2',
       atoms='H:2 O:2',
       thermo=(NASA([300.00, 1180.00],
                   [ 2.91896355E+00, 9.92397296E-03, -8.56537418E-06,
                     4.23738723E-09, -8.61930485E-13, -1.76139998E+04,
                     8.76340177E+00]),
              NASA([1180.00, 3500.00],
                   [ 4.56163072E+00, 4.35560969E-03, -1.48694629E-06,
                     2.38275424E-10, -1.46610352E-14, -1.80016693E+04,
                     5.66597119E-01])),
       transport=gas_transport(geom='nonlinear',
                            diam=3.458,
                            well_depth=107.4,
                            rot_relax=3.8))
species(name='CO',
       atoms='C:1 O:1',
       thermo=(NASA([300.00, 1000.00],
                   [ 3.81890943E+00, -2.40697343E-03, 5.75226966E-06,
                    -4.28629830E-09, 1.11070419E-12, -1.43689533E+04,
                     2.49992060E+00]),
              NASA([1000.00, 3500.00],
                   [ 2.68595014E+00, 2.12486373E-03, -1.04548608E-06,
                     2.45538864E-10, -2.22550981E-14, -1.41423615E+04,
                     7.96579426E+00])),
       transport=gas_transport(geom='linear',
                            diam=3.65,
                            well_depth=98.1,
                            polar=1.95,
                            rot_relax=1.8))
species(name='CO2',
       atoms='C:1 O:2',
       thermo=(NASA([300.00, 1620.00],
```

```
                    [ 2.44892797E+00, 8.54596135E-03, -6.60570102E-06,
                      2.52769046E-09, -3.80099332E-13, -4.83922906E+04,
                      9.47557732E+00]),
                NASA([1620.00, 3500.00],
                    [ 5.07830985E+00, 2.05366041E-03, -5.94311265E-07,
                      5.38675131E-11, 1.66346855E-15, -4.92442103E+04,
                     -4.47815290E+00])),
        transport=gas_transport(geom='linear',
                                diam=3.763,
                                well_depth=244.0,
                                polar=2.65,
                                rot_relax=2.1))
species(name='CH2O',
        atoms='C:1 H:2 O:1',
        thermo=(NASA([300.00, 930.00],
                    [ 3.13463322E+00, 1.80037482E-03, 8.80336316E-06,
                     -8.92465077E-09, 2.63639286E-12, -1.50171301E+04,
                      7.57920580E+00]),
                NASA([930.00, 3500.00],
                    [ 1.06639253E+00, 1.06960337E-02, -5.54447373E-06,
                      1.36053696E-09, -1.28442554E-13, -1.46324373E+04,
                      1.74071779E+01])),
        transport=gas_transport(geom='nonlinear',
                                diam=3.59,
                                well_depth=498.0,
                                rot_relax=2.0))
species(name='HCOOH',
        atoms='C:1 H:2 O:2',
        thermo=(NASA([300.00, 1800.00],
                    [ 1.36256505E+00, 1.66938805E-02, -1.11828949E-05,
                      3.66178037E-09, -4.73930912E-13, -4.64539011E+04,
                      1.76174180E+01]),
                NASA([1800.00, 3500.00],
                    [ 5.80573302E+00, 6.82017393E-03, -2.95480608E-06,
                      6.14340060E-10, -5.06753135E-14, -4.80534416E+04,
                     -6.42993389E+00])),
        transport=gas_transport(geom='nonlinear',
                                diam=3.855,
                                well_depth=470.6,
                                rot_relax=1.0))
species(name='CH4',
        atoms='C:1 H:4',
        thermo=(NASA([300.00, 1070.00],
                    [ 2.85765313E+00, 2.53571100E-03, 9.67916346E-06,
                     -8.69880870E-09, 2.25599770E-12, -1.00357904E+04,
                      4.98969392E+00]),
                NASA([1070.00, 3500.00],
                    [-2.82321416E-01, 1.42739336E-02, -6.77628877E-06,
                      1.55380951E-09, -1.39473841E-13, -9.36383584E+03,
                      2.03507024E+01])),
        transport=gas_transport(geom='nonlinear',
                                diam=3.746,
                                well_depth=141.4,
                                polar=2.6,
                                rot_relax=13.0))
species(name='CH3OH',
        atoms='C:1 H:4 O:1',
        thermo=(NASA([300.00, 700.00],
                    [ 2.88895785E+00, 4.85657077E-03, 1.59348814E-05,
                     -2.08247943E-08, 7.94986176E-12, -2.53716460E+04,
                      1.03674509E+01]),
                NASA([700.00, 3500.00],
                    [ 9.34193000E-01, 1.60266556E-02, -8.00101466E-06,
                      1.97129714E-09, -1.91599484E-13, -2.50979789E+04,
                      1.91008457E+01])),
```

```
       transport=gas_transport(geom='nonlinear',
                               diam=3.626,
                               well_depth=481.8,
                               rot_relax=1.0))
species(name='C2H2',
       atoms='C:2 H:2',
       thermo=(NASA([300.00, 970.00],
                   [ 1.83812159E+00, 1.64533925E-02, -1.93408005E-05,
                     1.24068047E-08, -3.14627391E-12, 2.61425043E+04,
                     9.54239252E+00]),
               NASA([970.00, 3500.00],
                   [ 4.61193612E+00, 5.01498204E-03, -1.65253694E-06,
                     2.49922532E-10, -1.30568636E-14, 2.56043843E+04,
                    -3.75517096E+00])),
       transport=gas_transport(geom='linear',
                               diam=4.1,
                               well_depth=209.0,
                               rot_relax=2.5))
species(name='C2H2O2',
       atoms='C:2 H:2 O:2',
       thermo=(NASA([300.00, 1700.00],
                   [ 1.89947966E+00, 2.35363962E-02, -1.81616014E-05,
                     6.72307419E-09, -9.65107677E-13, -2.69305506E+04,
                     1.58338747E+01]),
               NASA([1700.00, 3500.00],
                   [ 9.83116579E+00, 4.87360532E-03, -1.69443300E-06,
                     2.65361078E-10, -1.54439841E-14, -2.96273239E+04,
                    -2.66407027E+01])),
       transport=gas_transport(geom='nonlinear',
                               diam=4.41,
                               well_depth=470.6,
                               rot_relax=1.5))
species(name='C2H4',
       atoms='C:2 H:4',
       thermo=(NASA([300.00, 1800.00],
                   [ 2.66161697E-01, 1.94272328E-02, -1.14541158E-05,
                     3.49691054E-09, -4.39228267E-13, 5.45399123E+03,
                     1.95264329E+01]),
               NASA([1800.00, 3500.00],
                   [ 4.49333672E+00, 1.00335105E-02, -3.62601388E-06,
                     5.97613541E-10, -3.65481279E-14, 3.93220822E+03,
                    -3.35192020E+00])),
       transport=gas_transport(geom='nonlinear',
                               diam=3.971,
                               well_depth=280.8,
                               rot_relax=1.5))
species(name='C2H4O',
       atoms='C:2 H:4 O:1',
       thermo=(NASA([300.00, 1440.00],
                   [-1.76683146E+00, 3.11247960E-02, -2.31168173E-05,
                     9.09246001E-09, -1.49102113E-12, -7.02731487E+03,
                     3.09356489E+01]),
               NASA([1440.00, 3500.00],
                   [ 4.77217531E+00, 1.29608883E-02, -4.19608017E-06,
                     3.32859470E-10, 2.97428516E-14, -8.91054882E+03,
                    -2.99568268E+00])),
       transport=gas_transport(geom='nonlinear',
                               diam=4.53,
                               well_depth=362.6,
                               rot_relax=1.5))
species(name='CH3CHO',
       atoms='C:2 H:4 O:1',
       thermo=(NASA([300.00, 1800.00],
                   [ 9.91751377E-01, 2.23500313E-02, -1.35975169E-05,
                     4.27666307E-09, -5.48877497E-13, -2.10792434E+04,
```

```
                    1.99667711E+01]),
             NASA([1800.00, 3500.00],
                  [ 6.27018126E+00, 1.06201871E-02, -3.82264672E-06,
                    6.56340789E-10, -4.60549581E-14, -2.29794782E+04,
                   -8.60119259E+00])),
       transport=gas_transport(geom='nonlinear',
                               diam=3.97,
                               well_depth=436.0,
                               rot_relax=2.0))
species(name='C2H4O2',
       atoms='C:2 H:4 O:2',
       thermo=(NASA([300.00, 770.00],
                  [ 4.64403525E+00, 1.38306802E-02, 2.18084389E-06,
                   -8.31108086E-09, 3.28100852E-12, -3.89966715E+04,
                    6.40833543E+00]),
             NASA([770.00, 3500.00],
                  [ 3.40614010E+00, 2.02613044E-02, -1.03463461E-05,
                    2.53497107E-09, -2.40436915E-13, -3.88060356E+04,
                    1.20569218E+01])),
       transport=gas_transport(geom='nonlinear',
                               diam=5.2,
                               well_depth=496.0,
                               rot_relax=1.0))
species(name='C2H3CHO',
       atoms='C:3 H:4 O:1',
       thermo=(NASA([300.00, 1340.00],
                  [ 3.40917666E-01, 3.51200360E-02, -2.88391725E-05,
                    1.22832633E-08, -2.12384107E-12, -1.16562372E+04,
                    2.26803642E+01]),
             NASA([1340.00, 3500.00],
                  [ 6.70517760E+00, 1.61222451E-02, -7.57298869E-06,
                    1.70307233E-09, -1.49924851E-13, -1.33618589E+04,
                   -9.88613663E+00])),
       transport=gas_transport(geom='nonlinear',
                               diam=4.12,
                               well_depth=443.2,
                               rot_relax=1.0))
species(name='C3H4O3',
       atoms='C:3 H:4 O:3',
       thermo=(NASA([300.00, 1710.00],
                  [ 2.17563103E+00, 3.78954970E-02, -2.73980784E-05,
                    9.81743159E-09, -1.38498288E-12, -5.38306424E+04,
                    2.19543274E+01]),
             NASA([1710.00, 3500.00],
                  [ 1.37242810E+01, 1.08811110E-02, -3.70124855E-06,
                    5.78901440E-10, -3.43205818E-14, -5.77802807E+04,
                   -3.99570073E+01])),
       transport=gas_transport(geom='nonlinear',
                               diam=4.662,
                               well_depth=435.2,
                               dipole=2.7,
                               rot_relax=1.0))
species(name='C3H6O',
       atoms='C:3 H:6 O:1',
       thermo=(NASA([300.00, 1720.00],
                  [-9.99780843E-02, 3.52621481E-02, -1.97932767E-05,
                    5.61555868E-09, -6.88932126E-13, -1.25581031E+04,
                    2.53116313E+01]),
             NASA([1720.00, 3500.00],
                  [ 6.42754902E+00, 2.00818525E-02, -6.55464685E-06,
                    4.84306793E-10, 5.68893699E-14, -1.48035725E+04,
                   -9.71995026E+00])),
       transport=gas_transport(geom='nonlinear',
                               diam=4.82,
                               well_depth=411.0,
```

```
                           rot_relax=1.0))
species(name='C5H4O2',
       atoms='C:5 H:4 O:2',
       thermo=(NASA([300.00, 1430.00],
                    [-1.81996644E+00, 5.68283325E-02, -4.71217197E-05,
                      1.94409629E-08, -3.18486782E-12, -1.98022652E+04,
                      3.45255921E+01]),
               NASA([1430.00, 3500.00],
                    [ 1.05158962E+01, 2.23224229E-02, -1.09267096E-05,
                      2.56683236E-09, -2.34844997E-13, -2.33303219E+04,
                     -2.94000374E+01])),
       transport=gas_transport(geom='nonlinear',
                           diam=5.653,
                           well_depth=524.69,
                           rot_relax=1.0))
species(name='CYC5H6',
       atoms='C:5 H:6',
       thermo=(NASA([300.00, 1020.00],
                    [-6.32922867E+00, 6.93993183E-02, -6.82623529E-05,
                      3.63968870E-08, -8.08274648E-12, 1.54866915E+04,
                      5.11475893E+01]),
               NASA([1020.00, 3500.00],
                    [ 1.70141558E+00, 3.79065957E-02, -2.19495256E-05,
                      6.12706526E-09, -6.63672518E-13, 1.38484401E+04,
                      1.22453451E+01])),
       transport=gas_transport(geom='nonlinear',
                           diam=5.2,
                           well_depth=408.0,
                           rot_relax=1.0))
species(name='C6H5OH',
       atoms='C:6 H:6 O:1',
       thermo=(NASA([300.00, 1330.00],
                    [-5.47325435E+00, 7.87541571E-02, -7.33732049E-05,
                      3.42982836E-08, -6.29384372E-12, -1.28778595E+04,
                      4.85843830E+01]),
               NASA([1330.00, 3500.00],
                    [ 1.39867712E+01, 2.02277643E-02, -7.36599500E-06,
                      1.21196288E-09, -7.46105018E-14, -1.80542263E+04,
                     -5.08485811E+01])),
       transport=gas_transport(geom='nonlinear',
                           diam=5.5,
                           well_depth=450.0,
                           rot_relax=1.0))
species(name='C6H6O3',
       atoms='C:6 H:6 O:3',
       thermo=(NASA([300.00, 1770.00],
                    [ 7.10718582E-01, 6.12173180E-02, -4.26352889E-05,
                      1.47094886E-08, -2.00094354E-12, -4.27462910E+04,
                      2.88889342E+01]),
               NASA([1770.00, 3500.00],
                    [ 1.98638073E+01, 1.79335016E-02, -5.95408859E-06,
                      8.93593939E-10, -4.95459880E-14, -4.95264845E+04,
                     -7.44496694E+01])),
       transport=gas_transport(geom='nonlinear',
                           diam=5.915,
                           well_depth=567.841,
                           rot_relax=1.0))
species(name='C6H8O4',
       atoms='C:6 H:8 O:4',
       thermo=(NASA([300.00, 1300.00],
                    [-4.55493836E+00, 1.00453147E-01, -9.00163533E-05,
                      4.10485358E-08, -7.47842033E-12, -7.25846463E+04,
                      5.20658817E+01]),
               NASA([1300.00, 3500.00],
                    [ 1.58073709E+01, 3.77998882E-02, -1.77241312E-05,
```

```
                     3.97560136E-09, -3.49009860E-13, -7.78788467E+04,
                    -5.15128322E+01])),
       transport=gas_transport(geom='nonlinear',
                               diam=5.23,
                               well_depth=568.5,
                               polar=10.3,
                               rot_relax=1.0))
species(name='C6H10O5',
       atoms='C:6 H:10 O:5',
       thermo=(NASA([300.00, 1220.00],
                    [-7.95116461E+00, 1.26488345E-01, -1.19085729E-04,
                      5.74579042E-08, -1.11165221E-11, -1.03461116E+05,
                      6.95642163E+01]),
               NASA([1220.00, 3500.00],
                    [ 1.54889718E+01, 4.96354387E-02, -2.45944509E-05,
                      5.82332585E-09, -5.35665863E-13, -1.09180509E+05,
                     -4.81819837E+01])),
       transport=gas_transport(geom='nonlinear',
                               diam=5.23,
                               well_depth=568.5,
                               polar=10.3,
                               rot_relax=1.0))
species(name='C8H10O3',
       atoms='C:8 H:10 O:3',
       thermo=(NASA([300.00, 1280.00],
                    [-3.09348688E+00, 1.50478421E-01, -1.41970521E-04,
                      6.75254832E-08, -1.26857982E-11, -6.17667016E+04,
                      4.61370519E+01]),
               NASA([1280.00, 3500.00],
                    [ 2.98957517E+01, 4.73870505E-02, -2.11603212E-05,
                      4.60350399E-09, -3.96349099E-13, -7.02119467E+04,
                     -1.21160681E+02])),
       transport=gas_transport(geom='nonlinear',
                               diam=5.64,
                               well_depth=621.1,
                               rot_relax=1.0))
species(name='C9H10O2',
       atoms='C:9 H:10 O:2',
       thermo=(NASA([300.00, 1620.00],
                    [-2.04331024E+00, 9.87327525E-02, -7.53682334E-05,
                      2.85512188E-08, -4.25270367E-12, -2.79267379E+04,
                      4.01996488E+01]),
               NASA([1620.00, 3500.00],
                    [ 2.64048781E+01, 2.84903123E-02, -1.03289369E-05,
                      1.78607618E-09, -1.22280426E-13, -3.71439509E+04,
                     -1.10770565E+02])),
       transport=gas_transport(geom='nonlinear',
                               diam=6.362,
                               well_depth=663.45,
                               rot_relax=1.0))
species(name='C11H12O4',
       atoms='C:11 H:12 O:4',
       thermo=(NASA([300.00, 1280.00],
                    [-3.09348688E+00, 1.50478421E-01, -1.41970521E-04,
                      6.75254832E-08, -1.26857982E-11, -6.17667016E+04,
                      4.61370519E+01]),
               NASA([1280.00, 3500.00],
                    [ 2.98957517E+01, 4.73870505E-02, -2.11603212E-05,
                      4.60350399E-09, -3.96349099E-13, -7.02119467E+04,
                     -1.21160681E+02])),
       transport=gas_transport(geom='nonlinear',
                               diam=6.362,
                               well_depth=663.45,
                               rot_relax=1.0))
species(name='O',
```

```
       atoms='O:1',
       thermo=(NASA([300.00, 950.00],
                    [ 2.95200330E+00, -1.68459131E-03, 2.55897854E-06,
                     -1.77574473E-09, 4.66034833E-13, 2.91471652E+04,
                      2.94136507E+00]),
               NASA([950.00, 3500.00],
                    [ 2.57318360E+00, -8.95609984E-05, 4.05096303E-08,
                     -8.39812674E-12, 9.43621991E-16, 2.92191409E+04,
                      4.74952023E+00])),
       transport=gas_transport(geom='atom',
                               diam=2.75,
                               well_depth=80.0))
species(name='H',
       atoms='H:1',
       thermo=(NASA([300.00, 1490.00],
                    [ 2.50000000E+00, -4.07455160E-15, 5.98527266E-18,
                     -3.43074982E-21, 6.74775716E-25, 2.54716200E+04,
                     -4.60117600E-01]),
               NASA([1490.00, 3500.00],
                    [ 2.50000000E+00, 7.40336223E-15, -5.56967416E-18,
                      1.73924876E-21, -1.92673709E-25, 2.54716200E+04,
                     -4.60117600E-01])),
       transport=gas_transport(geom='atom',
                               diam=2.05,
                               well_depth=145.0))
species(name='OH',
       atoms='H:1 O:1',
       thermo=(NASA([300.00, 880.00],
                    [ 3.37995109E+00, 6.13440526E-04, -1.06464235E-06,
                      1.14489214E-09, -3.76228211E-13, 3.45699735E+03,
                      2.70689352E+00]),
               NASA([880.00, 3500.00],
                    [ 3.62538436E+00, -5.02165281E-04, 8.36958463E-07,
                     -2.95714531E-10, 3.30350486E-14, 3.41380110E+03,
                      1.55419440E+00])),
       transport=gas_transport(geom='linear',
                               diam=2.75,
                               well_depth=80.0))
species(name='HO2',
       atoms='H:1 O:2',
       thermo=(NASA([300.00, 1540.00],
                    [ 2.85241381E+00, 5.40257188E-03, -3.80535043E-06,
                      1.51268170E-09, -2.40354212E-13, 4.47851086E+02,
                      9.84483831E+00]),
               NASA([1540.00, 3500.00],
                    [ 4.16318067E+00, 1.99798265E-03, -4.89192086E-07,
                      7.71153172E-11, -7.30772104E-15, 4.41348948E+01,
                      2.95517985E+00])),
       transport=gas_transport(geom='nonlinear',
                               diam=3.458,
                               well_depth=107.4,
                               rot_relax=1.0))
species(name='HCO',
       atoms='C:1 H:1 O:1',
       thermo=(NASA([300.00, 920.00],
                    [ 3.74218864E+00, 2.75844059E-05, 6.16298892E-06,
                     -5.89177898E-09, 1.73431136E-12, 4.07330951E+03,
                      5.45007090E+00]),
               NASA([920.00, 3500.00],
                    [ 2.44772078E+00, 5.65570555E-03, -3.01329556E-06,
                      7.57702524E-10, -7.26129631E-14, 4.31149160E+03,
                      1.15871953E+01])),
       transport=gas_transport(geom='nonlinear',
                               diam=3.59,
                               well_depth=498.0))
```

```
species(name='CH3',
       atoms='C:1 H:3',
       thermo=(NASA([300.00, 1270.00],
                    [ 3.53327401E+00, 3.61488008E-03, 1.00739068E-06,
                     -1.39958516E-09, 3.34014277E-13, 1.63060366E+04,
                      2.10113860E+00]),
               NASA([1270.00, 3500.00],
                    [ 2.57723974E+00, 6.62601164E-03, -2.54906392E-06,
                      4.67320141E-10, -3.34867663E-14, 1.65488693E+04,
                      6.94195966E+00])),
       transport=gas_transport(geom='linear',
                               diam=3.8,
                               well_depth=144.0))
species(name='CH2OH',
       atoms='C:1 H:3 O:1',
       thermo=(NASA([300.00, 1590.00],
                    [ 1.95857131E+00, 1.56199253E-02, -1.23601148E-05,
                      5.06183022E-09, -8.13124769E-13, -3.25268877E+03,
                      1.43100973E+01]),
               NASA([1590.00, 3500.00],
                    [ 7.61004151E+00, 1.40239019E-03, 1.05265418E-06,
                     -5.61972284E-10, 7.11209072E-14, -5.04985629E+03,
                     -1.55757586E+01])),
       transport=gas_transport(geom='nonlinear',
                               diam=3.69,
                               well_depth=417.0,
                               dipole=1.7,
                               rot_relax=2.0))
species(name='C2H3',
       atoms='C:2 H:3',
       thermo=(NASA([300.00, 700.00],
                    [ 2.74606708E+00, 3.71341276E-03, 1.60736225E-05,
                     -2.12880236E-08, 8.22995002E-12, 3.33332148E+04,
                      1.05346375E+01]),
               NASA([700.00, 3500.00],
                    [ 7.05094230E-01, 1.53761148E-02, -8.91788178E-06,
                      2.51340905E-09, -2.70561650E-13, 3.36189510E+04,
                      1.96531878E+01])),
       transport=gas_transport(geom='nonlinear',
                               diam=4.1,
                               well_depth=209.0,
                               rot_relax=1.0))
species(name='CH3CO',
       atoms='C:2 H:3 O:1',
       thermo=(NASA([300.00, 1800.00],
                    [ 1.83189171E+00, 1.73119663E-02, -1.03948404E-05,
                      3.22021171E-09, -4.07592723E-13, -3.96477680E+03,
                      1.68993055E+01]),
               NASA([1800.00, 3500.00],
                    [ 5.59449005E+00, 8.95063669E-03, -3.42706569E-06,
                      6.39554414E-10, -4.91680987E-14, -5.31931220E+03,
                     -3.46466160E+00])),
       transport=gas_transport(geom='nonlinear',
                               diam=3.97,
                               well_depth=436.0,
                               rot_relax=2.0))
species(name='CH2CHO',
       atoms='C:2 H:3 O:1',
       thermo=(NASA([300.00, 1030.00],
                    [ 2.15742069E-01, 2.78720987E-02, -2.67403448E-05,
                      1.43321353E-08, -3.22098924E-12, 6.73694406E+02,
                      2.26661724E+01]),
               NASA([1030.00, 3500.00],
                    [ 3.66502520E+00, 1.44768244E-02, -7.23266377E-06,
                      1.70580456E-09, -1.56345856E-13, -3.68579193E+01,
```

```
                    5.92341850E+00])),
       transport=gas_transport(geom='nonlinear',
                               diam=3.97,
                               well_depth=436.0,
                               rot_relax=2.0))
species(name='C2-QOOH',
       atoms='C:2 H:5 O:2',
       thermo=(NASA([300.00, 1270.00],
                  [ 8.24295798E-01, 3.89409231E-02, -3.39574000E-05,
                    1.54707291E-08, -2.85531058E-12, 2.50651957E+03,
                    2.49202290E+01]),
               NASA([1270.00, 3500.00],
                  [ 7.85685775E+00, 1.67911217E-02, -7.79621720E-06,
                    1.73782470E-09, -1.51982948E-13, 7.20248835E+02,
                   -1.06887184E+01])),
       transport=gas_transport(geom='nonlinear',
                               diam=4.41,
                               well_depth=470.6,
                               rot_relax=1.5))
#-------------------------------------------------------------------------------
# Reaction data
#-------------------------------------------------------------------------------
# Reaction 1
reaction('H + O2 <=> OH + O', [9.600000e+14, -0.2, 16625.0])
# Reaction 2
reaction('O + H2 <=> OH + H', [4.330000e+13, 0.0, 10000.0])
# Reaction 3
falloff_reaction('H + O2 (+ M) <=> HO2 (+ M)',
               kf=[5.580000e+12, 0.4, 0.0],
               kf0=[8.400000e+17, -0.8, 0.0],
               efficiencies='CO:1.2 CO2:2.4 H2:2.5 H2O:18.0 N2:1.26',
               falloff=Troe(A=0.5, T3=1e-30, T1=1e+30))
# Reaction 4
reaction('OH + HO2 <=> H2O + O2', [5.000000e+13, 0.0, 1000.0])
# Reaction 5
reaction('H + HO2 <=> OH + OH', [2.500000e+14, 0.0, 1900.0])
# Reaction 6
reaction('OH + OH <=> O + H2O', [3.570000e+04, 2.4, -2110.0])
# Reaction 7
three_body_reaction('H + OH + M <=> H2O + M', [4.500000e+22, -2.0, 0.0],
                  efficiencies='CO2:1.9 H2:2.0 H2O:16.0')
# Reaction 8
reaction('H + HO2 <=> H2 + O2', [2.500000e+13, 0.0, 700.0])
# Reaction 9
reaction('HO2 + HO2 <=> H2O2 + O2', [2.110000e+12, 0.0, 0.0])
# Reaction 10
falloff_reaction('OH + OH (+ M) <=> H2O2 (+ M)',
               kf=[7.400000e+13, -0.37, 0.0],
               kf0=[1.300000e+18, -0.9, -1700.0],
               efficiencies='CH4:2.0 CO:1.5 CO2:2.0 H2:2.0 H2O:6.0 N2:0.9',
               falloff=Troe(A=0.7346, T3=94.0, T1=1756.0, T2=5182.0))
# Reaction 11
three_body_reaction('O + OH + M <=> HO2 + M', [1.000000e+16, 0.0, 0.0])
# Reaction 12
reaction('O2 + HCO <=> HO2 + CO', [3.000000e+12, 0.0, 0.0])
# Reaction 13
reaction('CO + OH <=> CO2 + H', [9.600000e+11, 0.14, 7352.0],
        options='duplicate')
# Reaction 14
reaction('CO + OH <=> CO2 + H', [7.320000e+10, 0.03, -16.0],
        options='duplicate')
# Reaction 15
falloff_reaction('H + CH3 (+ M) <=> CH4 (+ M)',
               kf=[1.200000e+15, -0.4, 0.0],
               kf0=[6.400000e+23, -1.8, 0.0],
```

```
               efficiencies='CO:2.0 CO2:3.0 H2:2.0 H2O:5.0',
               falloff=SRI(A=0.45, B=797.0, C=979.0))
# Reaction 16
falloff_reaction('C2H2 + H (+ M) <=> C2H3 (+ M)',
               kf=[1.000000e+13, 0.0, 2770.0],
               kf0=[3.900000e+16, 0.0, -560.0],
               efficiencies='CO:2.0 CO2:3.0 H2:2.0 H2O:5.0')
# Reaction 17
falloff_reaction('CH3OH (+ M) <=> CH3 + OH (+ M)',
               kf=[7.000000e+20, -1.3, 92000.0],
               kf0=[1.250000e+14, 0.85, 67000.0])
# Reaction 18
reaction('CH3CHO <=> CH3 + HCO', [1.500000e+16, 0.0, 85000.0])
# Reaction 19
reaction('O2 + CH4 <=> HO2 + CH3', [9.000000e+13, 0.0, 56000.0])
# Reaction 20
three_body_reaction('HCO + M <=> CO + H + M', [1.200000e+17, -1.0, 17000.0],
                  efficiencies='CH4:2.8 CO:1.9 CO2:3.0 H2:1.9 H2O:5.0')
# Reaction 21
three_body_reaction('CH2OH + M <=> H + CH2O + M', [3.750000e+14, 0.0, 25000.0])
# Reaction 22
three_body_reaction('CH3CO + M <=> CH3 + CO + M', [2.500000e+15, 0.0, 14400.0])
# Reaction 23
reaction('O + C2H4 <=> CH3 + HCO', [5.000000e+06, 1.88, 200.0])
# Reaction 24
reaction('O2 + CH2OH <=> HO2 + CH2O', [6.000000e+12, 0.0, 0.0])
# Reaction 25
reaction('O2 + C2H3 <=> O + CH2CHO', [7.500000e+14, -0.61, 5260.0])
# Reaction 26
reaction('O2 + C2H3 <=> C2H2 + HO2', [6.000000e+09, 0.0, 0.0])
# Reaction 27
reaction('O2 + CH2CHO => CH2O + OH + CO', [6.000000e+10, 0.0, 0.0])
# Reaction 28
reaction('OH + CH3 <=> CH2OH + H', [1.100000e+13, 0.0, 6300.0])
# Reaction 29
reaction('OH + CH3 <=> CH2O + H2', [6.000000e+12, 0.0, 0.0])
# Reaction 30
reaction('OH + CH3 <=> O + CH4', [2.000000e+12, 0.0, 8000.0])
# Reaction 31
reaction('HCO + HO2 => H + OH + CO2', [3.000000e+13, 0.0, 0.0])
# Reaction 32
reaction('HCO + CH3 <=> CO + CH4', [1.000000e+13, 0.0, 0.0])
# Reaction 33
reaction('CH2CHO + H => CH3CHO', [6.000000e+13, 0.0, 0.0])
# Reaction 34
reaction('CH2CHO <=> CH3CO', [2.000000e+11, 0.0, 32000.0])
# Reaction 35
reaction('O + C2H4 => CH2CHO + H', [1.000000e+13, 0.0, 3000.0])
# Reaction 36
reaction('OH + C2H2 => CH2CHO', [5.000000e+11, 0.0, 0.0])
# Reaction 37
reaction('OH + C2H4 <=> H2O + C2H3', [2.000000e+13, 0.0, 6000.0])
# Reaction 38
reaction('H + CH2O <=> H2 + HCO', [4.500000e+14, 0.0, 7500.0])
# Reaction 39
reaction('H + CH3CHO <=> H2 + CH3CO', [4.500000e+14, 0.0, 7500.0])
# Reaction 40
reaction('H + H2O <=> H2 + OH', [4.800000e+10, 1.0, 19000.0])
# Reaction 41
reaction('H2O2 + H <=> H2 + HO2', [6.025000e+13, 0.0, 7950.0])
# Reaction 42
reaction('OH + CH3OH => H2O + CH2OH', [9.200000e+04, 2.53, -1000.0])
# Reaction 43
reaction('HO2 + CH3OH => H2O2 + CH2OH', [8.000000e+13, 0.0, 19400.0])
# Reaction 44
```

```
reaction('OH + CYC5H6 => HCO + C2H2 + C2H4', [2.000000e+12, 0.0, 0.0])
# Reaction 45
reaction('C2-QOOH => C2H4 + HO2', [1.500000e+13, 0.0, 24000.0])
# Reaction 46
reaction('HO2 + C2H4 => C2-QOOH', [5.000000e+11, 0.0, 14000.0])
# Reaction 47
reaction('C2-QOOH => OH + C2H4O', [8.000000e+10, 0.0, 18000.0])
# Reaction 48
reaction('C2H4O => CH3 + HCO', [1.000000e+17, 0.0, 71000.0])
# Reaction 49
reaction('C2H4O <=> CH3CHO', [6.000000e+16, 0.0, 69000.0])
# Reaction 50
reaction('C3H6O => CH2CHO + CH3', [5.000000e+16, 0.0, 73000.0])
# Reaction 51
reaction('C3H6O => C2H4 + CH2O', [1.000000e+16, 0.0, 64000.0])
# Reaction 52
reaction('C2H4O2 <=> CH2OH + HCO', [1.000000e+16, 0.0, 82000.0])
# Reaction 53
reaction('C2H4O2 <=> CH2O + CH2O', [5.000000e+12, 0.0, 60000.0])
# Reaction 54
reaction('OH + C2H3CHO => CH3 + C2H2O2', [1.000000e+12, 0.0, 0.0])
# Reaction 55
reaction('C2H2O2 <=> HCO + HCO', [3.000000e+16, 0.0, 71000.0])
# Reaction 56
reaction('C3H4O3 => HCO + C2H2O2 + H', [1.000000e+16, 0.0, 77000.0])
# Reaction 57
reaction('C6H6O3 => C5H4O2 + H + HCO', [2.000000e+16, 0.0, 79000.0])
# Reaction 58
reaction('C6H6O3 <=> CH2O + C5H4O2', [5.000000e+12, 0.0, 59000.0])
# Reaction 59
reaction('C6H10O5 => C2H4O2 + C2H3CHO + OH + HCO', [2.500000e+16, 0.0, 85000.0])
# Reaction 60
reaction('C6H10O5 => C6H6O3 + H2O + H2O', [1.000000e+14, 0.0, 65000.0])
# Reaction 61
reaction('C6H10O5 => C6H8O4 + H2O', [1.000000e+14, 0.0, 65000.0])
# Reaction 62
reaction('C6H8O4 => C6H6O3 + H2O', [1.000000e+14, 0.0, 65000.0])
# Reaction 63
reaction('C11H12O4 => C8H10O3 + CO + C2H2', [7.000000e+15, 0.0, 88000.0])
# Reaction 64
reaction('H + C11H12O4 => C2H3 + CO + C8H10O3', [1.000000e+13, 0.0, 5000.0])
# Reaction 65
reaction('C2H3CHO => HCO + C2H3', [3.000000e+16, 0.0, 90000.0])
# Reaction 66
reaction('OH + C2H3CHO => CH3CHO + HCO', [4.000000e+12, 0.0, 0.0])
# Reaction 67
reaction('OH + C2H3CHO => CO2 + C2H4 + H', [1.100000e+13, 0.0, 0.0])
# Reaction 68
reaction('HCO + C2H3 => C2H3CHO', [4.000000e+12, 0.0, 0.0])
# Reaction 69
reaction('C6H5OH <=> CYC5H6 + CO', [2.500000e+13, 0.0, 72400.0])
# Reaction 70
reaction('OH + C6H5OH => OH + CYC5H6 + CO', [4.000000e+12, 0.0, 0.0])
# Reaction 71
reaction('HCOOH <=> CO + H2O', [9.000000e+13, 0.0, 65300.0])
# Reaction 72
reaction('HCOOH <=> CO2 + H2', [7.000000e+12, 0.0, 64700.0])
# Reaction 73
reaction('OH + CH4 => H2O + CH3', [2.796000e+06, 2.0, 1566.11])
# Reaction 74
reaction('H + C2H4 => H2 + C2H3', [1.925000e+07, 2.0, 10409.77])
# Reaction 75
reaction('CH3 + H2O => CH4 + OH', [3.903000e+05, 2.0, 15366.11])
# Reaction 76
reaction('OH + CH2O => H2O + HCO', [3.195000e+06, 2.0, -2065.87])
```

```
# Reaction 77
reaction('CH3 + CH2O => CH4 + HCO', [3.122000e+05, 2.0, 3781.38])
# Reaction 78
reaction('OH + CH3CHO => H2O + CH3CO', [2.396000e+06, 2.0, -1734.99])
# Reaction 79
reaction('OH + C2H4O => H2O + CH2CHO', [1.598000e+06, 2.0, -1174.58])
# Reaction 80
reaction('OH + C2H4O2 => H2O + CO + CH2OH', [1.598000e+06, 2.0, -3343.83])
# Reaction 81
reaction('OH + C2H2O2 => H2O + CO + HCO', [3.195000e+06, 2.0, -3343.83])
# Reaction 82
reaction('OH + C3H4O3 => H2O + CO + C2H2O2 + H', [3.195000e+06, 2.0, -3343.83])
# Reaction 83
reaction('OH + C6H6O3 => H2O + C5H4O2 + CO + H', [1.598000e+06, 2.0, -3343.83])
# Reaction 84
reaction('O + C6H6O3 => OH + C5H4O2 + CO + H', [5.413000e+06, 2.0, 1094.46])
# Reaction 85
reaction('OH + C6H10O5 => H2O + CH2O + CH2CHO + C3H4O3', [1.598000e+06, 2.0, -2259.83])
# Reaction 86
reaction('OH + C6H10O5 => H2O + C6H8O4 + OH', [1.997000e+05, 2.0, -2259.83])
# Reaction 87
reaction('OH + C6H8O4 => H2O + C6H6O3 + OH', [3.994000e+05, 2.0, -2259.83])
# Reaction 88
reaction('OH + C3H6O => H2O + C2H3CHO + H', [5.991000e+05, 2.0, -2259.83])
# Reaction 89
reaction('OH + HCOOH => H2O + CO + OH', [1.997000e+05, 2.0, -474.43])
```

Listing A.2: Infinitely-fast $C_xH_yO_z$ model in OpenFOAM syntax

```
species
(
    O2
    H2O
    FUEL1
    CO2
    N2
);

reactions
{
    CxHyOzReaction
    {
        type        irreversibleinfiniteReaction;
        reaction     "FUEL1 + 2.12875O2 + 8.0041N2 = 1.961CO2 + 1.5375H2O + 8.0041N2";
    }
}
```

Listing A.3: Infinitely-fast $C_xH_yO_z$ thermodynamics and transport in OpenFOAM syntax

```
FUEL1
{
    specie
    {
        molWeight     45.8404;
    }
    thermodynamics
    {
        Tlow          250;
        Thigh         3500;
        Tcommon       1590;
        highCpCoeffs  ( 4.5677358877 0.014570647 -5.4103173e-06 -1.643080445e-09
            1.3936236e-12 -2.7436727e+03 0.6217895);
        lowCpCoeffs   ( 4.5677358877 0.014570647 -5.4103173e-06 -1.643080445e-09
            1.3936236e-12 -2.7436727e+03 0.6217895);
    }
    transport
    {
        As            1.67212e-06;
        Ts            170.672;
    }
    elements
    {
        C             1.961;
        H             3.075;
        O             1.202;
    }
}
```

# Appendix B

## Time-series of Ignition for Skeletal-A, Skeletal-B and Skeletal-C

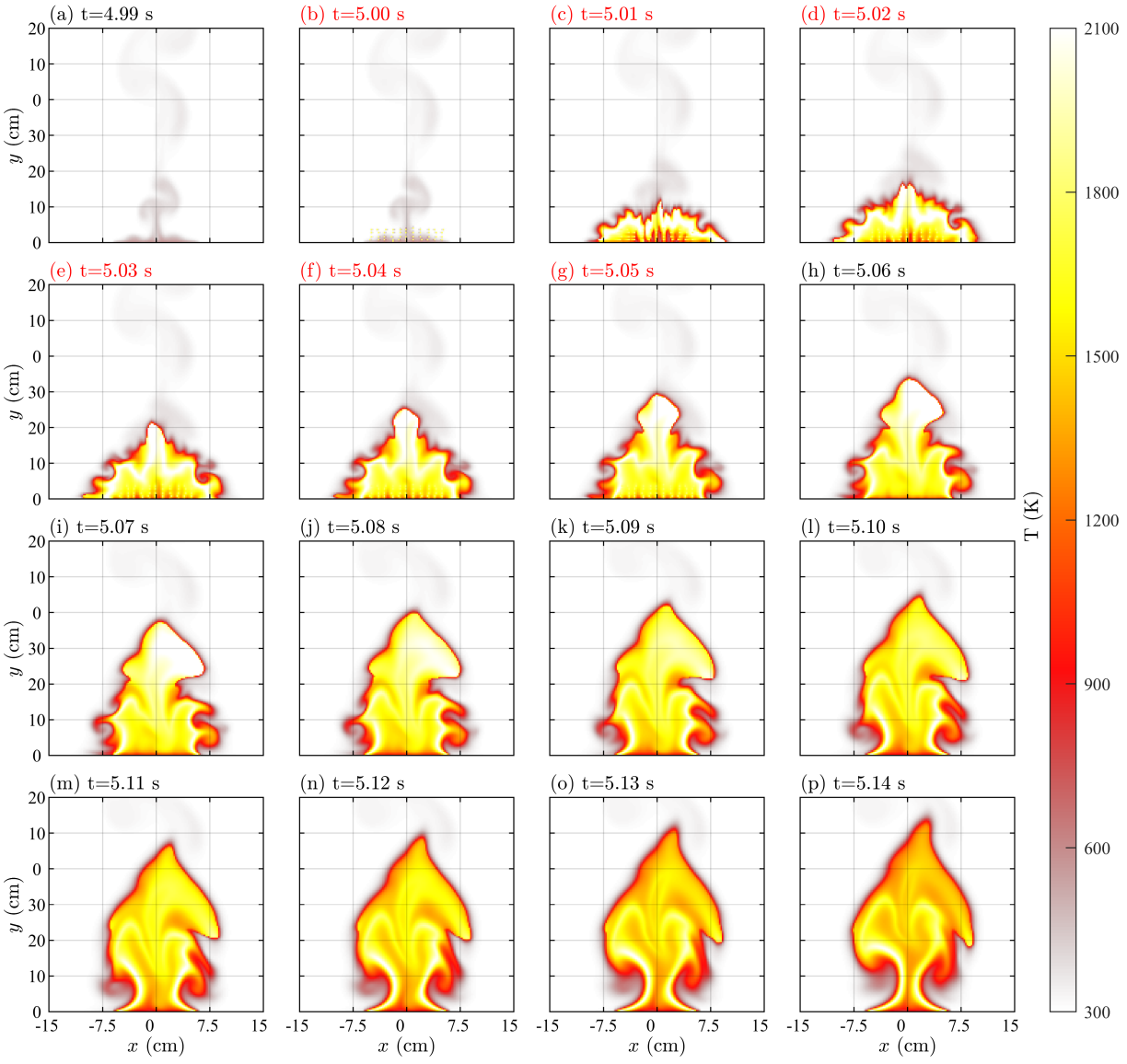


Figure B.1: Time-series of temperature during ignition with Skeletal-A model, with 0.05 s spark beginning at $t = 5$ s. Time labels written in red indicate when the simulation is under-going the "sparking" process.

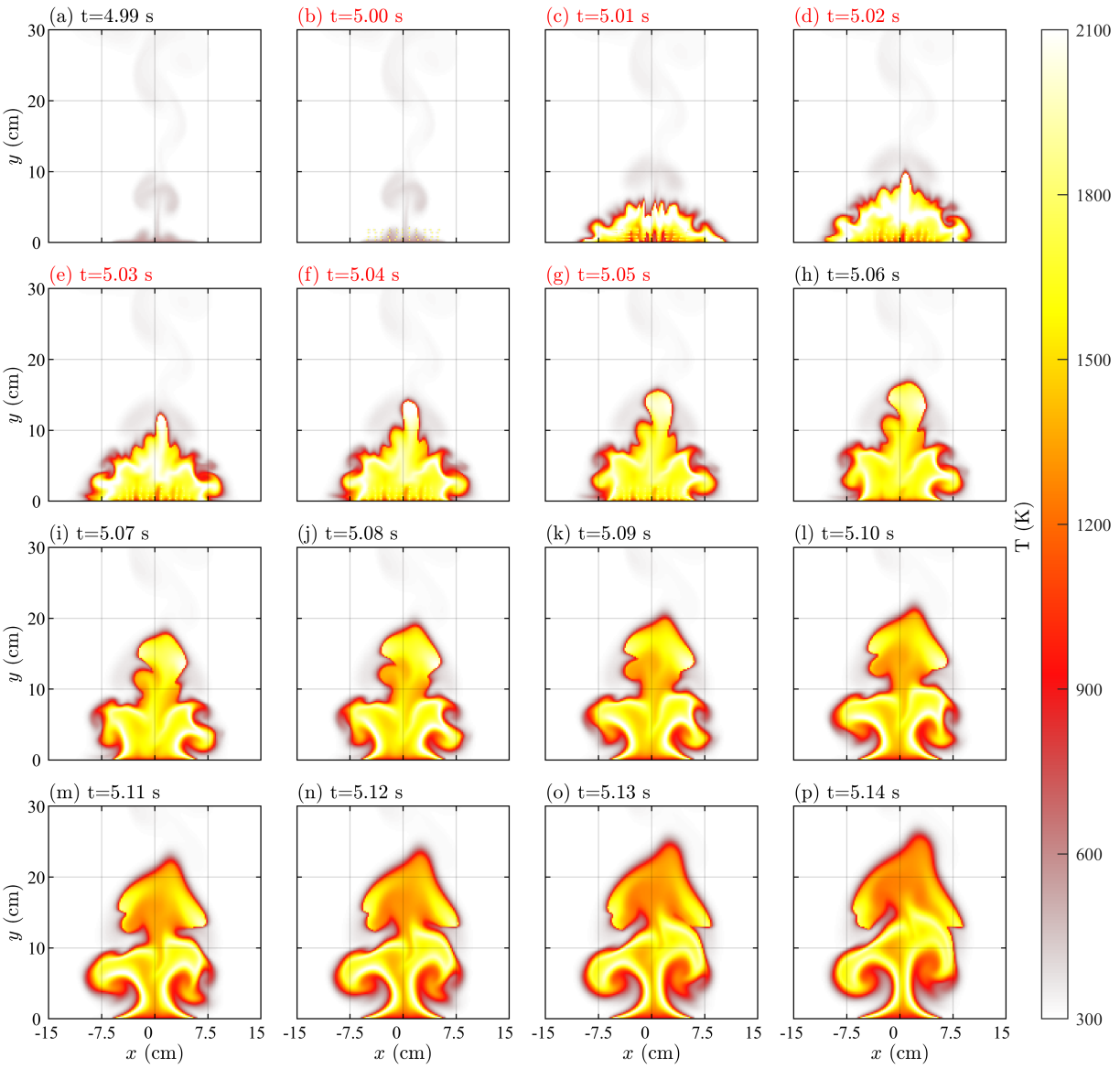


Figure B.2: Time-series of temperature during ignition with Skeletal-B model, with 0.05 s spark beginning at $t = 5$ s. Time labels written in red indicate when the simulation is under-going the "sparking" process.

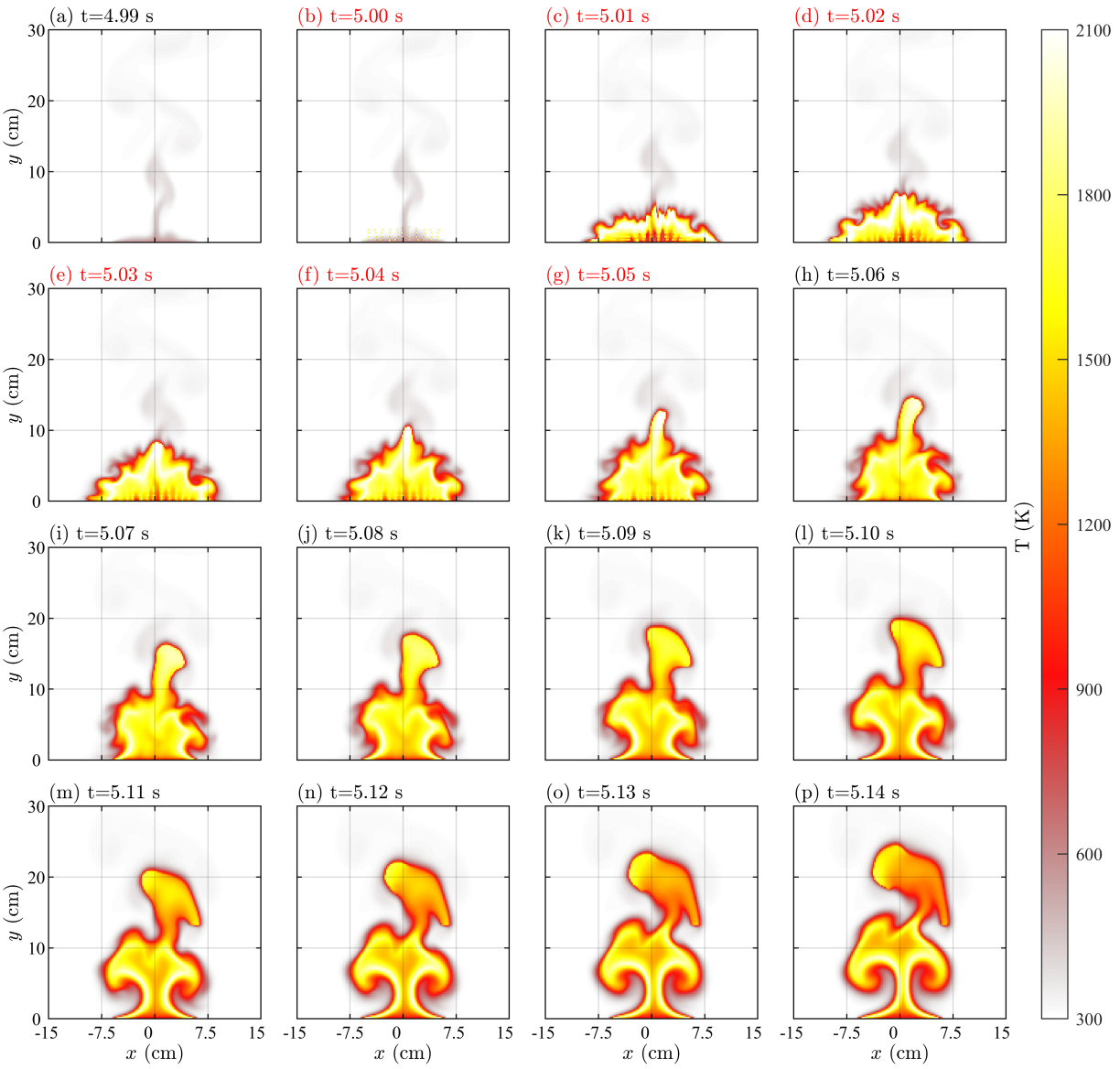


Figure B.3: Time-series of temperature during ignition with Skeletal-C model, with 0.05 s spark beginning at $t = 5$ s. Time labels written in red indicate when the simulation is under-going the "sparking" process.

# Appendix C

## Comparisons of Exact and Average Power Spectral Densities

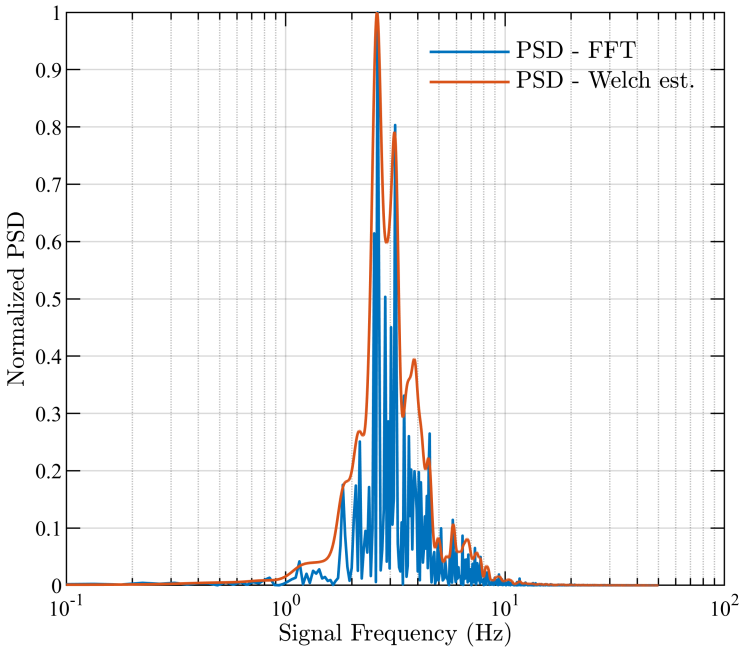


Figure C.1: Comparison of the exact PSD, calculated via FFT (blue) and the window-averaged PSD, calculated via Welch's method (orange) for Skeletal-A.

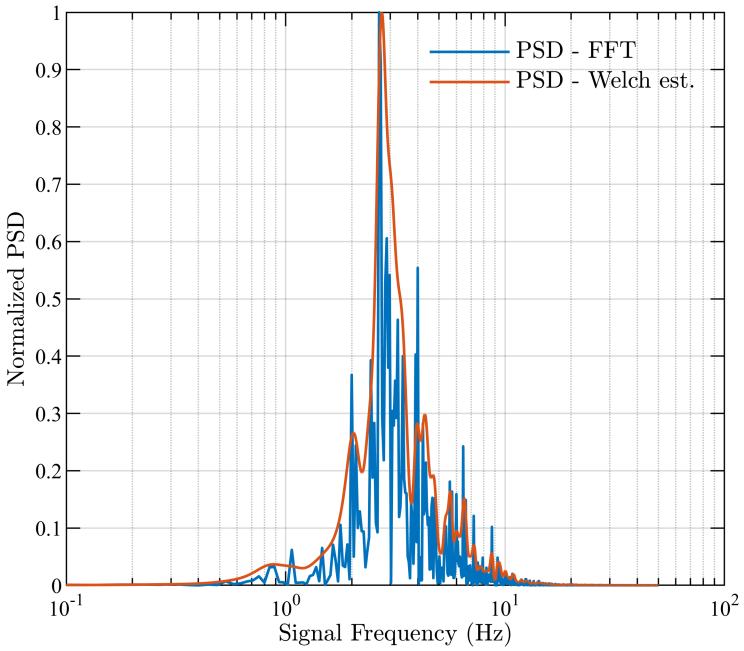


Figure C.2: Comparison of the exact PSD, calculated via FFT (blue) and the window-averaged PSD, calculated via Welch's method (orange) for Skeletal-B.

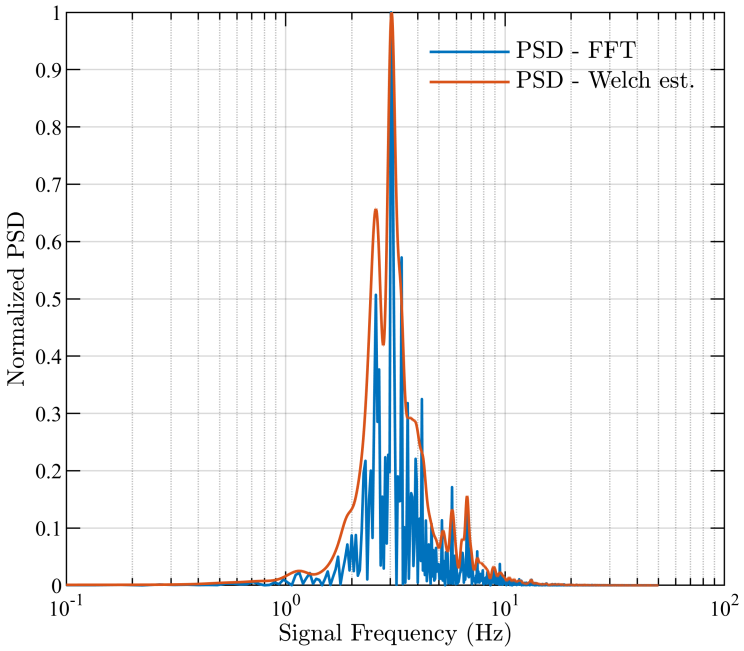


Figure C.3: Comparison of the exact PSD, calculated via FFT (blue) and the window-averaged PSD, calculated via Welch's method (orange) for Skeletal-C.

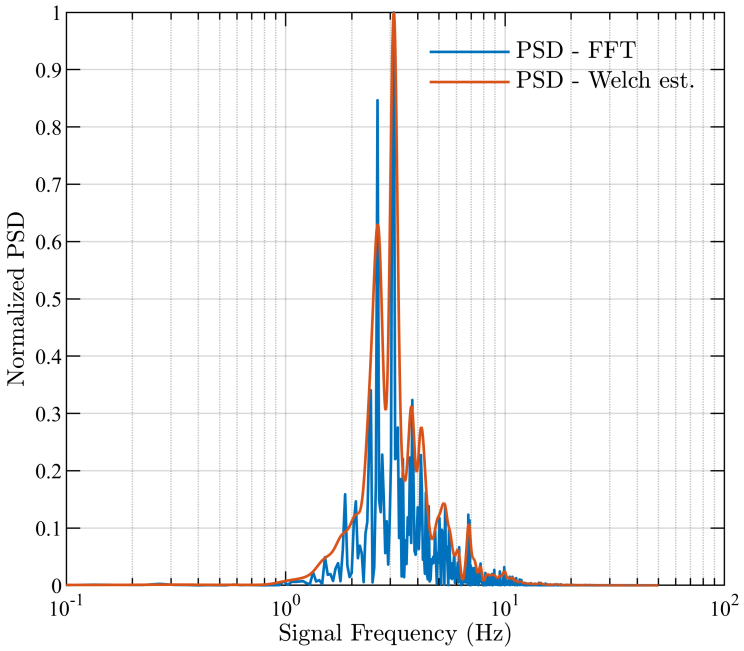


Figure C.4: Comparison of the exact PSD, calculated via FFT (blue) and the window-averaged PSD, calculated via Welch's method (orange) for Skeletal-D.

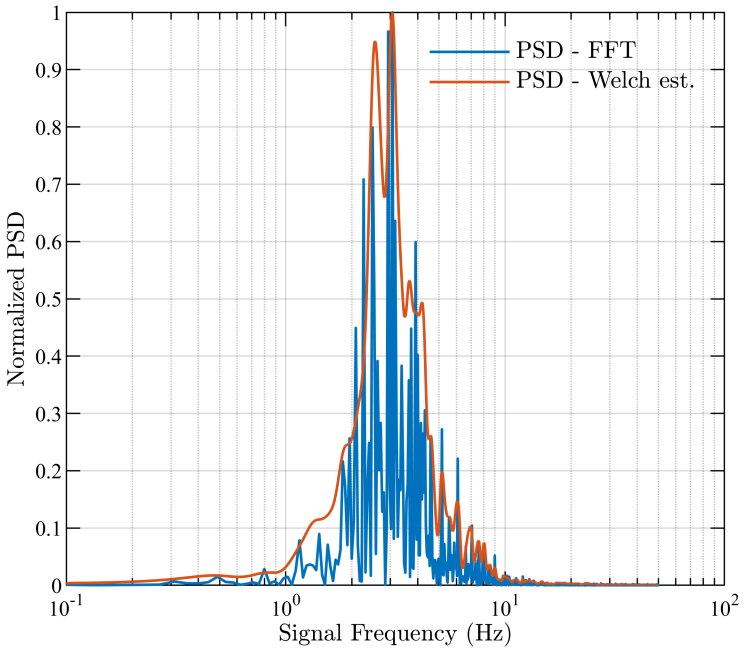


Figure C.5: Comparison of the exact PSD, calculated via FFT (blue) and the window-averaged PSD, calculated via Welch's method (orange) for infinitely-fast chemistry.

# Appendix D

## Comparisons of HRR′ and Vertical Velocity-Based Power Spectral Densities

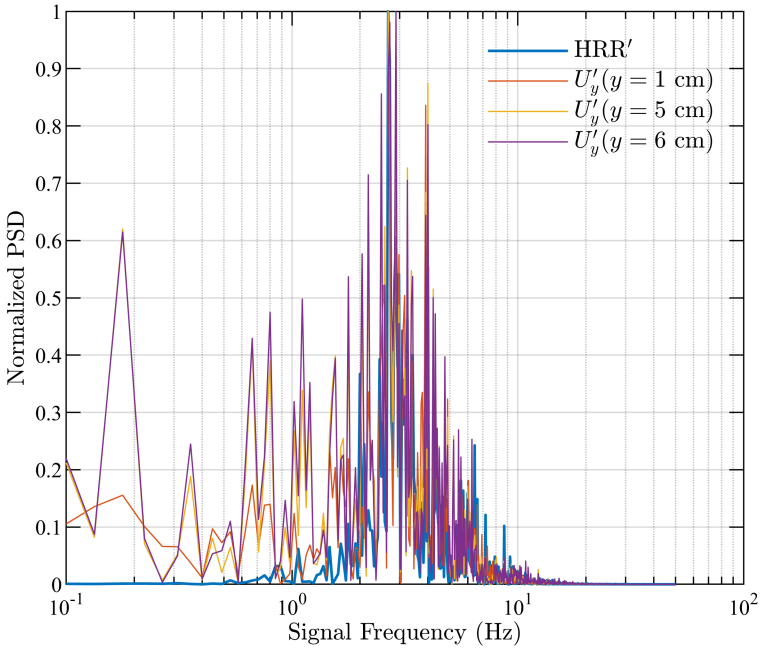


Figure D.1: Comparison of the normalized PSD, calculated via HRR′ (blue), and $U_y'$ at 1 cm (red), 5 cm (yellow) and 6 cm (purple) along the centerline for Skeletal-B.

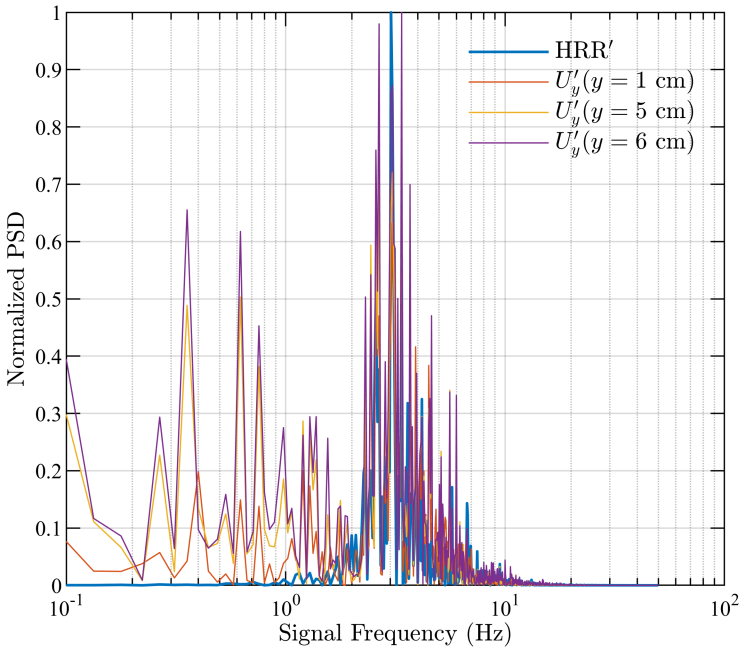


Figure D.2: Comparison of the normalized PSD, calculated via HRR′ (blue), and $U_y'$ at 1 cm (red), 5 cm (yellow) and 6 cm (purple) along the centerline for Skeletal-C.

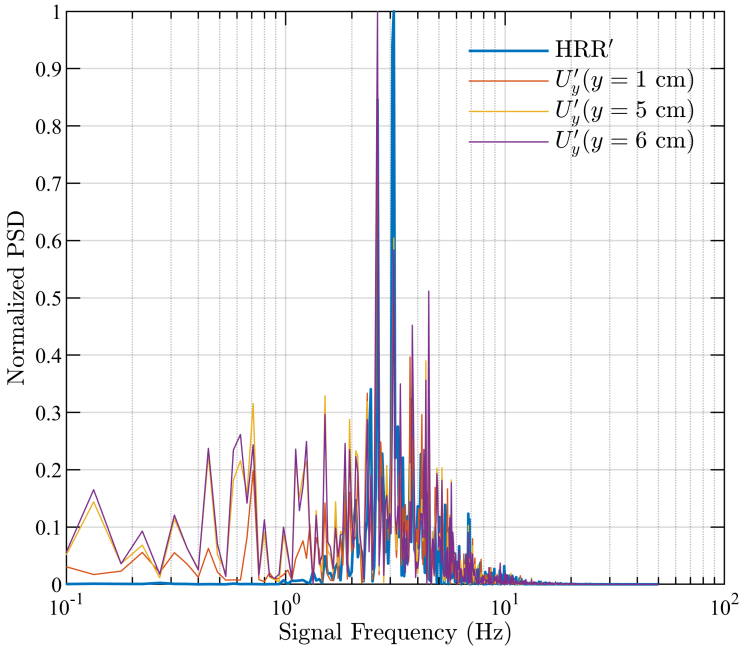


Figure D.3: Comparison of the normalized PSD, calculated via HRR′ (blue), and $U_y'$ at 1 cm (red), 5 cm (yellow) and 6 cm (purple) along the centerline for Skeletal-D.

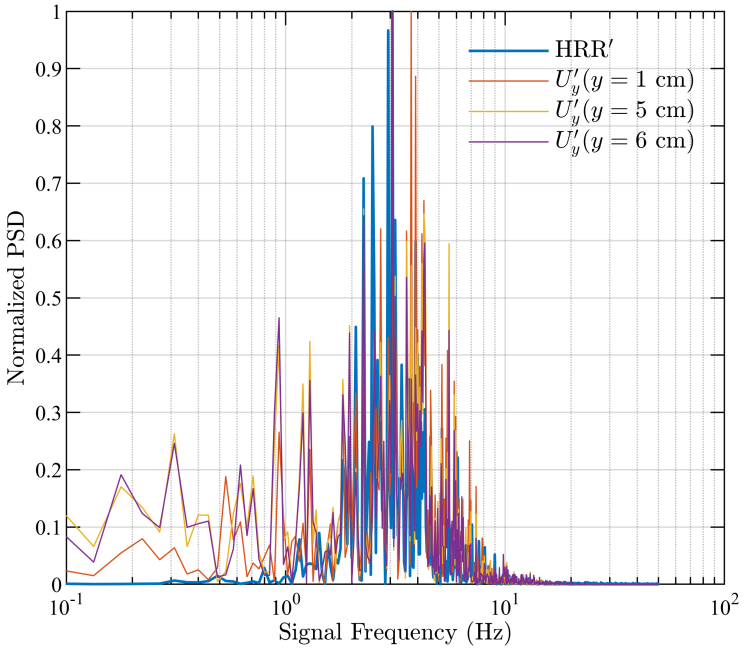


Figure D.4: Comparison of the normalized PSD, calculated via HRR′ (blue), and $U_y'$ at 1 cm (red), 5 cm (yellow) and 6 cm (purple) along the centerline for infinitely-fast chemistry.